Driving quantum materials using resonators, orbitals and phonons

Matthiesen, M.

DOI
10.4233/uuid:0c1664e3-b128-4ecb-8521-1d1ba3d0d2db

Publication date
2025

Document Version
Final published version

Citation (APA)
Matthiesen, M. (2025). *Driving quantum materials using resonators, orbitals and phonons*. [Dissertation (TU Delft), Delft University of Technology]. https://doi.org/10.4233/uuid:0c1664e3-b128-4ecb-8521-1d1ba3d0d2db

DRIVING QUANTUM MATERIALS USING RESONATORS, ORBITALS AND PHONONS

Mattias Matthiesen

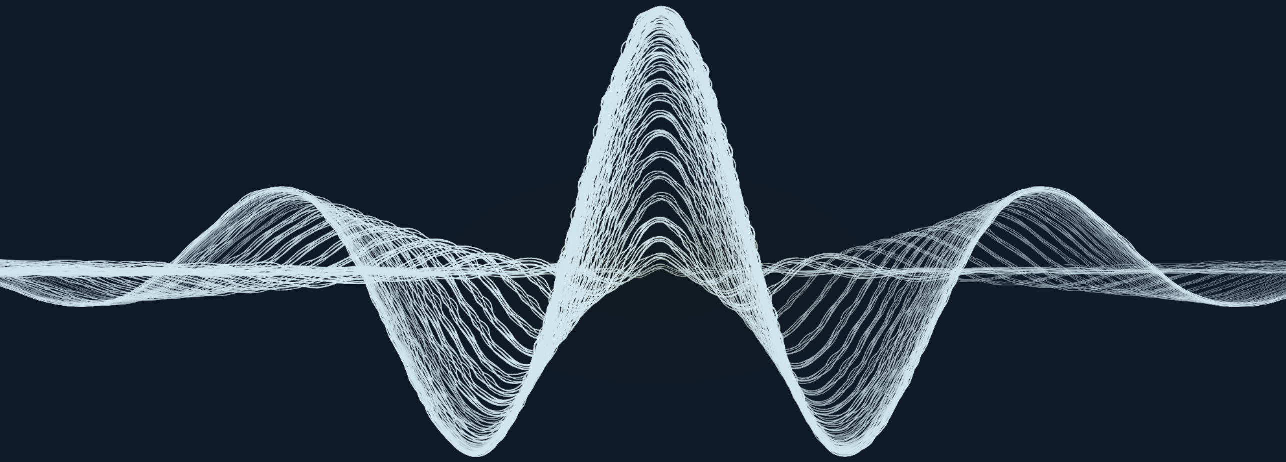

Driving quantum materials using resonators, orbitals and phonons

Driving quantum materials using resonators, orbitals and phonons

Dissertation

for the purpose of obtaining the degree of doctor

at Delft University of Technology

by the authority of the Rector Magnificus prof. dr. ir. T.H.J.J. van der Hagen

chair of the Board for Doctorates

to be defended publicly on

10 January 2025 at 12:30 o'clock

by

Mattias MATTHIESEN

Master of Science in Applied Physics
Delft University of Technology, The Netherlands

born in Bergen, Norway.

This dissertation has been approved by the promotors.

promotor: prof. dr. A. Caviglia
promotor: prof. dr. Y. Blanter

Composition of the doctoral committee:

Rector Magnificus,	chairperson
prof. dr. Y. Blanter,	Delft University of Technology, promotor
prof. dr. A. Caviglia,	University of Geneva, promotor
Independent members:	
prof. dr. T. H. M. Rasing,	Radboud University
dr. M. H. Diniz Guimaraes,	University of Groningen
dr. G. J. Verbiest,	Delft University of Technology
prof. dr. ir. O. Isabella,	Delft University of Technology
dr. A. R. Akhmerov,	Delft University of Technology
prof. dr. L. Siebbeles,	Delft University of Technology, reserve

Printed by: Gildeprint
Front & Back: Cover art by Mattias Matthiesen

ISBN 978-94-6366-984-9

An electronic version of this dissertation is available at
`http://repository.tudelft.nl/`.

Dedikert til Inger og Are, som sendte en liten
forskerspire på kjemikurs og robotikkskole, og som
alltid har vist stolthet uten krav og forventninger.

Contents

Summary

In this work, we explore various ways in which pulses of light can perturb solid phases in a controlled and purposeful manner. Through the use of nonlinear optical effects, electromagnetic pulses spanning from the visible to the far-infrared target specific transitions anticipated to trigger non-trivial dynamics of macroscopic properties. The two ingredients, light and matter, participate in each experiment, but undergo greater levels of intervention as the chapters progress: To start—in chapters 2 and 3—we exploit natural instabilities in quantum materials, producing magnetization and spin waves with light. In chapter 4, we intervene in the structure of a solid to create acoustic confinement and excite high-frequency strain modulations using electron-phonon coupling. Finally, in chapters 5 and 6, we intervene in the structure of the light fields by engineering microscopic electric resonators in the terahertz band, exploiting their strong internal electric field to trigger carrier delocalization in a coupled correlated insulator.

Samenvatting

In dit werk verkennen we verschillende manieren waarop lichtpulsen vaste fasen op een gecontroleerde en doelgerichte manier kunnen verstoren. Door gebruik te maken van niet-lineaire optische effecten richten elektromagnetische pulsen, die reiken van het zichtbare tot het verre infrarood, zich op specifieke overgangen die naar verwachting niet-triviale dynamiek van macroscopische eigenschappen teweegbrengen. De twee ingrediënten, licht en materie, nemen deel aan elk experiment, maar ondergaan naarmate de hoofdstukken vorderen steeds grotere interventies: Om te beginnen — in chapters 2 and 3 — maken we gebruik van natuurlijke instabiliteiten in kwantummaterialen, waarbij we met licht magnetisatie en spin-golven opwekken. In chapter 4 grijpen we in op de structuur van een vaste stof om akoestische opsluiting te creëren en hoge-frequentie spanningsmodulaties te stimuleren via elektron-fonon-koppeling. Ten slotte, in chapters 5 and 6, grijpen we in op de structuur van de lichtvelden door microscopische elektrische resonatoren in het terahertz-gebied te ontwerpen, waarbij we hun sterke interne elektrische veld benutten om ladingsdragers te delokaliseren in een gekoppelde gecorreleerde isolator.

Introduction

In a remarkable advancement of technology, the measurement of processes occurring at speeds faster than a trillionth of a second is achievable in many scientific laboratories today. This feat was made possible by the advent of ultrashort laser pulses, granting scientists a highly resolved window into the temporal unfolding of cause and effect. As effects temporally succeed (and possibly coincide with) their causes, this unparalleled time resolution serves as a potent instrument for studying physical processes, and in particular, the dynamics of electrons, ions, and spins in condensed matter systems.

The tools available to the spectroscopist are legion: Magneto-optics, spectroscopy, polarimetry, and interferometry all provide unique insight into physical properties and can be performed at any photon energy available with the use of nonlinear optical elements for frequency conversion. In this dissertation for example, we use near-infrared and visible-light pulses, on the scale of 1 eV and 100 THz, to photodope insulators, measure the time evolution of magnetization in ferromagnets, excite and measure acoustic vibrations in thin membranes. Pulses in the mid-infrared, on the scale of 10 meV or 10 THz, are used to resonantly excite optical phonons. Terahertz pulses, on the scale of 1 meV, are used to measure conductivity, assist electrons in tunneling across band gaps, and measure spin-charge conversion.

One might notice from the above list that light is used not only as a way to measure but also as a way to influence a system. As such, the experiments in this dissertation can be understood to exist at the intersection of science and engineering, naively conceived, where the goal is simultaneously to gain an understanding of causes while also seeking a level of technological control over the effects. These experiments are part of a larger effort to discover ways in which macroscopic quantities and properties that do not couple to light, may nevertheless be controllably perturbed with light through the internal correlations and competing energy scales within the solid.

The key strength of experiments that use ultrashort light pulses is *selectivity*: Photon energy and polarization can select a specific dipole moment or optical resonance to excite, leaving others unperturbed except through their mutual interactions. In chapters 2 and 3 we drive intrinsic resonances in solids that bring them into a non-equilibrium state. There, new interactions can occur, resulting in complex macroscopic dynamics as the system minimizes its energy and returns to equilibrium. Chapters 4 to 6 take a different approach: We engineer resonances using micro- or nanopatterned structures that support strongly confined terahertz fields—electric and elastic—whose amplitudes bring them into competition with the internal interactions of the solid. Finally, in chapter 7, we study a non-resonant process in which large bandwidth terahertz pulses can be generated from spin currents.

1.1. Quantum materials

A small subset of internal degrees of freedom of a solid, such as infrared active phonons and optical transitions allowed by selection rules, have a dipole moment with which the electric fields of light may couple. Fortunately, many materials exhibit strong correlations between these dipole moments and other internal degrees of freedom (e.g., spin, charge, orbitals, and displacement), creating microscopic pathways through which light may produce desirable side-effects. Solids whose ground states are characterized with significant such correlations are sometimes referred to as *quantum materials*, or correlated materials.

In chapter 3, the correlations are the magnetic interactions between electrons after a charge-transfer transition that causes the formation of a transient magnetic order; in chapter 2, the correlations are between the spin and the orbital degree of freedom of pho-

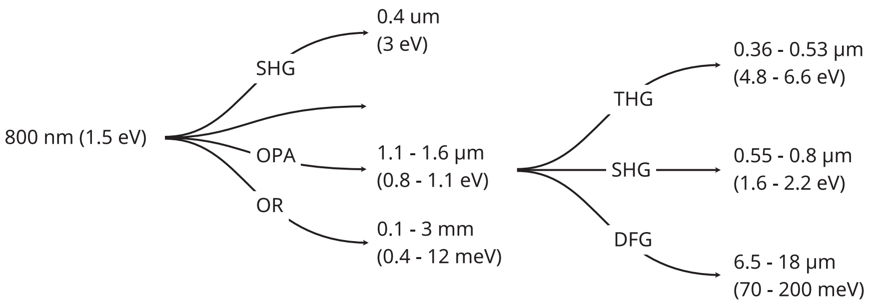

Figure 1.1: **Frequency conversion processes** The 1.5 eV pulses from the Ti:S laser are converted to lower and higher frequencies using optical parametric amplification (OPA), second harmonic generation (SHG), third harmonic generation (THG), optical rectification (OR), or difference-frequency generation (DFG).

toexcited bound electrons, and leads to collective oscillations of spins; in chapter 7, the same type of correlation, but for itinerant electrons, allows for the interconversion between spin and charge currents, and in chapter 6, the correlations are charge repulsions between electrons in highly covalent orbitals, which can be overcome by the application of strong electric fields.

1.2. Optical experiments

The various resonances that couple to light exist at distinct energies, and thus necessitates the conversion of laser pulse frequency through the use of nonlinear optical effects. The experiments of this disseration are driven by a titanium-sapphire (Ti:S) amplified laser, providing an average power of 7 W at a repetition rate of 1 kHz and a pulse duration of 100 fs. This pulse train is split into multiple beam paths using beam splitters, and converted into other frequencies using nonlinear optical processes, as illustrated in figure 1.1. A pair of optical parametric amplifiers (OPA) are used to generate pulses with independently tunable wavelengths in the range 1.1 µm to 1.6 µm. These in turn can either be mixed in a GaSe crystal to generate radiation at the difference of their central frequency, known as difference-frequency generation (DFG), producing wavelengths in the range 6.5 µm to 18 µm (16 THz to 46 THz) which is useful for resonant excitation of optical phonons. Alternatively, an output of the OPA can interact with a nonlinear medium such as BBO to generate second harmonic (SHG) or third harmonic (THG) frequencies, for excitation at higher energy such as photodoping above band gaps as in chapter 3 or

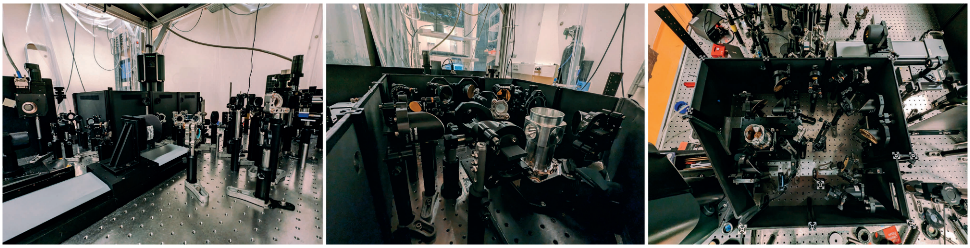

Figure 1.2: **Optical table configuration** The optical table is always changing, adapted to suit experiments. Here is shown a snapshot in time and space of the optical scheme, near the position of the sample. To the left, an optical delay line that sets the relative delay of pulses. In the center, parabolic mirrors focus light to the sample positioned inside the aluminium radiation shield, inside of which the sample can be cooled to a temperature of 5 K. To the right, a top view of the scheme around the sample, with an encasing that can be purged with dry air for experiments involving terahertz frequencies (for which water vapor is a strong absorber).

d-d orbital transitions as in chapter 2. Lastly, the direct output of the Ti:S laser can be frequency doubled in BBO, or it can undergo optical rectification (OR) in ZnTe, GaP or other nonlinear crystals that produce terahertz radiation, as in chapters 5 and 6.

All these processes require many optical elements, such as nonlinear crystals, mirrors, lenses, beam splitters, polarizers, curved and movable mirrors, as well as cryogenic equipment to move across thermal phase transitions, enclosures and dry air to control the water vapor levels in the air, photodiodes and photomultiplier tubes to measure laser intensity, lock-in amplifiers and oscilloscopes. Figure 1.2 shows photographs of parts of the optical table, and gives an impression of the experimental setup at a snapshot in time. More details on the experiments are given in the respective chapters.

1.3. Experimental techniques

Several experimental techniques are used in this dissertation, most being a variant of a **pump-probe scheme**: The sample under study is exposed to a pair of pulses—the pump pulse and the probe pulse—separated by a variable time delay that is scanned in the experiment. This time delay is produced by passing either the pump or the probe a mirror placed on a movable stage whose position is controlled by a computer. The speed of light is 0.3 mm/ps, so changing the time delay by an amount equal to the shortest pulses used in this work (100 fs) amounts to moving the mirror by 30 µm. The purpose of the *pump* is to excite the sample (e.g. an electronic transition), while the *probe* is used to measure the instantaneous value of some property. Which property is measured depends on what frequencies the probe contains, as well as which property of the probe pulse is being recorded (e.g. intensity, polarization, electric field).

In chapter 2, we study the dynamics of the magnetic order of the antiferromagnetic insulator $MnPS_3$ using magnetically induced *second harmonic generation*; in chapter 3, we use *terahertz time-domain spectroscopy* and the *Faraday effect* to measure electronic and magnetic dynamics in a photodoped non-magnetic insulator, $CaMnO_3$; in chapter 4, we measure the *time-resolved reflectivity* of freestanding membranes of the itinerant electron system $SrRuO_3$ after the excitation of highly confined coherent acoustic waves; in chapters 5 and 6, we study the conductivity of the insulator $NdNiO_3$ using *terahertz time-domain spectroscopy*, after submitting it to strongly confined electric fields with large amplitude; in chapter 7, the *Faraday effect* measures the magnetization of Co after photoexcitation, while *terahertz emission spectroscopy* probes transient charges flowing in the material due to the inverse spin Hall effect in an adjacent layer of Pt.

Below, we provide a brief overview of the main optical methods used in the experiments of each chapter, while full-length treatments of these can be found in textbooks and review articles which will be referenced in the following.

1.3.1. Terahertz time-domain spectroscopy

Terahertz time-domain spectroscopy (THz-TDS) is a technique that uses pulsed, phase-stable pulses with spectral content in the terahertz band (roughly 0.1 THz to 10 THz) as a spectroscopic probe. The pulses are reflected from, or transmitted through, a sample of study, and compared with a reference pulse. The distortion of the pulse due to the interaction with the sample encodes the full complex permittivity (or alternatively, conductivity) of the sample. The technique is non-contact, non-destructive, and can be used to study charges, phonons, and spins in the meV range with amplitude and phase information. In the special case that the sample of study itself produces THz radiation, we refer to the experiment as terahertz *emission spectroscopy*. For an excellent textbook on terahertz spectroscopy, see Dexheimer et al. [1].

Generation of terahertz pulses

Methods for generating terahertz radiation from the output of femtosecond lasers rely either on a transient current $\mathbf{j}$ or a transient polarization $\mathbf{P}$, as apparent from the inhomogeneous electric wave equation:

$$\nabla^2 \mathbf{E} - \frac{1}{c^2}\frac{\partial^2 \mathbf{E}}{\partial t^2} = \frac{4\pi}{c}\left(\frac{\partial^2 \mathbf{P}}{\partial t^2} + \frac{\partial \mathbf{j}}{\partial t}\right) \tag{1.1}$$

Generation based on transient currents is the foundation of the widely used photoconductive switches, and the photo-Dember effect. For large amplitude applications, a nonlinear polarization is instead used, which is the foundation of *optical rectification* (OR), and is the effect used in the experiments of this dissertation. Optical rectification is a second-order nonlinear optical effect and can be understood as difference-frequency generation between pairs of frequencies within the spectrum of the generating pulse—a femtosecond laser pulse with energies in the eV range. For example, consider a component $\cos(\omega_1 t)$ and another $\cos(\omega_2 t)$, producing a second-order polarization:

$$P^{(2)}(t) \sim \cos(\omega_1 t)\cos(\omega_2 t) = \frac{1}{2}\left(\cos[(\omega_1 - \omega_2)t] + \cos[(\omega_1 + \omega_2)t]\right) \tag{1.2}$$

The difference term, $\cos[(\omega_1 - \omega_2)t]$, is the slowly oscillating component that falls within the terahertz range for typical femtosecond laser pulses. Integrating over all pairs (ω_1, ω_2) within the generation pulse bandwidth yields a broadband spectrum in the terahertz range. Further considerations to optimize this process, such as phase matching and identifying materials with a large second-order nonlinear coefficient, are discussed in reference [1].

Detection of terahertz pulses

Electro-optic sampling of a free-space propagating THz pulse was first demonstrated in the 1990s [2]. This method operates based on the linear electro-optic effect, also known as the Pockels effect. Here, the electric field of a THz pulse co-propagates with an optical sampling pulse—typically a higher-energy pulse of significantly shorter duration, such as the 1.5 eV output of a Ti:S laser—causing an instantaneous local birefringence in the EO crystal. With sufficient phase matching, the sampling pulse experiences consistent birefringence throughout the crystal, propagating in tandem with the same instantaneous time slice of the THz waveform. Consequently, the linearly polarized optical sampling pulse becomes distorted in proportion to the instantaneous electric field, $E(t)$, of the THz pulse. Specifically, the sampler transitions to elliptical polarization due to the induced phase modulation, $\Gamma(t)$. This ellipticity, or phase modulation, is split into two beams with orthogonal polarizations by a prism, the difference of which is proportional to $\sin(\Gamma) \propto E(t)$. Essentially, the phase modulations are converted into intensity modulations, detectable by balanced photodiodes. A complete electric waveform is obtained by adjusting the relative delay between the sampler and the THz pulse.

1.3.2. Magneto-optic measurements

Magneto-optic effects allow for optical detection of macroscopic magnetic moments. According to equation (1.1), the propagation and dispersion of light depends on the polarization $\mathbf{P}$ induced in the material. Through the spin-orbit interaction, the spin degree of freedom can affect the polarizability of electrons, summarized in the electric permittivity tensor ϵ.

In the Faraday effect, also known as magnetic circular birefringence, the a phase shift between helicity components of the light builds up during propagation through a magnetic material, which in the linear basis amounts to a rotation θ_F of the polarization plane. In the magneto-optic Kerr effect, the phase shift is imparted on reflected light [3], and results generically in both a rotation θ_K and ellipticity η_K. The phenomenology of both effects enter into the off-diagonal components of the electric permittivity tensor, and are linear in the magnetization $\mathbf{M}$ of the material. Since the Faraday rotation is proportional to the sample thickness, it is typically easier to measure than the magneto-optic Kerr effect, the latter being the better choice for highly absorbing or very reflective samples.

1.3.3. Second harmonic generation

According to equation (1.2), given a finite second-order nonlinear susceptibility, driving a material at a frequency ω will produce a polarization oscillating at a frequency 2ω. This is not allowed in centrosymmetric materials: Since this symmetry requires the susceptibility $\chi^{(2)}$ to be invariant under inversion, whereas the polarization and the electric field both change sign under inversion, we have $P = \chi E^2 = \chi(-E)^2 = -P$, which entails $P = 0$. Therefore, second-harmonic generation is an effective optical probe of the breaking of inversion symmetry, and is heavily used in the study of ferroelectrics.

In chapter 2, we study a special case of second-harmonic generation that is caused by the breaking of inversion symmetry by the magnetic structure, rather than crystal structure. Similar to the magneto-optic effects, the spin sensitivity to this electric effect is due to the spin-orbit interaction. More details are given in chapter 2, and a comprehensive review can be found in Fiebig et al. [4].

1.3.4. Acoustic reflectometry

The use of picosecond acoustic pulses to probe the properties of materials, such as sound velocity, elastic properties, and highly resolved thickness measurements of multilayer heterostructures, started with pioneering experiments in the 1980s [5]. In short, a pico- or femtosecond laser pulse is used to generate a coherent acoustic pulse through the production of stress in the material, which evolves according to the elastic properties of the material and the wave equation. Since the electronic structure are sensitive to the crystal volume and shape, the propagation or evolution of the acoustic waves cause modulations of the electric permittivity of the material, which can be detected by measuring the reflectivity or transmittivity of the material. For a comprehensive review of generation mechanisms for coherent acoustic pulses, see Ruello et al. [5]. The detection of coherent acoustic waves is reviewed in Matsuda et al. [6].

2

Impulsive excitation of magnons via orbital transitions

In magnetic lattices with orbital angular momentum, spin-orbit coupling enables spin dynamics through the resonant excitation of low-energy electric dipoles such as phonons and orbital transitions which interact with spins. However, without orbital angular momentum, microscopic pathways for the resonant and low-energy optical excitation of coherent spin dynamics are few. In this chapter we consider the relative merits of electronic and vibrational excitations for the optical control of zero orbital angular momentum magnets, focusing on a limit case: the insulating antiferromagnet manganese phosphorous trisulfide ($MnPS_3$), constituted by orbital singlet Mn^{2+} ions. We study the correlation of spins with two types of excitations within its band gap: an orbital singlet-triplet transition of Mn^{2+} causing coherent spin precession, and an optical phonon causing thermal spin disordering. Our findings cast orbital transitions as key targets for magnetic control in insulators constituted by magnetic centers of zero orbital angular momentum.

This chapter is based on Matthiesen et al. [1], “Controlling magnetism with light in a zero orbital angular momentum antiferromagnet”.

Magnets are central to modern advanced technologies, for example, as bits in magnetic memories or as spin current conductors in spintronic devices. Recently, the inclusion of antiferromagnets into spin-based devices has garnered much interest, as they offer faster intrinsic spin dynamics and lower dissipation than the more commonly utilized ferromagnets [2]. Lacking net magnetization, antiferromagnets must be manipulated through non-magnetic drives, such as electric currents and voltages [3, 4], mechanical strain [5, 6], or light [7]. The latter, in the form of ultrashort laser pulses, allows spin perturbation at diabatic timescales, faster than the intrinsic timescales even of antiferromagnetic spin dynamics [8]. The light-spin coupling typically involves excited states of the magnetic ion orbitals, either virtually [9] or directly [10, 11], by causing a transient change of orbital angular momentum. This modifies the spin-lattice coupling (e.g., through magneto-crystalline anisotropy), and exerts a transient torque on the spins. With the advent of intense low-frequency pulses capable of resonant excitation of large amplitude optical phonons, new approaches have become possible that target the spin-lattice coupling not through orbitals, but instead through perturbation of the crystal field [12]—indirectly causing dynamics of the orbital angular momentum. The magnetic ions of many antiferromagnets lack orbital angular momentum, either due to strong crystal field quenching (e.g., Ni^{2+} in an octahedral field), or because the ion has a half-filled shell (e.g., Mn^{2+}, Fe^{3+}, Ni^{3+}). This raises the question of whether, in such magnets, the most efficient pathway to magnetic control should be via lattice or orbital perturbation. We study the spin dynamics caused by excited states of the crystal lattice and of the electron orbits in manganese phosphorous trisulfide ($MnPS_3$), a material in which the magnetic centers have strictly zero orbital angular momentum. We find that in this material, optical excitation of bound electrons involving a change of orbital angular momentum can cause coherent spin precession, whereas excitation of lattice vibrations leads to thermal spin disordering.

2.1. Manganese phosphorous trisulfide

The two-dimensional antiferromagnet $MnPS_3$ has recently attracted a lot of attention with observations of long-distance magnon transport [13], relativistic domain-wall dynamics [14] and giant dynamical modulations of its optical nonlinearities [15]. It is a van der Waals crystal with a layered two-dimensional crystalline and magnetic structure [16] (see figure 2.1b and c), which due to its small interplane magnetic exchange [17] retains

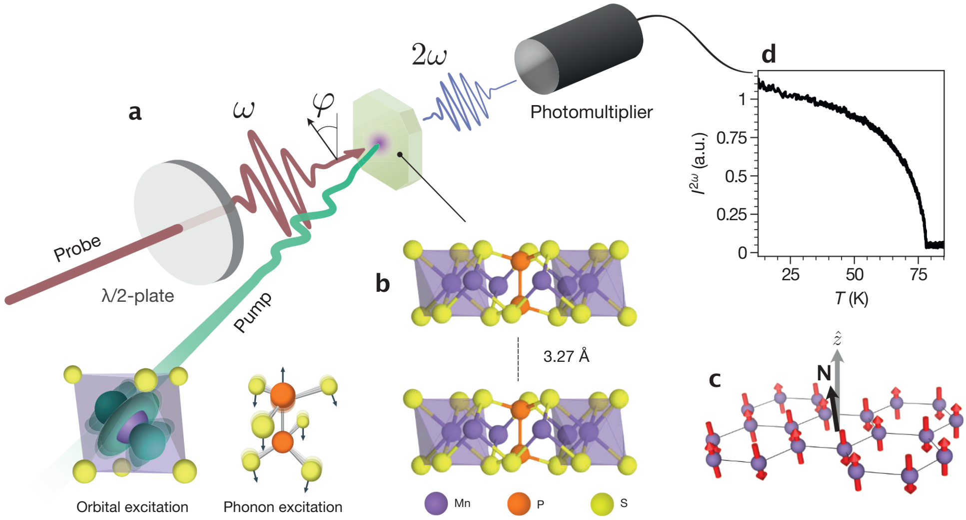

Figure 2.1: **Ultrafast optical spectroscopy of the magnetic order in single crystal MnPS$_3$** **a**. Schematic of the all-optical experimental setup, consisting of two incident beams: One to excite the material (green) and one to generate the second harmonic probe (red, frequency ω). The generated SHG (2ω) is detected with a photomultiplier tube. Inset: To bring the system out of equilibrium, we excite either d-d orbital transitions of the magnetic ions or in the phonon band. **b**. The layered crystal structure, consisting of sulfur-coordinated Mn^{2+} ions conjoined by $[P_2\, S_6]^{4-}$ molecules. **c**. The magnetic structure of MnPS$_3$, with **N** indicating the direction of the Néel vector and z the normal to the crystal planes. **d**. The temperature dependence of the second-harmonic intensity.

magnetic order down to a few layers [18, 19]. Within the two-dimensional layers, the Mn^{2+} ions are arranged in a honeycomb lattice. Below a Néel temperature of $T_N = 78$ K a fully compensated antiferromagnetic Néel ordered ground state forms (see figure 2.1c). This results in two collinear magnetic sublattices with oppositely oriented magnetizations, their difference constituting the antiferromagnetic order parameter—the Néel vector **N**. A predominantly out-of-plane orientation of N is caused by the magnetic dipole-dipole interaction [20]. Importantly for this work, the magnetic centers (Mn^{2+}) are in an orbital singlet ground state ψ_0 (Mulliken symbol ${}^6A_{1g}$) with a half-filled shell ($t_{2g}^3\, e_g^2$) such that $L = 0$. As is well known, the orbital angular momentum of transition-metal ions is typically reduced or quenched in crystals by the breaking of rotational symmetry in the crystal field [21]. The case of $MnPS_3$ is more extreme, where even the *free* ion has $L = 0$. Extraneous contributions to L from the ligands is also minimal, with only p-orbital ions and no other transition metals. Altogether, this casts $MnPS_3$ as an interesting limit-case “orbital angular momentum-free” antiferromagnet.

We studied a single crystal sample of $MnPS_3$ grown using chemical vapor transport [22], approximately 10 µm thick with a diameter of about 3 mm. All experiments were performed in a transmission geometry, where the probing light propagates through the crystal to the detector (see figure 2.1a).

2.2. Magnetically induced second harmonic generation

Despite the absence of magnetization, the magnitude of the order parameter **N** can be measured optically in this material through a magnetically induced second harmonic generation (MSHG) [18, 23, 24]. Neutron polarimetry shows that for $MnPS_3$, the magnetic point group (2’/m) group is non-centrosymmetric [25]. The breaking of both time-reversal and space-inversion symmetries by this magnetic order leads to a new contribution to the SHG, giving a nonlinear susceptibility of the form [23]

$$\hat{\chi}^{(2)} = \hat{\chi}(0) + \hat{\chi}(N) + \mathcal{O}(N^2) \tag{2.1}$$

where $\hat{\chi}(0)$ is the crystallographic contribution, insensitive to magnetic order, and $\hat{\chi}(N)$ which arises from the magnetic order and is linear in the magnetic order parameter N. In $MnPS_3$ the crystal structure is centrosymmetric, so that $\chi(0) \equiv 0$, leaving only the magnetic contribution $\chi(N)$ to the second-order susceptibility within the dipole approximation.

To measure MSHG we use pulses of photon energy 1.5 eV, generated by an amplified titanium-sapphire (Ti:S) laser ($\Delta t = 100\,\mathrm{fs}$, $f_{\mathrm{rep}} = 1\,\mathrm{kHz}$). The emitted second harmonic (3 eV) is detected using a photomultipler tube with strong band pass filters. We confirm the sensitivity of SHG to the magnetic order parameter by measuring its temperature dependence (figure 2.1d) which shows a sharp onset of signal at a temperature of $T_{\mathrm{N}} = 77.5(5)\,\mathrm{K}$. The origin of $\hat{\chi}(N)$ can be intuited as follows: Thinking of the action of the pump field as inducing two second-order polarizations of opposite sign, in the centrosymmetric lattice these cancel out by symmetry. However, spin-orbit coupling contributes a perpendicular velocity to the displacement currents, in analogy to the spin Hall effect, which due to the magnetic asymmetry do not cancel out and produces a net second harmonic signal.

2.3. Orbital excitation

Below the optical band gap (2.96 eV) [26], $MnPS_3$ has several absorption lines of different origin. We first consider the absorption lines caused by transitions within the Mn^{2+} ions. The ionic ground state ψ_0 is an orbital singlet ($L = 0$) with five unpaired spins ($S = 5/2$). Due to the sulfide crystal field, the first excited state is split into four states, with the lowest ψ_1 (Mulliken symbol $^4\mathrm{T}_{1g}$, or $\mathrm{t}_{2g}^4\,\mathrm{e}_g^1$) being an orbital triplet $L = 1$ with spin $S = 3/2$ at an energy of 1.92 eV, well below the optical gap [26]. Since this transition changes the quantum numbers of the magnetic centers, we find it a promising target for optical perturbation of the magnetic order. This state can in fact be populated optically: While prohibited by both spin- and parity-conserving selection rules, this transition does carry a dipole moment due to coupling to optical phonons that break the local centrosymmetry [27].

To excite this orbital transition, we generate pulses with photon energies 1.9 eV, in resonance with the transition energy. These are generated using a parametric amplifier seeded by the Ti:S laser ($\Delta t = 100\,\mathrm{fs}$, $f_{\mathrm{rep}} = 1\,\mathrm{kHz}$). We measure the ultrafast light-induced spin dynamics of the material in a stroboscopic pump-probe experiment, using MSHG as the magnetic probe (see figure 2.1a).

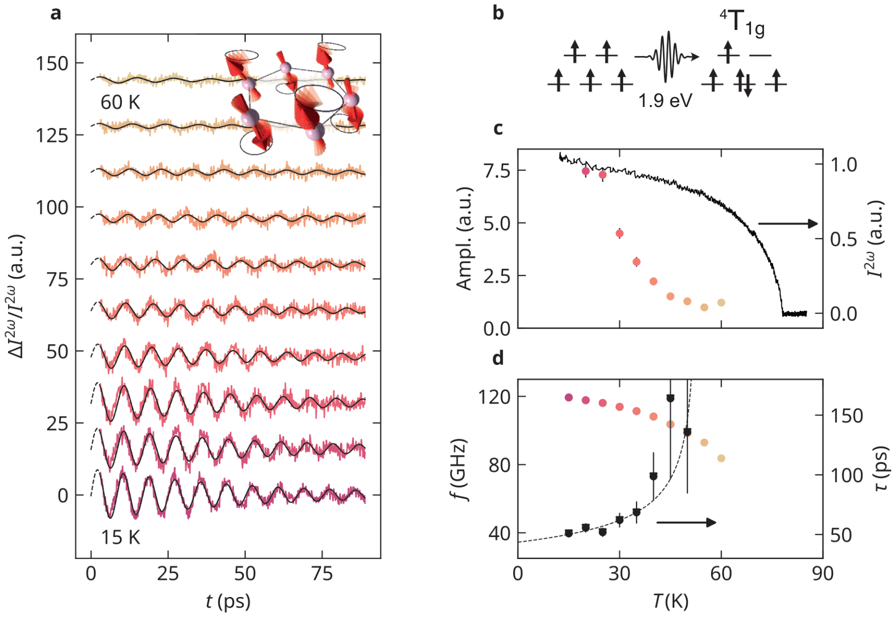

Figure 2.2: **Excitation of a magnon through orbital transitions** **a**. Pump-induced changes in the MSHG intensity in response to excitation with photon energy 1.9 eV and a fluence of 0.9 mJ/cm^2, for temperatures 15–60 K. Non-oscillatory background signal is subtracted. **b**. Single-particle Mulliken notation view of the optical transition excited. **c**. Extracted oscillation amplitude, obtained through best-fit to a damped sine wave in panel *a*. The amplitude is normalized on the total MSHG intensity (black, right axis). **d**. Best-fit oscillation frequency (red, left axis) for each temperature, and the damping time τ (black, right axis), with a dotted line as guide to the eye.

2.3.1. Spin dynamics

Figure 2.2a shows the intensity modulation of the MSHG in response to excitation into ψ_1 (see figure 2.2b), using an incident polarization at which the intensity was maximal. The time-domain signals reveal oscillatory dynamics at a frequency of 119 GHz (0.49 meV), which coincides with the magnon energy gap as measured by neutron scattering [16]. This magnon mode involves the precession of antiferromagnetically oriented spins causing a deviation of the Néel vector **N** from its equilibrium orientation.

Approaching the magnetic phase transition from low temperatures (see figure 2.2d), we observe the mode slowing down along with a reduction of the order parameter, as is typical for soft modes in the vicinity of phase transitions [28]. Surprisingly, the amplitude of the magnon decays at a temperature rate much faster than both the frequency and the magnetic order itself, and vanishes at about 50 K, significantly lower than $T_\mathrm{N} = 78\,\mathrm{K}$ (figure 2.2c). Furthermore, the oscillation lifetime markedly increases as we approach this same sub-T_N temperature (figure 2.2d), a highly unusual behavior for magnons. These temperature dependencies can arise either due to changes in the cross-section of the detection or excitation process, or in the dynamical properties of the material itself. In support of the latter, sub-T_N features have been observed in lattice vibrations [29], elastic losses [22], spin correlations [30, 31] and magnetic susceptance [32]. Mounting evidence points to the presence of critical behavior of the type usually associated with the XY model. In this picture, the otherwise isotropic Heisenberg system is pushed into the XY universality class by a small in-plane anisotropy, in which bound spin vortex pairs are predicted to form below a temperature $T_\mathrm{KT} \approx 55\,\mathrm{K} < T_\mathrm{N}$ [30, 31]. Free vortices at $T > T_\mathrm{KT}$ might be connected to our observation of a rapid decrease of the oscillation amplitude with temperature, and the damping anomalies (figure 2.2b), as they significantly modify spin correlations.

2.3.2. Photon energy dependence

To confirm the resonant character of the magnon excitation, we varied the photon energy of the excitation pulse across the $\psi_0 \rightarrow \psi_1$ resonance and monitored the amplitude of the magnon mode. We observe a magnon amplitude only when the photon energy lies within the absorption line, whereas spin dynamics are absent when exciting at energies below the orbital resonance (0.89 eV and 0.95 eV), as shown in figure 2.3. The immediate and phase-coherent spin dynamics launched via the excitation of the orbital resonance

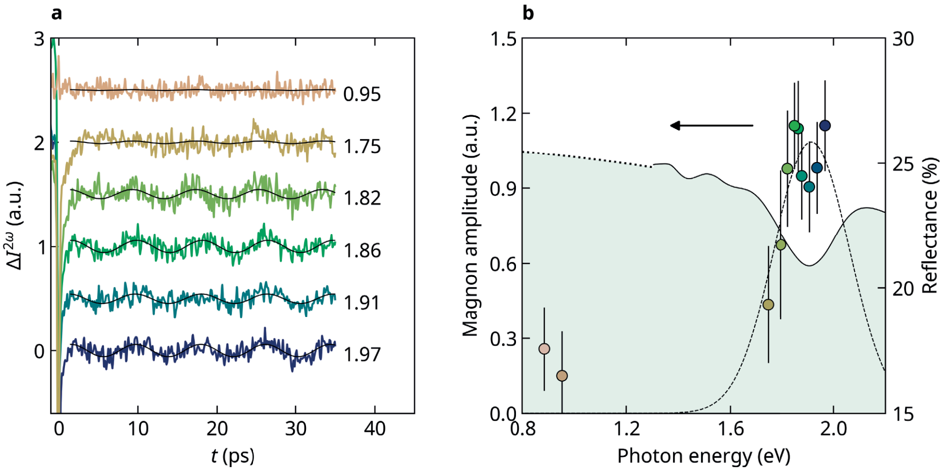

Figure 2.3: **Pump photon energy dependence of the magnon amplitude** **a**. Time-traces of the MSHG intensity changes in response to excitation with pump pulses of central photon energies in the range 0.88 eV to 1.97 eV, using constant fluence of 0.9 mJ/cm^2 and adjusting for reflection losses. Non-oscillatory background is subtracted, and the traces are offset. The oscillation amplitude, obtained by a fit to a Lorentzian centered at $f \approx 120$ GHz. To within noise, the magnon is only excited at the orbital transition, visible as a broad feature around 1.9 eV in the reflectance measurement (shaded green; dotted line denotes extrapolation).

points to a direct impact of the excitation on the spin system. The initial phase of the resulting oscillations is close to zero, indicating that the spins oscillate about their equilibrium directions. This is expected if the dynamics are initiated by an impulsive force, consistent with the short lifetime of the ψ_1 state (linewidth of 35 fs, based on figure 2.3b) and inconsistent with a thermal (displacive) excitation mechanism [33]. Furthermore, we find that due to the small absorption coefficient of the orbital transition [34], there is minimal laser-induced heating in our experiments, and thermal effects are only relevant at long timescales (see section 2.4.2).

2.3.3. Orbital excitation mechanism

Our observation that an excitation pulse in resonance with the $\psi_0 \rightarrow \psi_1$ orbital transition can cause spin precession agrees well with demonstrations of selective optical control of magnetism via optical excitation of d–shell transitions in other antiferromagnets [11, 35, 36]. Experimentally it has been determined that the spins in MnPS$_3$, while largely oriented out of plane, are rotated by a few degrees into the plane due to a small easy-plane anisotropy [37]. This is likely caused by a small single-ion anisotropy, which is a second-order perturbative contribution due to spin-orbit coupling with the excited states. Specifically, neglecting higher-energy excited states this contribution is [38]

$$\left\langle \hat{L} \right\rangle = \frac{\left\langle \psi_0 \middle| \hat{L} \middle| \psi_1 \right\rangle \left\langle \psi_1 \middle| \lambda \hat{L} \cdot \hat{S} \middle| \psi_0 \right\rangle}{E_0 - E_1} + \text{c.c.} \tag{2.2}$$

Here λ is the spin-orbit coupling constant. At equilibrium, dipole-dipole interactions favor a Néel vector **N** oriented out of plane, while a small perturbative contribution to $\left\langle \hat{L} \right\rangle$ together with spin-orbit coupling amounts to a single-ion anisotropy that favors in-plane spins. The competition is resolved with a small tilt of the spins into the plane. Photoexcitation disturbs this competition by creation a population of orbital triplets, such that the statistical expectation is $\left\langle \hat{L} \right\rangle = n \left\langle \psi_1 \middle| \hat{L} \middle| \psi_1 \right\rangle$ with n the concentration of the excited state. This amounts to an impulsive torque on **N** and causes spin precession, akin to previous observations in $\mathrm{NiPS_3}$ [11].

2.4. Lattice excitation

Having demonstrated that excitation of an orbital transition leads to phase coherent spin dynamics, we consider the effect of resonant lattice excitation on the magnetic state. For the excitation of optical phonons, whose energies are much lower than the orbital transitions, we generate intense low-energy pulses: Using two pulses produced by a pair of optical parametric amplifiers, we perform difference frequency mixing in a 350 µm thick GaSe crystal. We measure a fluence of 9.4 mJ/cm^2 at the sample position. The highest-energy phonon modes around 75 meV involve atomic motions within the ethane-like $[\mathrm{P_2\,S_6}]^{4-}$ complexes [39] (see inset to figure 2.4a). Importantly, these modes do not involve motion of the $\mathrm{Mn^{2+}}$ ions, and therefore preserves the distance between the adjacent magnetic ions, leaving their magnetic dipole-dipole interaction unperturbed to first order. Qualitatively, the coupling of phonons to spins should then occur only via the crystal field experienced by individual $\mathrm{Mn^{2+}}$ ions.

2.4.1. Spin dynamics

Figure 2.4a shows the change in MSHG, $\Delta I^{2\omega}$, in response to long-wavelength excitation, for three different temperatures. Close to the transition temperature, we observe a quenching of the MSHG signal, with an exponential decay of about 30 ps. Note that this quench-

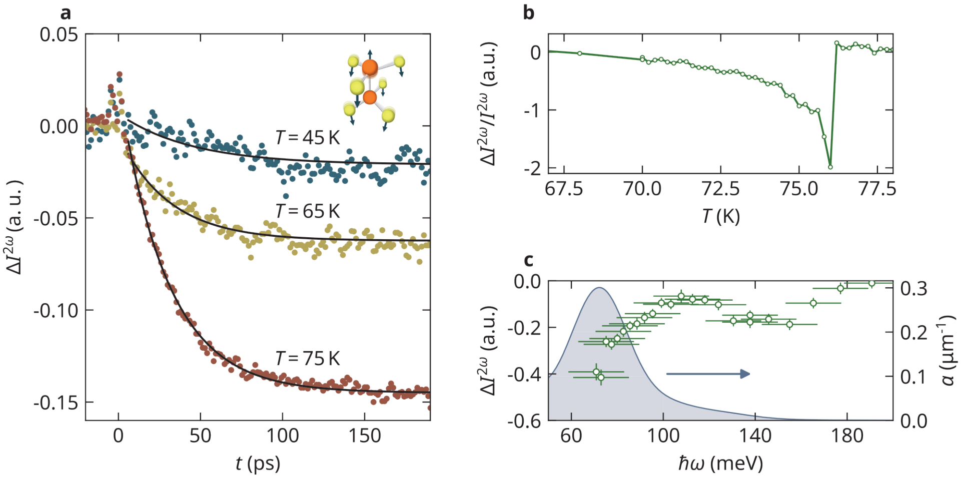

Figure 2.4: **Magnetic quenching by phonon excitation** **a**. Time trace of the spin dynamics induced by phonon pumping at three different temperatures. The inset illustrates the atomic motions of this mode. **b**. The change in MSHG measured at the fixed time delay of 60 ps, as a function of temperature, in resonance with the optical phonon. **c**. The MSHG signal 60 ps after excitation, measured as a function of pump photon energy at 75 K. Horizontal bars indicate the pump bandwidth. The data has been scaled to account for reflection losses. The absorption coefficient, based on FTIR measurements of a similar crystal of $MnPS_3$, is shown in the background.

ing significantly exceeds the period of coherent spin precession (8.4 ps), signifying thermally driven and phase-incoherent spin dynamics. Furthermore, we find that the signal does not recover completely between laser pulses, leading to an accumulated offset in the signal at negative pump-probe delay (amounting to a slightly elevated sample temperature). This implies that the quenched state lasts for at least one millisecond, until arrival of the next pulse. At lower temperatures however, this quenching vanishes almost completely. We note that such heat accumulation was not observed when exciting the orbital transition, further confirmation that significant heating does not occur in that case.

2.4.2. Temperature dependence

To capture a detailed temperature dependence of the quenching magnitude, we fixed the pump-probe delay at 60 ps and track the pump-induced signal ($\Delta I^{2\omega}$) as the sample was cooled down (see figure 2.4b). The quenching approaches zero at low temperatures and rises sharply close to the Néel transition. This observation is a clear indication that although the lattice excitation quenches the Néel order in $MnPS_3$, these changes are thermal in nature.

We can estimate the temperature rise ΔT induced by optical absorption under the assumption that all the absorbed energy is converted into heat. Then we identify the heat Q with the absorbed energy $U = U_0(1 - R)(1 - \mathrm{e}^{-\alpha d})$, where U_0 is the incident laser pulse energy, α is the absorption coefficient, d is the sample thickness and R is the reflectance. Using the specific heat capacity measurements from reference [40] and the excited volume based on the sample thickness and laser spot size, we can use the relation

$$U = Q = \int_{T_0}^{T_0+\Delta T} C(T)\,\mathrm{d}T \approx C(T_0)\Delta T \tag{2.3}$$

where C is the heat capacity. This gives a value of $\Delta T = 7.4\,\mathrm{K}$ for phonon pumping (75 meV). This evinces a stark difference between the orbital and the phonon excitation: When pumping the orbital transition, the estimated temperature change is only $\Delta T = 0.1\,\mathrm{K}$.

2.4.3. Photon energy dependence

Next, we varied the pump photon energy, and tracked the total intensity ($I^{2\omega}$) of the MSHG at a fixed pump-probe delay of 0.6 ns, shown in figure 2.4c. Sufficiently close to the optical phonon frequency, there is large magnetic quenching, while at higher energies this does not occur, except around 150 meV where some additional weaker absorption bands may exist. We thereby conclude that the dynamics are mediated by the population of optical phonons.

2.4.4. Phonon excitation mechanism

The slow timescale of the quenching dynamics, together with the dependence on the pump photon energy, supports a thermal origin of the magnetic quenching. We argue that because of the sphericity of the Mn^{2+} electrons, there is no orbital angular momentum to mediate a correlation between atomic displacements and spin orientation. This is corroborated by an isotropic magnetic susceptibility above the Néel temperature [41], and the low value of single-ion anisotropy of Mn^{2+} reported from electron spin resonance measurements [20, 42]. Consequently, perturbations of the crystal field are largely decoupled from the spins. Instead, the absorbed energy is dissipated into lower frequency phonons that heat the lattice via phonon-phonon scattering, producing an incoherent phonon population at an elevated temperature $T > T_N$. As the heat capacity of the crystal lattice is generally much higher than that of the spin system, the lattice acts akin to a bath whose temperature is promptly increased, in turn melting the magnetic order [43]. These conclusions are also in line with recent experiments on yttrium iron garnet, where resonant phonon excitation also leads to partial quenching of the ferrimagnetic order [44]. The long recovery time of the melted state could be explained by a low value of interplane heat conduction of $MnPS_3$, typical for layered van der Waals crystals [45]. We remark that excitation of lower energy Raman-active phonons, which specifically target atomic motions within the super-exchange Mn-S-Mn bonds, might couple more strongly to the magnetic order. While these modes could be activated through rectification of the infrared-active phonon [12, 46], we see no evidence of this occurring in our experiments. The weak structural correlation of the infrared-active and Raman-active phonons in transition-metal phosphorous trisulfides probably excludes their coupling [39], so that electronic Raman scattering might be a more feasible way to excite the low-energy phonons.

2.5. Conclusion

In summary, we have considered the antiferromagnet $MnPS_3$ whose electrons have zero orbital angular momentum, and excited distinct sub-systems (magnetic Mn^{2+} ions and crystal lattice) while probing the time-evolution of the spins. Excitation of a singlet-triplet orbital transition of the Mn^{2+} electrons activate the zone-center magnon, whereas lattice excitation leads to quenching of spin order. We argue that the orbital singlet Mn^{2+} ground state prohibits spin-lattice coupling, but that by bringing the magnetic ion out of the singlet ground state, the electrons can interact with the lattice and experience a transient magnetic anisotropy, evidenced by coherent spin evolution. Our results indicate that in insulating magnets with highly spherical magnetic ions, such as Mn^{2+} and Fe^{3+}, orbital transitions are the more viable paths to achieve resonant opto-magnetic control. Other in-gap states, such as spin-coupled excitons, have been fruitful as excitation targets for spin dynamics in other systems [47, 48], and should also be considered in $MnPS_3$ [34].

2.6. Contributions

Experiments and data analysis were done by M. Matthiesen, in dialogue with J. R. Hortensius and D. Afanasiev. The sample was grown by S. Mañas-Valero. For the estimates of the temperature rise, another sample was grown by D. Dumcenco and E. Giannini, with FTIR measurements done by I. Kapon and A. Kuzmenko.

2.7. Data availability

The datasets generated during the current study, and the data presented in the figures, is available in a Zenodo repository, 10.5281/zenodo.7526274.

References

1. Matthiesen, M. *et al.* Controlling Magnetism with Light in a Zero Orbital Angular Momentum Antiferromagnet. *Physical Review Letters* **130** (Feb. 17, 2023).
2. Jungwirth, T. *et al.* Antiferromagnetic Spintronics. *Nature Nanotechnology* **11** (2016).
3. Vaz, C. A. Electric Field Control of Magnetism in Multiferroic Heterostructures. *Journal of Physics: Condensed Matter* **24** (2012).
4. Liu, L. *et al.* Current-Induced Magnetization Switching in All-Oxide Heterostructures. *Nature Nanotechnology* **14** (2019).
5. Sapozhnik, A. A. *et al.* Manipulation of Antiferromagnetic Domain Distribution in Mn_2Au by Ultrahigh Magnetic Fields and by Strain. *physica status solidi (RRL)–Rapid Research Letters* **11** (2017).
6. Lee, J. H. *et al.* A Strong Ferroelectric Ferromagnet Created by Means of Spin–Lattice Coupling. *Nature* **466** (2010).
7. Němec, P. *et al.* Antiferromagnetic Opto-Spintronics. *Nature Physics* **14** (2018).
8. Kirilyuk, A. *et al.* Ultrafast Optical Manipulation of Magnetic Order. *Reviews of Modern Physics* **82** (2010).
9. Pershan, P. S. *et al.* Theoretical Discussion of the Inverse Faraday Effect, Raman Scattering, and Related Phenomena. *Physical review* **143** (1966).
10. Baierl, S. *et al.* Nonlinear Spin Control by Terahertz-Driven Anisotropy Fields. *Nature Photonics* **10** (2016).
11. Afanasiev, D. *et al.* Controlling the Anisotropy of a van Der Waals Antiferromagnet with Light. *Science Advances* **7** (2021).
12. Disa, A. S. *et al.* Polarizing an Antiferromagnet by Optical Engineering of the Crystal Field. *Nature Physics* **16** (2020).
13. Xing, W. *et al.* Magnon Transport in Quasi-Two-Dimensional van Der Waals Antiferromagnets. *Physical Review X* **9** (2019).
14. Alliati, I. M. *et al.* Relativistic Domain-Wall Dynamics in van Der Waals Antiferromagnet $MnPS_3$. *npj Computational Materials* **8** (2022).
15. Shan, J.-Y. *et al.* Giant Modulation of Optical Nonlinearity by Floquet Engineering. *Nature* **600** (2021).
16. Wildes, A. R. *et al.* Spin Waves and the Critical Behaviour of the Magnetization in $MnPS_3$. *Journal of Physics: Condensed Matter* **10** (1998).

17. Yagotintsev, K. A. *et al.* Interlayer Mn–Mn Exchange Parameter in $MnPS_3$ from x-Ray Diffraction Data. *Low Temperature Physics* **38** (2012).

18. Chu, H. *et al.* Linear Magnetoelectric Phase in Ultrathin $MnPS_3$ Probed by Optical Second Harmonic Generation. *Physical Review Letters* **124** (2020).

19. Long, G. *et al.* Persistence of Magnetism in Atomically Thin $MnPS_3$ Crystals. *Nano letters* **20** (2020).

20. Okuda, K. *et al.* Magnetic Properties of Layered Compound $MnPS_3$. *Journal of the Physical Society of Japan* **55** (1986).

21. Khomskii, D. *Transition Metal Compounds* 1. publ (Cambridge University Press, Cambridge, 2014).

22. Šiškins, M. *et al.* Magnetic and Electronic Phase Transitions Probed by Nanomechanical Resonators. *Nature Communications* **11** (2020).

23. Fiebig, M. *et al.* Second-Harmonic Generation as a Tool for Studying Electronic and Magnetic Structures of Crystals: Review. *Journal of the Optical Society of America B* **22** (2005).

24. Ni, Z. *et al.* Direct Imaging of Antiferromagnetic Domains and Anomalous Layer-Dependent Mirror Symmetry Breaking in Atomically Thin $MnPS_3$. *Physical review letters* **127** (2021).

25. Ressouche, E. *et al.* Magnetoelectric $MnPS_3$ as a Candidate for Ferrotoroidicity. *Physical Review B* **82** (Sept. 16, 2010).

26. Grasso, V. *et al.* Optical-Absorption Spectra of Crystal-Field Transitions in $MnPS_3$at Low Temperatures. *Physical Review B* **44** (1991).

27. Marciniak, A. *et al.* Vibrational Coherent Control of Localized d–d Electronic Excitation. *Nature Physics* **17** (2021).

28. Van Uijen, C. M. J. *et al.* Dipolar Anisotropy in Quadratic-Layer Antiferromagnets. *Physical Review B* **30** (1984).

29. Sun, Y.-J. *et al.* Probing the Magnetic Ordering of Antiferromagnetic $MnPS_3$ by Raman Spectroscopy. *The Journal of Physical Chemistry Letters* **10** (2019).

30. Rønnow, H. M. *et al.* Magnetic Correlations in the 2D $S = 5/2$ Honeycomb Antiferromagnet $MnPS_3$. *Physica B: Condensed Matter* **276** (2000).

31. Wildes, A. R. *et al.* Static and Dynamic Critical Properties of the Quasi-Two-Dimensional Antiferromagnet $MnPS_3$. *Physical Review B* **74** (2006).

32. Chaudhuri, S. *et al.* Low-Temperature Magnetic Order Rearrangement in the Layered van Der Waals Compound $MnPS_3$. *Physical Review B* **106** (2022).

33. Kalashnikova, A. M. *et al.* Impulsive Excitation of Coherent Magnons and Phonons by Subpicosecond Laser Pulses in the Weak Ferromagnet $FeBO_3$. *Physical Review B* **78** (2008).

34. Gnatchenko, S. L. *et al.* Exciton-Magnon Structure of the Optical Absorption Spectrum of Antiferromagnetic $MnPS_3$. *Low Temperature Physics* **37** (2011).

35. Mikhaylovskiy, R. V. *et al.* Resonant Pumping of d-d Crystal Field Electronic Transitions as a Mechanism of Ultrafast Optical Control of the Exchange Interactions in Iron Oxides. *Physical Review Letters* **125** (2020).

36. Duong, N. P. *et al.* Ultrafast Manipulation of Antiferromagnetism of NiO. *Physical review letters* **93** (2004).

37. Hicks, T. J. *et al.* Magnetic Dipole Splitting of Magnon Bands in a Two Dimensional Antiferromagnet. *Journal of Magnetism and Magnetic Materials* **474** (2019).

38. Bruno, P. Tight-Binding Approach to the Orbital Magnetic Moment and Magnetocrystalline Anisotropy of Transition-Metal Monolayers. *Physical Review B* **39** (Jan. 1, 1989).

39. Joy, P. A. *et al.* Infrared (700–100 cm^{-1}) Vibrational Spectra of the Layered Transition Metal Thiophosphates, MPS_3 (M = Mn, Fe and Ni). *Journal of Physics and Chemistry of Solids* **54** (Mar. 1, 1993).

40. Takano, Y. *et al.* Magnetic Properties and Specific Heat of MPS_3 (M = Mn, Fe, Zn). *Journal of Magnetism and Magnetic Materials* **272** (2004).

41. Joy, P. A. *et al.* Magnetism in the Layered Transition-Metal Thiophosphates MPS_3 (M = Nn, Fe, and Ni). *Physical Review B* **46** (1992).

42. Cleary, D. A. *et al.* Analysis of the ESR Spectrum of Manganese (II) in the Layered Compound $Cd_2P_2Se_6$. *Chemical physics* **106** (1986).

43. Kimel, A. V. *et al.* Ultrafast Quenching of the Antiferromagnetic Order in $FeBO_3$: Direct Optical Probing of the Phonon-Magnon Coupling. *Physical review letters* **89** (2002).

44. Maehrlein, S. F. *et al.* Dissecting Spin-Phonon Equilibration in Ferrimagnetic Insulators by Ultrafast Lattice Excitation. *Science advances* **4** (2018).

45. Minnich, A. J. Exploring the Extremes of Heat Conduction in Anisotropic Materials. *Nanoscale and Microscale Thermophysical Engineering* **20** (2016).

46. Afanasiev, D. *et al.* Ultrafast Control of Magnetic Interactions via Light-Driven Phonons. *Nature Materials* **20** (2021).

47. Belvin, C. A. *et al.* Exciton-Driven Antiferromagnetic Metal in a Correlated van Der Waals Insulator. *Nature communications* **12** (2021).

48. Kang, S. *et al.* Coherent Many-Body Exciton in van Der Waals Antiferromagnet $NiPS_3$. *Nature* **583** (2020).

3

Ferromagnetic photocarriers in an antiferromagnetic manganite

In doped manganite systems, a competition between antiferromagnetic and ferromagnetic order exists and is tied to electronic delocalization. Here we use an optical scheme to impulsively photodope the antiferromagnetic parent manganite system $CaMnO_3$ and measure the formation dynamics of a long-range ferromagnetic state. We target charge-transfer electronic transitions in $CaMnO_3$ to photodope the magnetic ions and probe the subsequent dynamics of both charges and spins, combining time-resolved terahertz spectroscopy and magneto-optical measurements. We demonstrate that photodoping promotes a long-lived population of delocalized electrons and induces a net magnetization, effectively promoting ferromagnetism resulting from double-exchange interactions between photoexcited manganese ions. The picosecond onset time of the magnetization, much longer than the electron timescale, as well as the presence of an excitation threshold, are consistent with the formation of a phase-separated state of ferromagnetic patches in an antiferromagnetic background.

This chapter is based on Hortensius et al. [1], "Ultrafast activation of the double-exchange interaction in antiferromagnetic manganite".

The perovskite manganites, $XMnO_3$, is a class of materials exhibiting a broad range of behaviors, most famously the colossal magnetoresistance of the $La_{1-x}Ca_xMnO_3$ series [2]. The end member of this series—$CaMnO_3$—is an antiferromagnetic (AFM) insulator. With its half-filled t_{2g} orbitals, charge localization is largely a consequence of strong on-site Coulomb repulsion, U. As is common among the perovskite oxides, this ground state is nearly degenerate with competing phases, giving rise to rich phase diagrams [3]. This makes the manganites suitable for phase control experiments, be it through electric fields [4, 5], strain effects [6], or chemical doping [7].

Photoexcitation above the spectral gap of an insulator produces a nonequilibrium population of quasiparticles. This process, referred to as *photodoping*, can be used as an alternative to chemical substitution, offering several advantages: it is time-resolved (when using pulsed light), it does not directly alter the crystal structure, and the amount of doping is a simple function of the intensity of the light. Early experiments on a charge-ordered antiferromagnetic insulator—$Pr_{0.7}Ca_{0.3}MnO_3$—demonstrated that photoexcitation can trigger a fast metallization [8, 9] that melts not only the charge order but also the magnetic order, on subpicosecond timescales. This discovery inspired many studies on the effects of photodoping on the orbital and magnetic order of correlated manganite systems on timescales down to a picosecond [10–15].

Manipulation of the magnetic order has been studied extensively in manganite systems whose ground states are ordered, and photoexcitation is followed by a melting of this order [10–15]. We here investigate $CaMnO_3$ (see figure 3.1a), in which charge- and orbital order is *absent* in the ground state. In this case, the photoexcited electrons are the only charge carriers experiencing the double-exchange interaction in the photoinduced transient state. This allows one to decouple and rule out some strong correlation effects as the driving force for the emergence of net magnetization and to study the intrinsic magnetic timescales. We target highly absorbing charge-transfer transitions between the oxygen and manganese ions (see figure 3.1b) in an epitaxial thin film of $CaMnO_3$, and find that this photodoping introduces delocalized electrons, leading to the emergence of a nonthermal magnetization on picosecond timescales. We also observe a critical number of photons required to observe this collective response, and discuss the possible contributions of both uniform (i.e. coherent) and inhomogeneous (i.e. incoherent) scenarios to the ultrafast magnetization and argue that the ultrafast photodoping results in an inhomogeneous phase-separated state (see figure 3.1b).

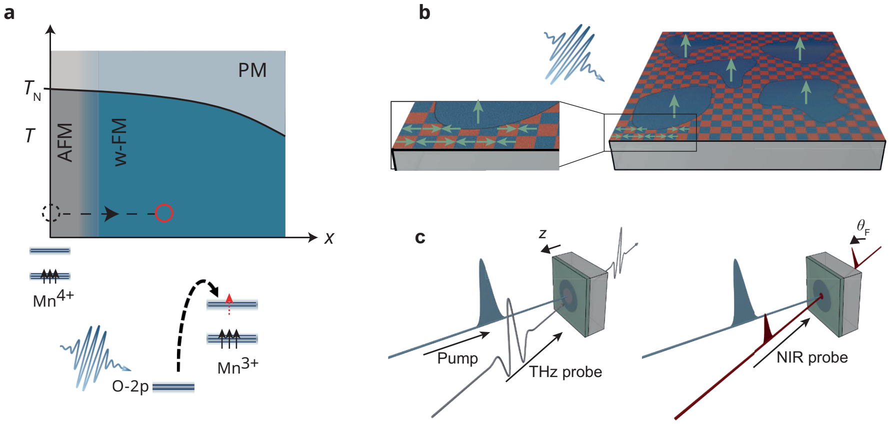

Figure 3.1: **Ultrafast photodoping of CaMnO$_3$ thin films** **a.** (top) Schematic temperature (K)–doping concentration (x) phase diagram of electron-doped CaMnO$_3$. Upon doping, the material becomes metallic and weakly ferromagnetic. (bottom) A tunable ultrashort pulse excites charge-transfer transitions between the oxygen and Mn-ions. **b.** The single-valence Mn^{4+} (d^3) spins in CaMnO$_3$ are ordered antiferromagnetically in the plane. Upon chemical or ultrafast electron doping, a macroscopic net magnetic moment emerges in the z-direction. The net magnetic moment is either the result of uniform spin canting or ferromagnetic droplets in a collinear AFM background. **c.** Schematic of the experiment: The tunable ultrashort pulse (blue) excites an ultrathin CMO film on YAlO$_3$ (001). The induced electron and magnetic dynamics are measured by THz pulses (grey, left) and polarization rotation (θ_F) and transmission changes of the NIR probe pulse (red, right) respectively.

3.1. Calcium manganite

While $CaMnO_3$ is an insulator, with only very modest electron doping it turns metallic and ferromagnetic. The substitution of Ca^{2+} with Ce^{4+} introduces two electrons ($2e$) into the conduction band. At the low doping levels at which conduction appears, screening of the repulsion U by the introduced carriers cannot be the cause of the metallicity. Instead, the ion substitution results in a mixed-valence (Mn^{3+}, Mn^{4+}) charge-ordered structure, which allows for *double-exchange* interaction between the manganese ions. This interaction promotes both electron hopping and gives rise to conduction. Importantly, the double-exchange interaction also favors parallel alignment of spins, in contrast to the *superexchange* interaction which favors antiparallel alignment, and is the reason the insulating ground state is antiferromagnetic.

The competition between double- and superexchange interactions reaches a compromise in the doped manganites as shown in figure 3.2, producing a weakly ferromagnetic phase. However, this compromise can be reached in two ways (see figure 3.2c): In the Ce-doped $CaMnO_3$, neighboring spins develop a relative angle with respect to each other—the *spin canting angle*, which can exceed 10° [16, 17], giving rise to a sizeable net magnetization along the crystallographic z-direction. In La- and Y-doped $CaMnO_3$, a spatial phase-separation occurs, with ferromagnetic and antiferromagnetic regions coexisting [18–20]. These two scenarios, (i) a homogeneously canted AFM state and (ii) phase segregation into regions with collinear antiferromagnetic order and ferromagnetic clusters, are clearly distinct [21]. The distinction raises the question on the dominant mechanism enabling ultrafast photo-induced dynamics: uniform spin canting or inhomogeneous phase segregation.

3.1.1. Thin film sample

Compressively strained, 100 nm thick films $CaMnO_3$ (CMO) were grown on a $YAlO_3$ (YAO) substrate using pulsed laser deposition, as detailed in Vistoli et al. [22]. Undoped bulk CMO adopts an orthorhombic perovskite *Pbmn* crystal structure. The superexchange interaction between neighboring Mn^{4+} ions gives rise to an antiferromagnetic (AFM) ground state below the Néel temperature T_N of about 120 K. The fundamental absorption edge is independent of the magnetic ordering and is located around an energy of 1.3 eV to 1.5 eV [23]. Microscopically it corresponds to the onset of the strongly absorbing charge-

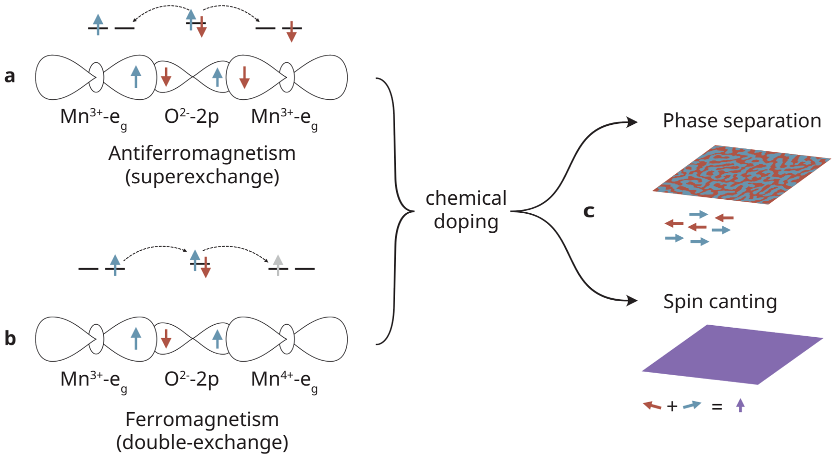

Figure 3.2: **Competition between superexchange and double-exchange a**. The superexchange mechanism involves virtual hopping between isovalent cations (Mn^{3+}) via oxygen ligands, and favors antiferromagnetic alignment of the cation spins. **b**. The double-exchange mechanism involving real hopping between heterovalent cations (here Mn^{3+} and Mn^{4+}), and favors ferromagnetic alignment between the spins. **c**. In a doped $CaMnO_3$, the competition between the super- and double-exchange mechanisms can resolve itself as either a phase-separated state (top) or a uniform state with a weak ferromagnetic moment (bottom).

transfer transitions from the O-2 p orbitals to the empty Mn-e_g states [24–26]. The YAO substrate is a wide bandgap insulator, with negligible absorption below 5 eV [27], which ensures negligible contribution to the measured transient response.

3.1.2. Terahertz spectroscopy

Time-domain terahertz spectroscopy, in which terahertz pulses are sampled in the time domain using the electro-optic effect [28], can be used to characterize the electronic properties close to the static limit while maintaining time resolution in a pump-probe experiment. Equilibrium spectroscopy of the CMO film on YAO is shown in figure 3.3, at a range of sample temperatures. While the dielectric properties of the material dominate the transmittivity in the terahertz range, the observation of a change in the temperature rate of change for the electric field energy near the Néel temperature T_N indicates a magnetic contribution to the terahertz response (see figure 3.3b), evidencing a significant correlation between spins and phonons, the latter dominating the dielectric function at these frequencies. Substantial spin-phonon coupling in this system has been predicted [29] and measured [30] so that we can attribute this temperature dependence

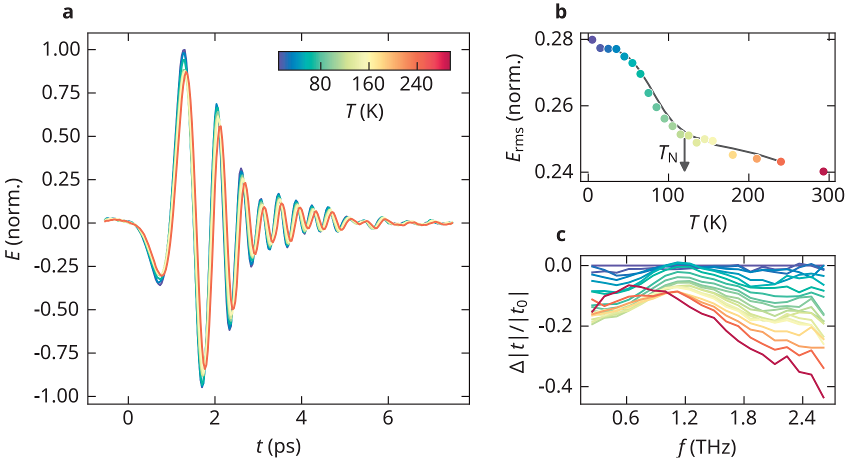

Figure 3.3: **Terahertz spectroscopy of the CaMnO$_3$ thin film** **a**. Electro-optically sampled waveforms, after transmission through the sample at a range of sample temperatures. **b**. The root-mean-square electro-optic signal (E_{rms}), proportional to the pulse energy. The change in slope near the Néel temperature T_{N} is a consequence of a correlation between the magnetic and the electronic or dielectric properties of the material. **c**. The relative change of the transmission magnitude with respect to that at the lowest temperature (5 K).

to changes in the phonon spectrum caused by spin ordering. In figure 3.3c we show the relative change in the transmission magnitude over the frequency content in terahertz pulses. The magnitude is calculated relative to the low-temperature (5 K) data. We find a feature just above 1 THz, present at all temperatures. Spectral features from the substrate are not expected, with phonons in YAO appearing at higher frequencies [31]. A resonance very close to this frequency has been observed in CMO previously [30], and was attributed to a defect mode, which are crystal vibrations localized around defects such as oxygen vacancies [32].

In the following sections, we will use the peak amplitude E_p of these transmitted waveforms to monitor the ultrafast changes in the electronic properties of the CaMnO$_3$ thin film under photodoping. For a nondispersive photoconductivity under the thin film approximation for the transmittivity, we can relate the change in the peak amplitude to the photoconductivity $\Delta\sigma$ of a film of thickness d,

$$\frac{\Delta E_p}{E_p} = -\frac{Z_0 d}{2}\Delta\sigma \tag{3.1}$$

The peak amplitude therefore provides a measure of the photoconductivity of the film, which is proportional to the number of excited carriers.

3.2. Charge-transfer doping

Ultrashort (about 100 fs) pulses of light are used to resonantly excite charge-transfer transitions. The excitation pulses are generated by using both the direct and frequency-doubled output of an optical parametric amplifier (OPA) operating in the infrared spectral range. This enables a tunable excitation pulse in a large energy range 0.8 eV to 2.5 eV ($\lambda = 500$ nm to 600 nm), across the onset of the Mn-O charge-transfer transitions. We used terahertz (THz) time-domain spectroscopy (see figure 3.1c) to measure transient changes in the THz (meV) optical conductivity. To characterize the effect of the photoexcitation on the magnetic order, we additionally measured the pump-induced changes in the transmission and polarization rotation θ of a co-propagating time-delayed, linearly polarized weak probe pulse at 1.55 eV transmitted through the sample (see figure 3.1c). The rotation of this near-infrared (NIR) light is related to the out-of-plane magnetization $\mathbf{M}$ due to the magneto-optical Faraday effect, such that $\theta \propto M$.

Photodoping at an excitation energy of 1.94 eV promptly reduces the amplitude of a THz pulse transmitted through the $CaMnO_3$ film. Figure 3.4a shows the pump-induced change in the peak value of the transmitted THz pulse as a function of the delay time between the probe and the THz pulse. A reduction in the field strength of almost 10% occurs within the first picosecond, which then remains diminished for hundreds of picoseconds. The reduction in the THz amplitude is likely due to increased screening by photoexcited free carriers since the transmission amplitude is inversely proportional to the conductivity [33]. The long-lived screening signifies a metallic state persisting beyond carrier lifetimes, not uncommon for photo-induced metallic states in manganites [10]. To monitor changes to the magnetic state we also tracked the time-resolved rotation θ of the NIR probe polarization that appears in response to photodoping (see figure 3.4b). We observe that there exist magnetic field-dependent and independent components at all temperatures and that the field-dependent component changes upon switching the magnetic field polarity (see the inset to figure 3.4b). Throughout this study, we perform the experiments at two fields of opposite polarity $\pm H$ to eliminate non-magnetic contributions to the polarization rotation and use the difference $\theta_F = \left(\theta(+H) - \theta(-H)\right)/2$ as a measure of the Faraday rotation that emerges in response to the photo-induced magnetization ΔM along the z-direction. Our experiment shows that the growth of magnetization

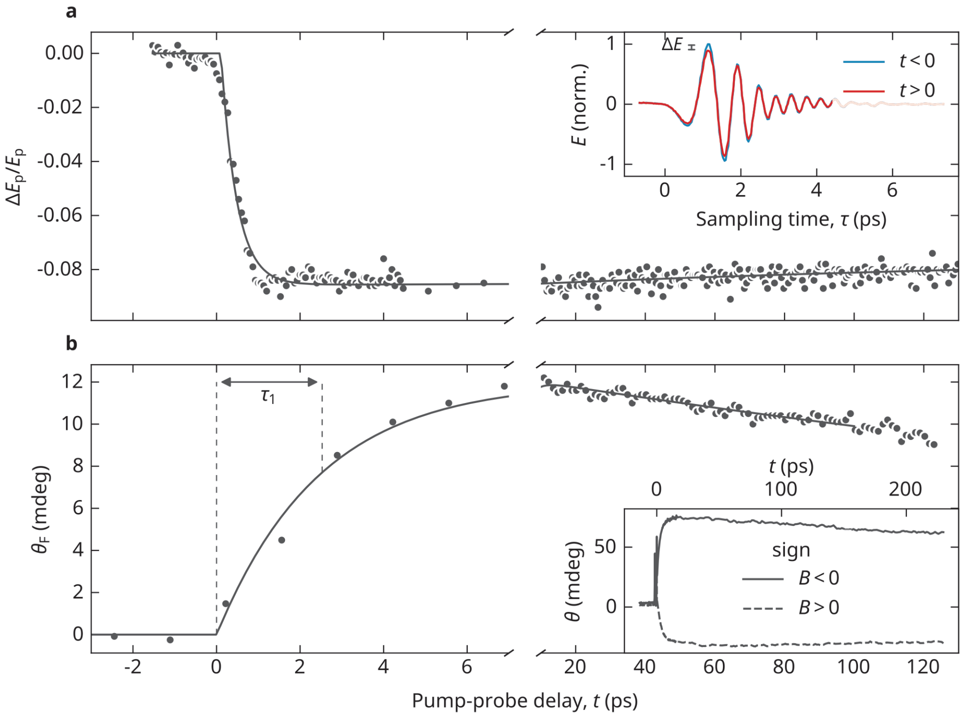

Figure 3.4: **Ultrafast carrier delocalization and magnetization in CaMnO$_3$** **a**. Time-resolved transient change in transmitted THz peak electric field after photodoping (1.94 eV). Inset: Electro-optically detected terahertz transients before (equilibrium) and a few ps after photodoping ($t > 0$). **b.** Faraday rotation θ_F probed by [001]-polarized NIR pulses after photodoping (1.94 eV). The solid line indicates the fit (see text). Inset: Transient polarization rotation θ for oppositely applied magnetic fields, here at 90 K.

occurs over a few picoseconds. After this, the signal decays exponentially on a nanosecond timescale. To track the temperature dependence of the time constants, we analyze the data with the following double exponential function:

$$\theta_{\mathrm{F}}(t) = A(1 - e^{-t/\tau_1}) - B(1 - e^{-t/\tau_1})(1 - e^{-t/\tau_2}) \tag{3.2}$$

The first term describes the emergence of a net magnetic component (ΔM) of amplitude A in the out-of-plane direction on a timescale τ_1 (see figure 3.4). The second term describes the partial decay (amplitude B) of the signal on a timescale τ_2.

Applying a magnetic field with a non-zero component in the z-direction is essential: it predefines the direction of **M** in the photoinduced magnetic state. Figure 3.5a shows the amplitude of the long-lived component of the transient photoinduced polarization rotation θ at a delay time of 25 ps as a function of the applied magnetic field. The data reveal a hysteresis loop and a magnetic remanence in the photoinduced state, indicating that not only the induced magnetic moment but also the equilibrium ground state is susceptible to the magnetic field.

Fitting equation (3.2) to the experimental data, we observe a strong temperature dependence of the photoinduced magnetization ΔM, shown in figure 3.5b, with a peak around 90 K and a full disappearance of the signal above 110 K. The latter is close to the Néel temperature T_{N} in the $\mathrm{CaMnO_3}$ thin films [22], another confirmation of the magnetic nature of the measured signal. The non-monotonic temperature dependence can be attributed to the competition between the decrease of both the coercive field and the antiferromagnetic order parameter in the ground state as temperature increases. At low temperatures, the out-of-plane magnetic field used in our experiment (0.1 T) is not sufficient to overcome the coercive field (up to 1.5 T at low temperatures for 4% Ce-doped samples [22]) and bring the sample in a monodomain state; it thus can only align the net magnetic moment in a part of the domains. The coercive field gets smaller at high temperatures, but simultaneously the overall AFM order decreases. The latter leads to a reduction of the transient net magnetization ΔM, which is proportional to this AFM order parameter.

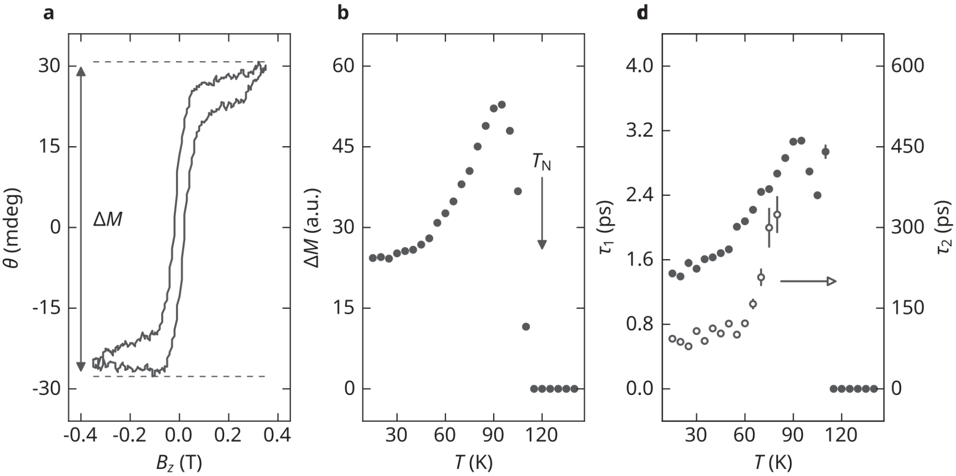

Figure 3.5: **Characterizing the transient net magnetic moment** **a**. Amplitude of the photoinduced polarization rotation at $t \approx 25$ ps, as a function of applied magnetic field out-of-plane. ($T = 105$ K). **b,c**. Amplitude (**b**) emergence time τ_1 and decay time τ_2 (**c**) of the induced magnetic component as a function of temperature, as extracted with fits equation (3.2) to the time-resolved transient Faraday rotation θ_F ($\pm H$) for different temperatures after excitation at a photon energy of 1.55 eV.

3.3. Timescales

Our experiments show the timescale τ_1 over which magnetization ΔM grows following excitation is 1.5 ps at low temperatures and gradually increases to 3 ps close to the transition temperature (see figure 3.5c). We also note that this time does not depend on the density of photogenerated electrons, as we observed no discernible dependence on the pump fluence or pump photon energy in the range 1.2 eV to 2.4 eV. Interestingly, this time is significantly longer than the pump-induced changes to the conductivity, occurring faster than 0.5 ps (see figure 3.4a). This observation evinces a clear distinction between the electronic and magnetic response of the material. At the same time the magnetic response time is still substantially faster than typical spin-lattice relaxation times (about 100 ps), which determines the interaction with the lattice—an angular momentum reservoir. We note that similar decoupling has been reported earlier in thin films of the spin glass $Gd_{0.55}Sr_{0.45}MnO_3$ [12]. We also find that the lifetime τ_2 of the magnetic state diverges in the approach of T_N (see figure 3.5c), similar to the one observed in photodoping experiments on the strongly correlated antiferromagnetic oxide Sr_2IrO_4 [34].

3.4. Excitation conditions

Studying the response of the system to changes in the excitation conditions can help identify the process by which magnetization appears. We studied the magnetic and electronic response of the system when varying two parameters of the excitation pulse: The fluence (intensity) and the photon energy. These measurements are summarized in figure 3.6.

3.4.1. Threshold behavior

Measurements at different excitation fluences F reveal a critical (threshold) fluence F_{th} for the magnetic signal to appear (figure 3.6a). In contrast, there is no threshold present for either the time-resolved THz (see figure 3.6a) or the NIR-probe (see figure 3.6c) transmission measurements, which measure the pump-induced changes to the electronic system. This indicates that while the number of photoexcited electrons is directly proportional to the light intensity, an excitation threshold of around 0.004 electrons per manganese ion (0.4% doping) is required to induce a net magnetization.

3.4.2. Energy selectivity

The susceptibility of the system to excitation is strongly energy-dependent. Defining the experimental photosusceptibility as the ratio between the induced magnetic component ΔM and the fluence used in the experiments, we show in the inset of figure 3.6a the dependence of this quantity on the photon energy of the excitation pulses. We observe peaked susceptibility around 1.5 eV, corresponding to the onset of the charge-transfer bandgap in $\mathrm{CaMnO_3}$ [25]. Specifically, this is the O-2p $\longrightarrow$ Mn-$\mathrm{e_{g\uparrow}}$ transition, with the transition into Mn-$\mathrm{e_{g\downarrow}}$ appearing at higher energies due to the Hund coupling with the $\mathrm{t_{2g\downarrow}}$ spins [24]. The decrease of the signal at higher energies may be a consequence of these transitions being spin-polarized, such that higher energies produce a less spin-polarized photocarrier population. Alternatively, it may be a detection effect resulting from a penetration depth mismatch between the excitation and probing light (1.55 eV).

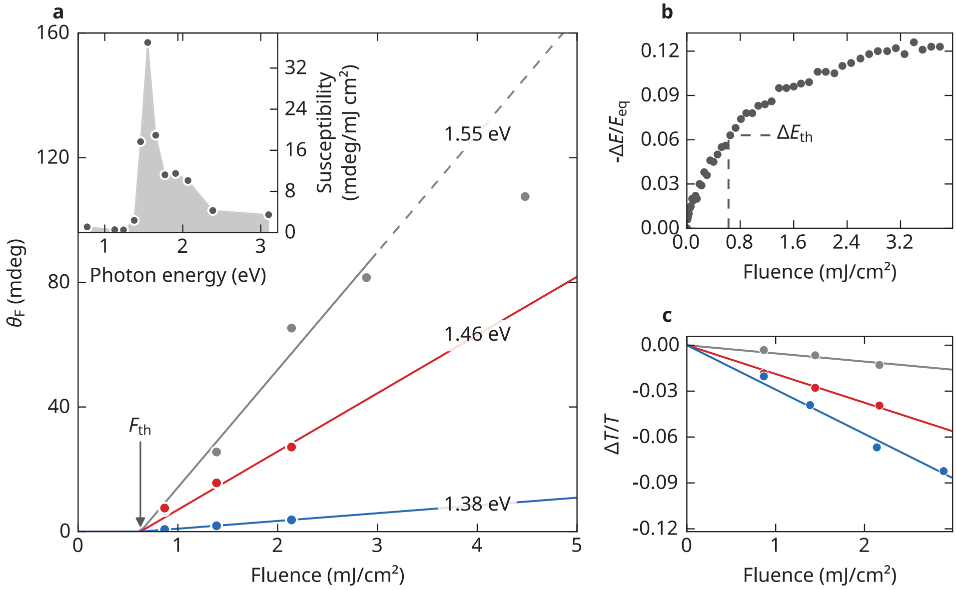

Figure 3.6: **Photodoping selectivity and threshold** **a**. Peak Faraday rotation for different fluences and different excitation photon energies with global linear fits, with shared critical fluence F_{th} for all photon energies. Inset: The resulting susceptibility as a function of the excitation photon energy. **b**. Transient ($t = 10$ ps) change in THz peak electric field transmitted by the $CaMnO_3$ film after excitation at 1.94 eV. **c**. Relative change in sample transmittance as a function of fluence at three photon energies, displaying linear relationship without the threshold behavior of the magnetic signal.

3.5. Nature of the nonequilibrium state

The emergence of equilibrium net magnetization in doped $CaMnO_3$, driven by the double-exchange interaction, can proceed in two distinct ways: (i) in “coherent” process, where electron doping leads to uniform canting of the antiferromagnetic sublattices (as observed in Ce-doped $CaMnO_3$), or (ii) in a phase-separated form, where ferromagnetic droplets appear within an antiferromagnetic background (as seen in La-doped and Y-doped $CaMnO_3$).

In the first scenario, we expect a phase-coherent response on a timescale set by the double-exchange interaction, appearing instantaneous with our experimental resolution. Conversely, our experiments indicate that the transient net magnetic moment arises on a relatively slow timescale. Furthermore, we observe an excitation threshold for the net magnetization to appear, which is absent in the electronic response as measured by THz spectroscopy. A critical threshold is not observed for chemical doping of this material [22], so we do not have this expectation for the photoinduced response.

In the second scenario, there is however some expectation of threshold behavior. The presence of a threshold suggests a metastable nonequilibrium state in which patches of the ferromagnetic phase emerges within the antiferromagnetic background; the threshold fluence corresponds to a type of percolation threshold of these ferromagnetic clusters, whose space filling is a function of the photoexcitation density: At low excitation fluences, the droplets remain below a critical size and cannot develop a magnetic moment, nor a long-range ordering with other ferromagnetic clusters. The mere presence of delocalized electrons is insufficient; a minimum density and size of these droplets are required for interaction and formation of a macroscopic magnetization. The threshold fluence corresponds to a percolation threshold of ferromagnetic clusters required to establish long-range macroscopic magnetic order. The change in THz transmission at the threshold fluence amounts to approximately 40% of the saturation value (see figure 3.6b), suggesting a percolation threshold for the magnetic order around 0.4. This closely aligns with the required site filling probability $p = 0.31$ in 3D cubic networks to establish percolation [35]. The delayed response of the magnetic dynamics in this scenario can be attributed to the mutual alignment of magnetization between individual droplets. The antiferromagnetic background likely plays a crucial role in this process, as the photoinduced magnetization appears exclusively below T_N. This alignment is probably mediated by the emission of elementary spin-wave excitations—magnons—that propagate and establish spin-spin correlations, requiring the equilibrium phase to support such quasi-particles. The strong magneto-crystalline anisotropy inherent to $CaMnO_3$ thin films [22] places the lowest frequency magnons in the sub-THz range, corresponding to the observed timescales of several picoseconds [36].

3.6. Conclusion

In summary, we have investigated the ultrafast response of thin films of the antiferromagnetic manganite $CaMnO_3$ following photoexcitation of the O ⟶ Mn charge-transfer transition. Using time-resolved THz transmission measurements, we detected the presence of a long-lived photoconducting state. Time-resolved Faraday measurements revealed the emergence of a macroscopic net magnetization within the antiferromagnetic film, forming on a timescale slower than the photoconductivity. The magnetization, we argue, is caused by the double-exchange interaction between photoexcited manganese ions, not present at equilibrium. The timescale is attributed to the interaction of ferromagnetic clusters within the AFM background. Our work advances the understanding of ultrafast cooperative phenomena in complex materials characterized by strong interplay among different degrees of freedom. Specifically, we demonstrate the emergence of a nonequilibrium magnetic state under charge-transfer doping that exhibits a threshold behavior not observed with chemical substitution.

3.7. Contributions

M. Matthiesen performed the terahertz measurements and analysis; J. R. Hortensius did the measurements and analysis of the photoexcitation experiments, in collaboration with D. Afanasiev, and wrote the bulk of the paper which this chapter is based on; samples were grown by L. Vistoli.

3.8. Data availability

Source data for figures are publicly accessible at the DOI 10.5281/zenodo.8034595.

References

1. Hortensius, J. R. *et al.* Ultrafast Activation of the Double-Exchange Interaction in Antiferromagnetic Manganites. *APL Materials* **11** (July 7, 2023).
2. Jin, S. *et al.* Thousandfold Change in Resistivity in Magnetoresistive LaCaMnO Films. *Science* **264** (Apr. 15, 1994).
3. Dagotto, E. *et al.* Colossal Magnetoresistant Materials: The Key Role of Phase Separation. *Physics Reports* **344** (Apr. 1, 2001).
4. Mathews, S. *et al.* Ferroelectric Field Effect Transistor Based on Epitaxial Perovskite Heterostructures. *Science* **276** (Apr. 11, 1997).
5. Tanaka, H. *et al.* Giant Electric Field Modulation of Double Exchange Ferromagnetism at Room Temperature in the Perovskite Manganite/Titanate p-n Junction. *Physical Review Letters* **88** (Dec. 27, 2001).
6. Konishi, Y. *et al.* Orbital-State-Mediated Phase-Control of Manganites. *Journal of the Physical Society of Japan* **68** (Dec. 15, 1999).
7. Hwang, H. Y. *et al.* Lattice Effects on the Magnetoresistance in Doped $LaMnO_3$. *Physical Review Letters* **75** (July 31, 1995).
8. Miyano, K. *et al.* Photoinduced Insulator-to-Metal Transition in a Perovskite Manganite. *Physical Review Letters* **78** (June 2, 1997).
9. Fiebig, M. *et al.* Visualization of the Local Insulator-Metal Transition in $Pr_{0.7}Ca_{0.3}MnO_3$. *Science* **280** (June 19, 1998).
10. Takubo, N. *et al.* Persistent and Reversible All-Optical Phase Control in a Manganite Thin Film. *Physical Review Letters* **95** (June 30, 2005).
11. Matsubara, M. *et al.* Photoinduced Switching between Charge and Orbital Ordered Insulator and Ferromagnetic Metal in Perovskite Manganites. *Physical Review B* **77** (Mar. 13, 2008).
12. Matsubara, M. *et al.* Ultrafast Photoinduced Insulator-Ferromagnet Transition in the Perovskite Manganite $Gd_{0.55}Sr_{0.45}MnO_3$. *Physical Review Letters* **99** (Nov. 15, 2007).
13. Miyasaka, K. *et al.* Ultrafast Photoinduced Magnetic Moment in a Charge-Orbital-Ordered Antiferromagnetic $Nd_{0.5}Sr_{0.5}MnO_3$ Thin Film. *Physical Review B* **74** (July 10, 2006).
14. Beaud, P. *et al.* Ultrafast Structural Phase Transition Driven by Photoinduced Melting of Charge and Orbital Order. *Physical Review Letters* **103** (Oct. 9, 2009).
15. Lingos, P. C. *et al.* Correlating Quasiparticle Excitations with Quantum Femtosecond Magnetism in Photoexcited Nonequilibrium States of Insulating Antiferromagnetic Manganites. *Physical Review B* **95** (June 28, 2017).

16. Caspi, E. N. *et al.* Structural and Magnetic Phase Diagram of the Two-Electron-Doped ($Ca_{1-x}Ce_x$)MnO_3 System: Effects of Competition among Charge, Orbital, and Spin Ordering. *Physical Review B* **69** (Mar. 4, 2004).

17. Ohnishi, H. *et al.* Spin-Canting in Lightly Electron-Doped $CaMnO_3$. *Physical Review B* **85** (Apr. 18, 2012).

18. Neumeier, J. J. *et al.* Possible Signatures of Magnetic Phase Segregation in Electron-Doped Antiferromagnetic $CaMnO_3$. *Physical Review B* **61** (June 1, 2000).

19. Ling, C. D. *et al.* Inhomogeneous Magnetism in La-Doped $CaMnO_3$. I. Mesoscopic Phase Separation Due to Lattice-Coupled Ferromagnetic Interactions. *Physical Review B* **68** (Oct. 23, 2003).

20. Sharma, N. *et al.* Phase Separated Behavior in Yttrium Doped $CaMnO_3$<script>. *Materials Research Bulletin* **77** (May 1, 2016).

21. Khomskii, D. *Transition Metal Compounds* 1. publ (Cambridge University Press, Cambridge, 2014).

22. Vistoli, L. *et al.* Giant Topological Hall Effect in Correlated Oxide Thin Films. *Nature Physics* **15** (1 Jan. 2019).

23. Husanu, M.-A. *et al.* Electron-Polaron Dichotomy of Charge Carriers in Perovskite Oxides. *Communications Physics* **3** (1 Apr. 2, 2020).

24. Jung, J. H. *et al.* Determination of Electronic Band Structures of $CaMnO_3$ and $LaMnO_3$ Using Optical-Conductivity Analyses. *Physical Review B* **55** (June 15, 1997).

25. Asanuma, S. *et al.* Relationship between Resistive Switching Characteristics and Band Diagrams of Ti/$Pr_{1-x}Ca_xMnO_3$ Junctions. *Physical Review B* **80** (Dec. 8, 2009).

26. Sotoudeh, M. *et al.* Electronic Structure of $Pr_{1-x}Ca_xMnO_3$. *Physical Review B* **95** (June 27, 2017).

27. Basun, S. A. *et al.* Optical and Photoelectrical Studies of Charge-Transfer Processes in $YAlO_3$:Ti Crystals. *Physical Review B* **54** (Sept. 1, 1996).

28. Koch, M. *et al.* Terahertz Time-Domain Spectroscopy. *Nature Reviews Methods Primers* **3** (June 29, 2023).

29. Hong, J. *et al.* Spin-Phonon Coupling Effects in Transition-Metal Perovskites: A DFT + U and Hybrid-Functional Study. *Physical Review B* **85** (Feb. 15, 2012).

30. Goian, V. *et al.* The Manifestation of Spin-Phonon Coupling in $CaMnO_3$. *Journal of Applied Physics* **117** (Apr. 27, 2015).

31. Morimoto, T. *et al.* Dielectric Absorption Behavior of $YAlO_3$ at Terahertz Frequencies. *Japanese Journal of Applied Physics* **56** (Sept. 14, 2017).

32. Barker, A. S. *et al.* Optical Studies of the Vibrational Properties of Disordered Solids. *Reviews of Modern Physics* **47** (Jan. 1, 1975).

33. Tinkham, M. Energy Gap Interpretation of Experiments on Infrared Transmission through Superconducting Films. *Physical Review* **104** (Nov. 1, 1956).

34. Afanasiev, D. *et al.* Ultrafast Control of Magnetic Interactions via Light-Driven Phonons. *Nature Materials* **20** (2021).

35. Stauffer, D. *et al.* *Introduction to Percolation Theory* Rev. 2. ed., transferred to digital print (Taylor & Francis, London, 2003).

36. Mitsudo, S. *et al.* Submillimeter Wave ESR Measurement of $LaMnO_3$. *Journal of Magnetism and Magnetic Materials. International Conference on Magnetism (Part II)* **177–181** (Jan. 1, 1998).

4

Nanoscale phononic resonators

Control of material properties (e.g., critical temperature, magnetization, conductivity) is regularly achieved with methods that use stress, such as diamond anvil cells or heteroepitaxial strain. Extending this degree of control to high frequencies is desirable, where it can act on the timescales of magnetic and electronic resonances. In this chapter, we use nanoscale acoustic confinement to excite coherent acoustic phonons (dynamical strain) with near-terahertz frequency. We demonstrate that such phonons can easily be excited when breaking the film-substrate epitaxy in the metallic perovskite $SrRuO_3$. Moreover, thermal annealing of the freestanding membranes placed on a substrate with a similar lattice constant dramatically decreases the interfacial acoustic impedance mismatch, evidencing the reformation of chemical bonds and interfacial restructuring.

While phonons are extremely easy to excite—all that is needed is a lighter—the production of a large number of phonons across a macroscopic volume all in phase with each other is less trivial. That involves the entire lattice of atoms oscillating with the symmetry and the frequency of a single phonon mode, known as a *coherent* phonon. With the advent of powerful coherent light sources in the mid- and far-infrared range, direct excitation of some phonons has become possible and has been a fruitful research avenue: Large-amplitude coherent phonons have been used to induce magnetic moments in antiferromagnets [1, 2], metallicity in insulators [3, 4], and a superconducting-like phase in a fullerene [5]. These works involve optical phonons, which, unlike acoustic phonons, involve a change in the relative position of ions within the unit cell. Since the intracell atomic positions are closely tied to the electronic and magnetic structure at equilibrium, optical phonons may seem like the obvious target for optical manipulation of material properties. However, a lesson from high-pressure physics and the material science of heteroepitaxy (*viz.* lattice-mismatched growth) is that *strain* can also modify electronic and magnetic properties. For the complex oxides (ABO_3), much of the physics is determined by the rotational pattern of the oxygen octahedra surrounding the B-atoms, which in turn is coupled to the crystal volume and shape [6]. Coherent acoustic phonons are the dynamical equivalent of strain, corresponding to dynamics of the macroscopic displacement field $\mathbf{u}(\mathbf{r}, t)$ with associated strain $\epsilon = \partial\mathbf{u}/\partial\mathbf{r}$. Thus, one can expect that the excitation of large-amplitude coherent acoustic phonons, especially at high frequencies, will dynamically alter the electronic and magnetic properties of many materials. Provided a mechanism to excite acoustic phonons (see section 4.1), there is another problem that must be solved: The dispersion relation of acoustic phonons is $\omega(\mathbf{q}) = v_s q$, with wavevector $\mathbf{q}$ and speed of sound v_s. Typically, v_s is of order 10 ps/nm, which means that to reach terahertz frequencies, the phonon wavelength must be of order 10 nm. This is much shorter than the wavelength of any optical laser, so some other parameter must determine the wavenumber. The solution explored in this chapter is to set the wavenumber by engineering the boundary conditions for the displacement field $\mathbf{u}$ using a nanoscale acoustic cavity. Thin films epitaxially bound to their substrates do not support confined phonons. The acoustic reflectivity of the substrate-film (sub-film) interface is given by

$$r = \frac{z_{\text{sub}} - z_{\text{film}}}{z_{\text{sub}} + z_{\text{film}}} \tag{4.1}$$

where $z = \rho v_s$ is the acoustic impedance, with ρ the mass density. Since epitaxial growth inevitably involves materials of similar unit cell volume and typically similar mass, the reflection coefficient will be small. Consequently, confined acoustic modes in the film are of low amplitude and short lifetime.

Fortunately, developments in the field of complex oxides have made it possible to produce single-crystal membranes: A few years ago, it was demonstrated that a water-soluble crystal $Sr_3Al_2O_6$ (SAO) can be deposited using pulsed laser deposition and form parts of heterostructures together with ABO_3 complex oxides [7]. The dissolution of this sacrificial SAO layer in water is often sufficient to create free membranes of the insoluble parts of the thin film heterostructure. To date, many properties of such membranes have been studied [8], not least motivated by their unique elastic properties. When stamped onto polymers, these membranes can reach uniaxial strains of several percent as the polymer is stretched [9].

In this chapter, we focus on the study of acoustic phonons under the extreme confinement provided by the freestanding membrane geometry, following the lift-off approach of reference [7], as illustrated in figure 4.7.

4.1. Excitation of coherent acoustic phonons

Optical phonons with an associated dipole moment, the so-called infrared (IR) active phonons, can be excited directly and coherently with optical fields. In isolation, one may not expect that driving these phonons to large amplitudes will have interesting side effects: They preserve crystal symmetry and are generally spectrally isolated at mid-infrared frequencies. Fortunately, due to anharmonicity of interatomic potentials, it is possible to excite symmetric phonons (*viz.* acoustic phonons and Raman-active phonons) indirectly. In earlier work from our group, Hortensius et al. [10] demonstrated indirect excitation of both coherent acoustic and Raman-active optical phonons through resonant driving of an IR mode. Intuitively, when atoms oscillate in an asymmetric potential, a time-average displacement occurs, illustrated in figure 4.1. The dominant anharmonic coupling of the IR phonon Q_{IR} and the symmetric (Raman or acoustic) mode Q is in centrosymmetric solids of the form $U_{\mathrm{anh}} \sim Q_{\mathrm{IR}}^2 Q$. This approach of using IR modes to drive symmetric modes anharmonically has recently come to be known as nonlinear phononics [11]. However, the basic principles were identified half a century ago under the name of ionic Raman scattering [12]. Resonant driving of Q_{IR} requires powerful light sources in the mid-infrared that are not readily available. Fortunately, coherent acoustic phonons

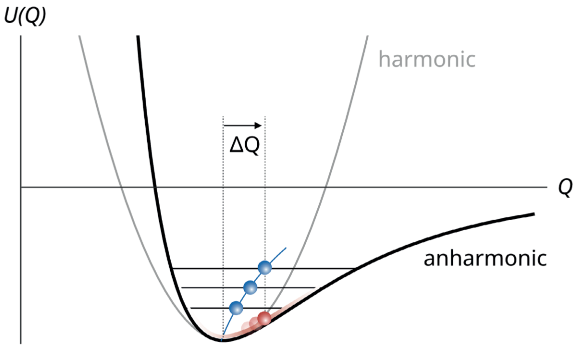

Figure 4.1: **Anharmonic lattice potential** Potential energy U as a function of phonon coordinate Q. *In red*: Driving the mode to large amplitudes in the anharmonic potential produces a time-average displacement ΔQ. *In blue*: Thermal population of phonons produces an energy-average displacement ΔQ

can be excited via electronic transitions through effects that also exist because of anharmonicity. To see the connection between electronic transitions, anharmonicity, and phonons, we begin by considering the cause of thermal expansion in solids.

4.1.1. Thermal expansion

When raising the temperature of a solid, the phonon occupations change in the asymmetric potential, producing a mean displacement as illustrated in figure 4.1. The (non-stationary) stress σ produced by a modified occupation is given by [13]

$$\sigma = -\sum_{\lambda} \Delta n_{\lambda} E_{\lambda} \gamma_{\lambda} \tag{4.2}$$

Here, λ is the quantum number (band, wavevector) of the mode, Δn the change in occupation, $E = \hbar\omega$ the energy of the mode, and γ its Grüneisen parameter. The latter is a measure of the mode anharmonicity defined as a dimensionless quantity of order unity:

$$\gamma_{\lambda} = -\frac{\partial \ln \omega_{\lambda}}{\partial \ln V} = -\frac{V}{\omega_{\lambda}} \frac{\partial \omega_{\lambda}}{\partial V} = -\frac{1}{\omega_{\lambda}} \frac{\partial \omega_{\lambda}}{\partial \epsilon} \tag{4.3}$$

It is clear that $\gamma_\lambda = 0$ for a purely harmonic mode λ because the frequency is independent of the volume (or strain). The macroscopic (or total) Grüneisen parameter γ is the weighted mean of the mode Grüneisen parameters, with the weights given by the volumetric *mode specific heat* (Pa/K),

$$C_\lambda = E_\lambda \frac{\partial n_\lambda}{\partial T} \tag{4.4}$$

The macroscopic Grüneisen parameter is related to the thermal expansion coefficient α and the bulk modulus B through $\gamma = 3\alpha B/C$. Using the above definition of C_λ and inserting it into equation (4.2), we get a thermal stress

$$\sigma = \int_{T_0}^{T} \mathrm{d}T \, \frac{\partial \sigma}{\partial T} = -\int_{T_0}^{T} \mathrm{d}T \, \sum_\lambda \left(\frac{\partial n_\lambda}{\partial T} E_\lambda \right) \gamma_\lambda = -\int_{T_0}^{T} \mathrm{d}T \, \sum_\lambda C_\lambda \gamma_\lambda \tag{4.5}$$

In the simplest models, such as the Debye model, we have $\gamma_\lambda = \gamma$ for all modes λ [14]. Hence,

$$\sigma = -\gamma \int_{T_0}^{T} \mathrm{d}T \, C(T) \approx C(T_0) \Delta T \tag{4.6}$$

Of course, this stress results from a *thermal* population of phonons, not the coherent population created by resonant excitation. If, however, the temperature has a time evolution $\Delta T = \Delta T(t)$ that is sufficiently fast, then macroscopic oscillations—or coherent phonons—may be excited. Considering this vibration as a harmonic oscillator with normal coordinate Q and a generic driving force $Q^{\mathrm{ex}} \propto \sigma(t)$ (such as the temperature change),

$$\frac{\mathrm{d}^2 Q}{\mathrm{d}t^2} + \omega_0^2 Q = \omega_0^2 Q^{\mathrm{ex}}(t) \tag{4.7}$$

To excite any dynamics of Q, it is necessary that Q^{ex} has spectral content at ω_0. In the case of nonlinear phononics, the driving force of the symmetric phonon is the infrared phonon envelope, $Q_{\mathrm{IR}}^2(t)$, which due to its finite rise and decay time has spectral content at the symmetric resonance. As we shall see next, for photoexcitation of electrons, the spectral content comes from the fast response of the electrons and the short timescale of the electron-phonon coupling.

4.1.2. Electronic excitation of stress

Indirect excitation

When electrons are photoexcited, their energy transfers to phonons at a timescale $\tau_{\text{e-p}}$ determined by the strength of the electron-phonon coupling. Consequently, the effective temperature of the phonons rises by $\Delta T = E/C_p V$ with E the absorbed laser energy, C_p the phononic specific heat, and V the excited volume. The corresponding *thermoelastic stress* is $\sigma = -\gamma_p C_p \Delta T$. This process of acoustic phonon excitation is *indirect*, in that the electrons act as an intermediator between the laser field and the phonon temperature. The phonons will heat up on the timescale $\tau_{\text{e-p}}$. Following Voisin et al. [15], we can model the force term of equation (4.7) as

$$Q_p^{\text{ex}} = Q_{0,p}\left(1 - e^{-t/\tau_{\text{e-p}}}\right) \tag{4.8}$$

This has the following solution:

$$Q_p^{\text{ex}}(t) = -\frac{Q_{0,p}}{\omega_0^2\sqrt{1 + (\omega_0\tau_{\text{e-p}})^2}}\cos(\omega_0 t + \phi) \tag{4.9}$$

The phase is $\phi \approx \tan^{-1}(\omega_0\tau_{\text{e-p}})$. This cosinusoidal response results from a step-like driving force and is known as *displacive* excitation.

Direct excitation

Before electrons transfer energy to other subsystems, they can exert stress directly. Consider that electronic states also have a finite Grüneisen parameter, a direct consequence of Pauli's exclusion principle, which creates a *degeneracy pressure* (or "exchange pressure") [16]—no wonder, since not only ionic but also electronic degrees of freedom set the interatomic potentials. Consequently, equation (4.2) also applies to electrons. As shown in the illustration of figure 4.1, the electronic excitation will modify the potential energy rather than the phonon distributions or displacements, setting up new equilibrium positions for the ions and causing macroscopic oscillations of the lattice. The most common manifestations of electronic stress are when the photoexcited carriers are (i) distributed thermally in a metal or (ii) accumulated at a band edge in an insulator:

(i) *Hot electron pressure*. Photoexcited electrons quickly (<100 fs) form a Fermi-Dirac distribution with an effective temperature $T_e > T_0$ via scattering (e.g. *e*-*e* collisions, impact ionization). The hot electron gas exerts a stress $\sigma = -\gamma_e C_e \Delta T_e$, with C_e the volumetric electronic specific heat and γ_e the total electronic Grüneisen parameter. At short timescales, before electron-phonon thermalization, the electron temperature can reach high temperatures, as can the specific heat $C_e \propto T_e$ [14] so that this can be a significant source of stress [17] despite $C_e/C_p \ll 1$ at ambient conditions.

(ii) *Deformation potential*. In insulators, the photoexcited distribution n will peak at the band gap E_g. equation (4.2) reduces to the simple form $\sigma = n_{\text{ex}}\mathcal{D}_g$, with n_{ex} is the number of excited electrons and $\mathcal{D}_g$ the *deformation potential* for the conduction band [13] defined as $\mathcal{D}_\lambda = (\partial E_\lambda/\partial \epsilon) = -\gamma_\lambda E_\lambda$. The real-space picture of this effect is that excited electrons will populate anti-bonding orbitals, which exert a force on the ions.

These are just specific cases of stress following a change in the occupation of electronic levels according to equation (4.2). The experiments of this chapter will involve a metallic system, $SrRuO_3$, such that photoexcitation causes the creation of a hot electron population. For the hot electron pressure effect, the electrons will reach T_e near-instantaneously and decay on the timescale of $\tau_{\text{e-p}}$. We can then model the force term as

$$Q_e^{\text{ex}}(t) = Q_{0,e}e^{-t/\tau_{\text{e-p}}} \tag{4.10}$$

with $Q_e^{\text{ex}} = 0$ for $t < 0$. The solution equation (4.7) is

$$Q_e^{\text{ex}}(t) = \frac{\tau_{\text{e-p}}Q_{0,e}}{\omega_0\sqrt{1+(\omega_0\tau_{\text{e-p}})^2}}\sin(\omega_0 t + \phi) \tag{4.11}$$

Provided that $\phi \approx 0$ ($\omega\tau_{\text{e-p}} \ll 1$), the response is sinusoidal—a consequence of an impulsive driving force.

4.2. Removal of epitaxy

We compare the acoustic properties of a complex oxide pinned to a substrate to one transferred using the soluble sacrificial layer method. We choose strontium ruthenate ($SrRuO_3$) as the material. Among the perovskite oxides, $SrRuO_3$ is the only one that not only conducts electricity but also spontaneously magnetizes to form a ferromagnetic ground state at low temperature. While it does conduct reasonably well, it is nevertheless a ceramic material with complexities that distinguish it from ordinary metals, such as having a Fermi wavelength and electron mean free path of similar magnitude, the characteristic of "bad metals". Compared to elemental metals, it has a lower carrier density and an effective mass four times higher than a free electron [18, 19]. These features give rise to a low reflectivity in the visible due to its low plasma frequency [20] and a substantial absorption coefficient. These features make $SrRuO_3$ a reasonable entry point for studying acoustic phonon dynamics in perovskite oxides, especially since it can be integrated into heterostructures with many other materials.

4.2.1. Sample preparation

The films were deposited on a $SrTiO_3$ substrate by pulsed laser deposition using a 248 nm KrF excimer laser at a 1 Hz repetition rate ablating a sintered powder of $SrRuO_3$ at a fluence of 1.2 J/cm^2. The substrate was heated to about 600 °C during this process, and the partial pressure of oxygen in the growth chamber was 10 Pa.

Next, we prepared another sample containing an intermediate layer of SAO grown below the $SrRuO_3$ film at a substrate temperature of 850 °C and a low oxygen partial pressure of 10^{-4} Pa. Consequently, the $SrRuO_3$ film was released from the substrate by dissolving the SAO layer in water and transferred to a substrate of CaF_2. For the latter sample, an x-ray diffractogram around the [0 0 2] condition of the substrate was measured before and after the film transfer, shown in figure 4.2a. The presence of a Bragg peak before and after the transfer confirms the integrity of the crystal after the transfer process. We also measured the resistivity of the transferred film as a function of temperature, shown in figure 4.2b, confirming that the membrane remains metallic and even exhibits the characteristic kink in the resistivity at the magnetic transition temperature $T_N = 131$ K.

4.2.2. Time-resolved reflectometry

The sample was excited with pump pulses of central wavelength $\lambda_p = 640$ nm ($\hbar\omega_p = 1.94$ eV), with a pulse duration of about 100 fs, a repetition rate of 500 Hz, and a fluence of 0.5 mJ/cm^2. These pulses were generated using a sequence of nonlinear processes: An optical parametric amplifier seeded by a titanium-sapphire (Ti:S) laser was used to create pulses of 1.28 µm wavelength; second-harmonic generation of these in barium borate produced the final wavelength at 640 nm.

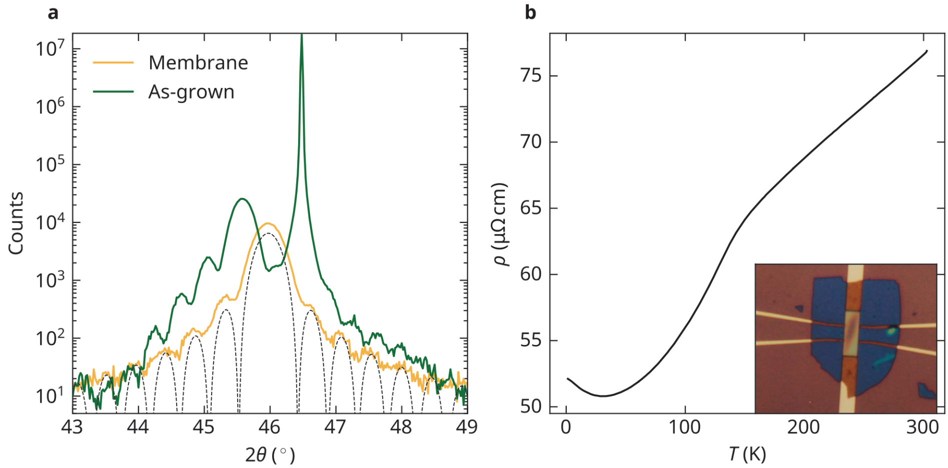

Figure 4.2: **Characterisation of freestanding membranes** **a**. X-ray diffractogram at various stages of the sample: as-grown on $SrTiO_3$ with an intermediate water-soluble film ($Sr_3Al_2O_6$) (green), and after release and supported on CaF_2 (yellow). A simulated diffractogram is shown in a dashed line, with c-axis lattice constant of 3.945 Å, and thickness of 54 unit cells. The finite-size oscillations and the clear central peak indicate good crystal coherence of the released membrane. **b**. Longitudinal resistivity ρ of a single $SrRuO_3$ membrane, measured using a Hall bar of dimension $3 \times 9\,\mu$m.

A weak 1 kHz pulse train of 800 nm (1.5 eV) light from the Ti:S laser was used as probe. The probe beam was focused to a spot size of about 100 µm on the sample. The reflected intensity was measured using a pair of balanced photodiodes, whose voltage difference was demodulated at 500 Hz with a lock-in amplifier. This amounts to a measurement of the difference in reflected power from the photoexcited sample and the sample at equilibrium. An automated moving retroreflector controlled the relative arrival of the pump and probe pulses at the sample. Both pump and probe energies lie above the plasma energy of the electron gas (0.62 eV [21]). The pump energy lies between the $t_{2g} \longrightarrow t_{2g}$ (or 4d) transitions of Ru and $O_{2p} \longrightarrow t_{2g}$ charge-transfer transitions [22], driving a mixture of these. The probe mainly measures the electronic state of a Ru-t_{2g} band near the Brillouin zone center, as $\hbar\omega_{\mathrm{pr}}$ is close to a $t_{2g} \longrightarrow t_{2g}$ transition [22].

4.2.3. Comparing membrane and film

The measured signals are summarized in figure 4.3, including fits to the following minimal model:

$$\frac{\Delta R}{R} = \Theta(t)\left(a_{\mathrm{th}} e^{-t/\tau_{\mathrm{th}}} + a_{\mathrm{osc}} \cos(2\pi f t + \phi) e^{-t/\tau_{\mathrm{osc}}}\right) \tag{4.12}$$

Here, Θ is a step function with a step rate corresponding to the pulse duration. Two distinct oscillation frequencies are present in the reflectivity: For the thin film on $SrTiO_3$, the oscillation frequency is $f_{\mathrm{film}} = 45\,\mathrm{GHz}$; for the freestanding membrane on CaF_2, the oscillation frequency is $f_{\mathrm{m}} = 130\,\mathrm{GHz}$. To understand their different origins, consider the relationship between the reflection coefficient and the strain in the sample, as derived by Matsuda et al. [23],

$$\frac{\Delta r(t)}{r_0} = \frac{2ik\hat{n}}{1-\hat{n}^2}\int_0^\infty \mathrm{d}z\,\epsilon(z,t)\frac{\partial\hat{n}(t)}{\partial\epsilon}e^{2ik\hat{n}z} \tag{4.13}$$

where the photoelastic constant $\partial\hat{n}/\partial\epsilon$ relates the strain $\epsilon(z,t)$ to the complex refractive index $\hat{n}$. This tensor is not available in the literature for $SrRuO_3$. Without it, estimating ϵ from the reflectivity data is difficult. Note that we are measuring reflected intensity, not the amplitude, so that our observable is $\Delta R/R_0 \approx \mathrm{Re}(2\Delta r/r_0)$.

Origin of slow oscillations

Assuming the acoustic reflectivity of the interface is small, we know that phonons generated in the film transmit into the substrate—they have nowhere else to go. Elastic continuity across the interface means phonons of any wavelength can be generated. However, only the film absorbs the light, so phonons are only generated in a region of thickness d. The excitation profile is a rectangle function $\Pi(z/d)$, zero everywhere but for $|z/d| < 1$. The reciprocal space image of this profile (*viz.* the Fourier transform $\mathcal{F}$) is

$$\mathcal{F}\left[\Pi(z)\right] = \frac{\sin(\pi q d)}{\pi q} \tag{4.14}$$

The confinement causes acoustic diffraction, producing a *wavepacket* with most of its density within $q < 1/d$:

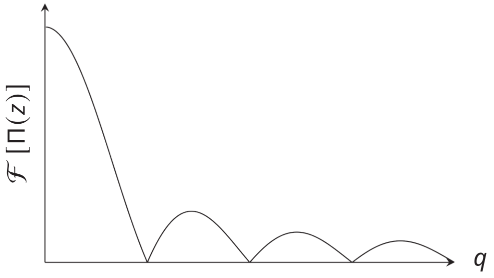

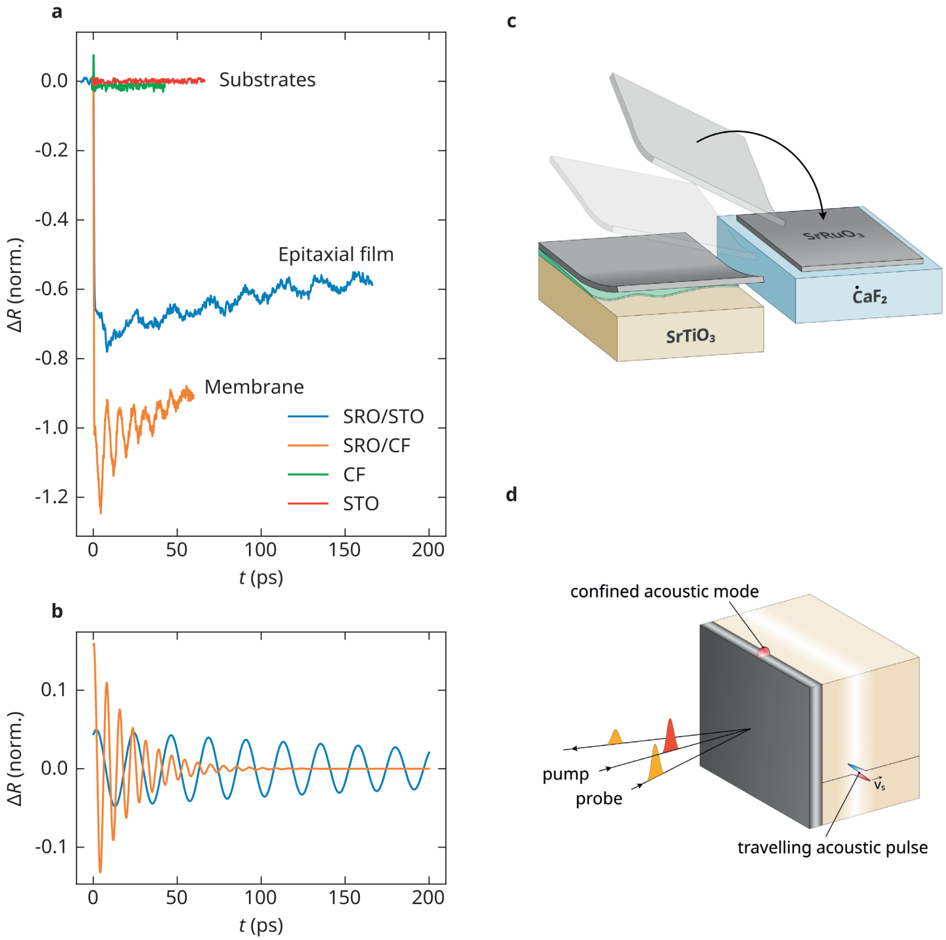

Figure 4.3: **Acoustic confinement in freestanding membranes** **a**. Comparison of reflectivity (transmittivity) dynamics of a photoexcited $SrRuO_3$ film and freestanding membrane, on $SrTiO_3$ (STO) and CaF_2 (CF) substrates. **b**. Extracted oscillations based on fits to equation (4.12). **c**. Illustration of the epitaxial release process: The $SrRuO_3$ film is grown on a water-soluble crystalline buffer layer deposited on an STO substrate. This buffer layer dissolves in water, releasing the $SrRuO_3$ film and leaving it on a transfer tape. The tape is then attached to a CF substrate and removed, leaving a density of $SrRuO_3$ membranes on the CF substrate. **d**. Illustration of two optoacoustic effects, the confined acoustic mode involving a local oscillation of the film/membrane thickness and the traveling acoustic pulse emitted into the substrate.

How would this wavepacket manifest in the time domain reflectivity? We consider the $d \longrightarrow 0$ limit and let the wavepacket propagate into the substrate at the speed of sound v_s. Then $\Delta\hat{n}(t) \sim \delta(z - v_s t)$, in which case equation (4.13) implies that the signal will go as

$$\Delta r/r_0 \sim e^{2ik\hat{n}v_s t} \tag{4.15}$$

The oscillation frequency is set by the probing wavenumber k and the speed of sound v_s. Specifically,

$$f = knv_s/\pi \tag{4.16}$$

with n the real part of the refractive index. With the wavelength $\lambda = 800\,\text{nm}$ of our probe, and a refractive index of $n = 2.34$ for $SrTiO_3$, we get $f = (5.86 \times 10^6\,\text{nm}^{-1})v_s$. Equating this with the observed frequency for the thin film, $f_{\text{film}} = 45\,\text{GHz}$, we get $v_s = 7.7\,\text{nm/ps}$. This is close to another measured value of the longitudinal speed of sound in $SrTiO_3$ of 7.9 nm/ps [24]. We conclude that the slower signal f_{film} arises from an acoustic wavepacket traveling into the substrate, produced by phonon emission from the film.

Origin of fast oscillations

Considering the limiting case of an isolated membrane, it must support acoustic standing waves in the confinement direction. The fundamental mode of such a longitudinal wave, the fundamental dilatational mode, will have a wavenumber $q_0 = \pi/d$ [25]. Using the linear dispersion relation, the corresponding frequency is[1]

$$f_0 = v_s q_0/2\pi = \frac{v_s}{2d} \tag{4.17}$$

Considering a localized acoustic phonon oscillating at f_0 in an infinitesimally thin region at $z = d$. Then we can take $\Delta\hat{n} \propto \delta(z - d)\cos(2\pi f_0 t)$ and the signal goes as

$$\Delta r/r_0 \sim \cos(2\pi f_0 t) \tag{4.18}$$

The measured oscillation frequency coincides with that of the acoustic phonon and is independent of the probing wavenumber. To see whether this matches the experimental data, we evaluate f_0 for $d = 21.3\,\text{nm}$, and the bulk value for the longitudinal group velocity for $SrRuO_3$, $v_s = 6.31\,\text{nm/ps}$ [26]. This gives $f = 134\,\text{GHz}$, very close to the observed

---

[1] This generalizes to the case of a supported membrane but requires that the impedance is greatest in the membrane. If the substrate has the greater acoustic impedance, the frequencies will be halved [25].

frequency $f_\mathrm{m} = 130\,\mathrm{GHz}$. We conclude that the faster signal (f_m) arises from the fundamental dilatational mode of the membrane. In summary, we identified two distinct acoustic effects in the samples: In the epitaxial film, the $SrRuO_3$ acts as a photoacoustic transducer. The stresses produced by the optical excitation in the thin film are transmitted into the substrate and produce a coherent acoustic wavepacket traveling into the substrate at the speed of sound. The transferred film, which rests non-epitaxially atop CaF_2, supports a confined acoustic mode, and the reflectivity oscillations arise from the vibrations in the membrane. The two effects are illustrated in figure 4.3c.

4.2.4. Phonon excitation mechanism

According to the point estimates awarded by fitting the data to equation (4.12), we find that the phonon phase is $\phi \approx 0$ (see figure 4.3). In other words, the oscillations are cosinusoidal, consistent with a *displacive* (stepped) excitation mechanism, rather than an impulsive one (see section 4.1.2).

In search of a displacive source, let us start by assuming that the stress dynamics can be modeled thermodynamically: After photoexcitation, the electrons instantly form a thermal (Fermi-Dirac) distribution with a corresponding elevated temperature T_e, while the thermal (Bose-Einstein) distribution of the phonons remains unchanged. Then the two subsystems (T_e, T_p) will thermalize on a timescale set by the rate of electron-phonon collisions ($\tau_\text{e-p}$), and at all times the two subsystems remain at equilibrium internally. These are the assumptions of the “two-temperature model” [27]. The corresponding stresses are thermoelastic, following the subsystem (i) temperatures as $\sigma_i = \gamma_i C_i \Delta T_i$, with C_i the volumetric specific heat.[2]

There are at least two ways in which a displacive force can originate. Let f_0 be the phonon frequency, and consider two limiting cases:

1. $f_0\tau_\text{e-p} < 1$: T_e decays quickly, transferring energy to the phonons, which produces a displacive stress $\sigma_p \approx -\gamma_p C_p \Delta T_p$.
2. $f_0\tau_\text{e-p} > 1$: T_e will decay slowly, and will itself be a step function on the phonon timescale, producing a displacive stress $\sigma_e \approx -\gamma_e C_e \Delta T_e$.

---

[2] Note that the phonons excited by the decaying electrons have no phase relation with each other and are not themselves contributing to the coherent acoustic phonon state. Rather, the coherent phonon is excited by the transient stress exerted by the hot lattice.

To assess which source dominates, we must consider the dynamical equations explicitly.

Two-temperature model

Neglecting electron diffusion—since we are dealing with a thin film and a homogeneous excitation—as well as the thermalization with the substrate that happens on a longer timescale, the two-temperature model is a simple pair of coupled ODEs,

$$C_e(T_e)\frac{\mathrm{d}T_e}{\mathrm{d}t} = P(t) - G(T_e - T_l) \tag{4.19}$$

$$C_p\frac{\mathrm{d}T_l}{\mathrm{d}t} = G(T_e - T_l) \tag{4.20}$$

We approximate C_p to be constant for the phonons at ambient conditions [28]. The electronic specific heat is linear in temperature, $C_e(T_e) = aT_e$, with a the electronic specific heat coefficient. The constant G is proportional to the electron-phonon coupling strength [29, 30], and $\tau_{\text{e-p}} \approx C_e(T_0)/G$. It is approximately independent of temperature. The source term $P(t)$ is given by

$$P(t) = \frac{\overline{P}A}{f_{\text{rep}}\tau_p(\pi w^2/2)d}\frac{e^{-t^2/2\sigma^2}}{\sigma\sqrt{2\pi}}, \qquad A = \frac{8dk_0\kappa n}{(1+n_s+2dk_0\kappa n)^2} \tag{4.21}$$

The parameters in these equations are explained in table 4.1, and the solution to the system of equations (4.20) is shown in figure 4.4. Inspecting the solution, we see that with the electron-phonon coupling G reported in the literature [32], the electron temperature falls at a rate *much* slower than the phonon period $1/f_0$. That seems to suggest we are in the $f_0\tau_{\text{e}-\text{p}} \gg 1$ regime 2, i.e., that the electron temperature itself is a displacive force, and that thermal phonons are not involved in the excitation process. The slow decay time observed in the reflectivity data also supports regime 2. In section S1.2, we argue that for the non-oscillatory reflectivity dynamics, $R \propto T_e$.

Hot electron pressure

To assess whether hot electron pressure explains the excitation of the coherent acoustic phonon, we compare the electronic stress with that obtained after the equilibration of electron and phonon temperatures. The stress produced at the highest electron temperature T_e^* is

$$\sigma_e = -\gamma_e a T_e^*(T_e^* - T_0) = -(20\,\mathrm{MPa})\gamma_e \tag{4.22}$$

Parameter	Value	Description
$\overline{P}$	2 mW	Average power of pulse train
n	1.962 [31]	Refractive index at 640 nm
κ	0.964 [31]	Extinction coefficient at 640 nm
f_{rep}	1 kHz	Pulse rate
τ_p	150 fs	Pulse duration
w	2.3 mm	Beam radius
d	21.7 nm	Film thickness
a	800 Pa/K^2 [32]	Electronic specific heat coeff.
C_p	2.85 MPa/K [26]	Phonon specific heat
G	2 kPa/K/ps [32]	e-p coupling constant

Table 4.1: Parameters used in the solution to the 2T model, shown in figure 4.4.

We do not know the electron Grüneisen parameter γ_e. According to the Sommerfeld model, $\gamma_e = 2/3$, but in multiband systems, it is typically somewhat greater than unity. Let us compare this to the stress after thermalization when the total temperature is $T^* = 310$ K:

$$\sigma = \sigma_e + \sigma_p = -(2.4\,\text{MPa})\gamma_e - (28.5\,\text{MPa})\gamma_p \tag{4.23}$$

The initial hot electron pressure immediately after excitation is comparable to the total stress after equilibration, indicating that the hot electrons explain the excitation of the acoustic mode. On the other hand, we see from figure 4.5 that the amplitude of the phonon scales linearly with the pump pulse energy E_{ex}. The resulting stress is *quadratic* in the electron temperature, so we expect $\sigma_e \sim E_{\text{ex}}^2$. In figure 4.5, we show how the reflectivity dynamics scale with the energy of the pump pulse. According to figure 4.5b, the thermal background a_{th} scales linearly with the pump energy, as expected if the reflectivity is proportional to the electron temperature T_e. However, looking at figure 4.5d, the amplitude of the oscillations a_{osc}, which we assume to be proportional to the stress, also scales linearly with the pump energy. That is in contradiction with the quadratic relation expected from hot electron pressure.

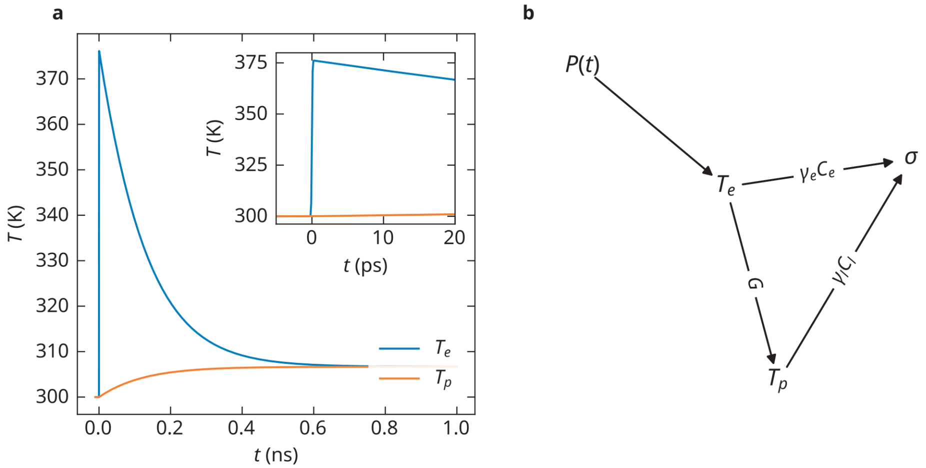

Figure 4.4: **Two-temperature model** **a**. The solution to the two-temperature model of Eq. (4.20). Due to the small value of G, the electron temperature is retained at a high value during the lifetime of the acoustic oscillations, and the phonon temperature does not contribute at this timescale (see inset for a close-up on the short timescale). **b**. Directed graph illustrating the energy flow within the two-temperature model toward the production of stress.

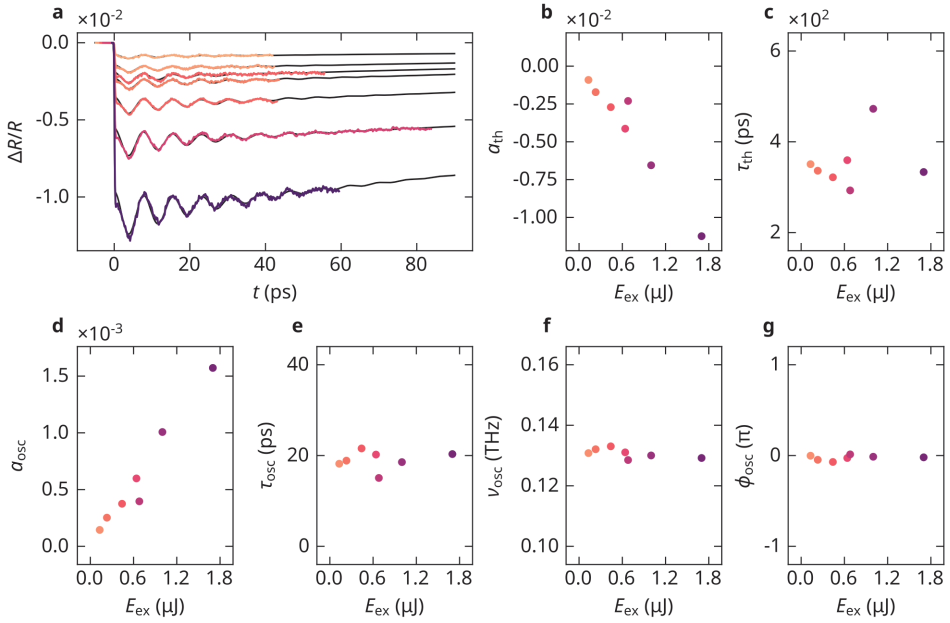

Figure 4.5: **Reflectivity dynamics** Pump pulse energy E_{ex} dependence of oscillatory (*osc*) and non-oscillatory or thermal (*th*) dynamics. Parameters are point estimates from fits to equation (4.12).

Strong electron-phonon coupling

There is compelling evidence of a non-thermal source of light-induced stress in $SrRuO_3$. In an earlier work by Wei et al. [33], the Raman phonon spectrum of $SrRuO_3$ was measured under continuous laser illumination. At a laser intensity of $50\,W/cm^2$, they observed phonon frequency shifts that correspond to a lattice strain of $0.76\,\%$. This strain was present despite negligible laser-induced heating, as measured by the relative intensity of Stokes and anti-Stokes scattering.

Photoemission measurements of the electronic spectrum of $SrRuO_3$ reveal a significant kink in the quasiparticle band dispersion at an energy of $\hbar\Omega = 65\,meV$ [18]. Such a kink implies that the quasiparticle scattering rate is modified within a narrow energy range, signifying strong coupling between the electrons and a collective excitation [34]. Yang et al. [35] identified the collective mode as a bond-stretching optical phonon. In other words, the electrons in $SrRuO_3$ are intrinsically dressed by a specific phonon mode, an effect so significant as to increase the electron mass by a factor of 4 [18]. Enhanced coupling to a single optical phonon means that the two-temperature model is not valid; one cannot average over the phonon sector and assume a single phonon temperature T_p and coupling constant G [27]. Sometimes, a *three* temperature model is used, treating the more strongly coupled phonon apart from the rest of the phonon sector, with its separate temperature [27]. In a weak coupling regime, this phonon provides a faster electron relaxation channel. This process would restore the rapid decay of the electron temperature, which we did not observe in our experiments. In the strong coupling regime, which is believed to be the case for $SrRuO_3$ [18], the strongly coupled phonon will be excited not by electron *decay*, with no phase relation among each other, but rather concomitantly with the electron transition. That translates to stress either according to equation (4.2), with the phonon distribution being strongly non-thermal, or else through its intrinsic anharmonicity, $V_{\mathrm{anh}} \sim Q_\Omega^2 \epsilon$ [11].

4.3. Thermal annealing

Having shown that the freestanding membrane supports a confined acoustic phonon, we now consider whether the epitaxial interface between the membrane and the substrate can be restored by promoting the formation of chemical bonds at high temperatures. We fabricate a new sample of $SrRuO_3$ membranes but transfer them to an $SrTiO_3$ substrate equivalent to the one on which they were grown. The acoustic properties are measured after annealing at increasingly high temperatures, cooling the sample back to room temperature for each measurement.

4.3.1. Sample preparation and characterization

This sample was grown using a combination of pulsed laser deposition for the sacrificial layer, followed by sputtering of the $SrRuO_3$ layer to a thickness of about 40 nm. The sample was then annealed in a furnace at progressively higher temperatures for about 1 h, each time cooling it back down and measuring the reflectivity dynamics. X-ray characterization of the sample after each annealing step is shown in figure 4.6, demonstrating crystallinity of the membranes up to 550 °C, and a reduction after annealing at 750 °C. Optical and atomic force microscopy of the sample after exposure to 750 °C showed the appearance of large (on the scale of 100 nm) nanoparticles on the sample surface, as well as a marked change in the opacity and morphology of the sample, indicating a change in the sample stoichiometry and crystallinity. As such, we consider only the annealing steps up to 550 °C henceforth.

4.3.2. High-throughput reflectometry

The transfer process leaves not a continuous film but a surface covered with distinct pieces of $SrRuO_3$. Since thermal annealing is a thermodynamic process, it is conceivable that the acoustic properties of some pieces will change while others will not. We measure many pieces in sequence for each annealing step to avoid missing these statistics. That requires the use of a fast experimental setup. We used an asynchronous optical sampling (ASOPS) scheme to allow high-speed scanning over a nanosecond range with picosecond resolution without using a mechanical delay line. This technique uses two synchronized lasers emitting 100 MHz pulse trains with a small (kHz) offset in their repetition rate. The entire train of current pulses produced by the probe pulses on a photodiode is recorded with a high-speed acquisition card, and the envelope of this train corresponds to the transient dynamics. The probe central wavelength is 780 nm, with an average power of about 100 µW. The pump was 1560 nm, with an average power of about 100 mW.

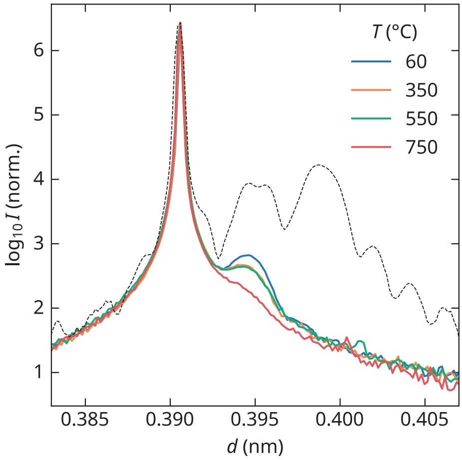

Figure 4.6: **X-ray diffractometry** X-ray diffractogram of the sample at various stages of its history. Each color corresponds to exposure to a different annealing temperature T. The black line corresponds to the diffractogram of the film grown atop the sacrificial layer. The 2θ range corresponds to a measurement around the [0 0 2] Bragg condition and the main sharp peak is that of the $SrTiO_3$ substrate. The data has been normalized to the intensity of this peak. The presence of the $SrRuO_3$ peak (indicated at the dotted vertical line) signifies the crystallinity of the membrane. The intensity signals the crystalline coherence but is also affected by the placement of the sample in the diffractometer because of the inhomogeneous coverage of the substrate surface with $SrRuO_3$.

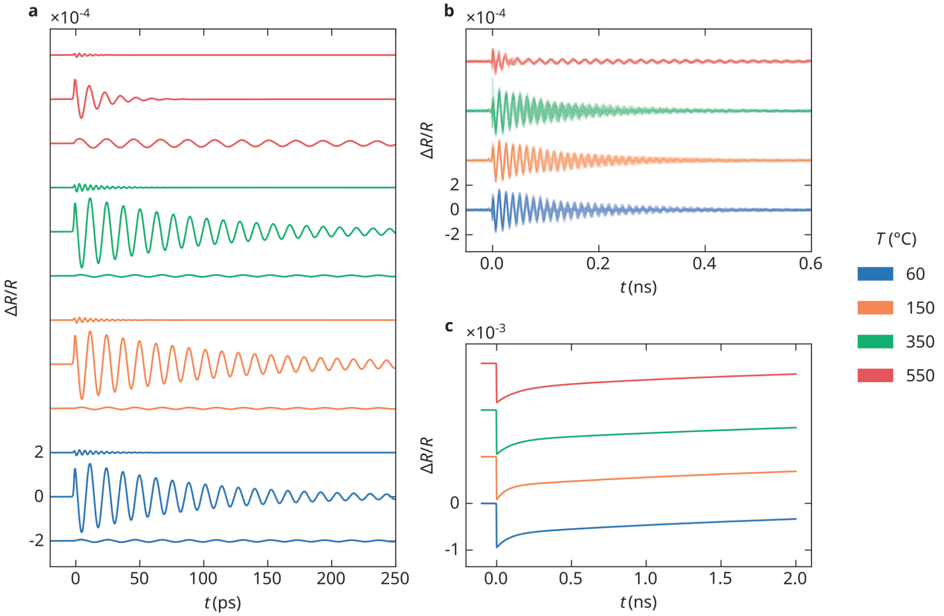

Figure 4.7: **Reflectivity dynamics of annealed samples** Annealing temperature (T) study of phonon dynamics. **a**. Oscillatory components to the least-squares solution, offset for visibility. The slowest frequency f_B is the Brillouin oscillation, the intermediate frequency f_m is the dilatational mode of the membrane, and the fastest signal $3f_m$ is the third harmonic of that membrane mode. **b**. Raw signal, with the background subtracted. **c**. The biexponential background component of the least-squares solution.

4.3.3. Results

The results of these measurements are shown in figure 4.7, where the data was fit to the following model:

$$\frac{\Delta R}{R} = \Theta(t) \left(\sum_{i=1}^{2} a_i^{\mathrm{th}} e^{-t/\tau_i^{\mathrm{th}}} + \sum_{i=1}^{3} a_i^{\mathrm{osc}} e^{-t/\tau_i^{\mathrm{osc}}} \cos(2\pi f_i t + \phi_i) \right) \tag{4.24}$$

This model is more involved than that of equation (4.12), including Brillouin oscillations (from the phonon wavepacket traveling into the substrate), the next allowed[3] order of the dilatational mode of the membrane (oscillating at $3f_\mathrm{m}$), and a biexponential thermal signal.

The point estimates for parameters of the three oscillators obtained from these fits are shown in figure 4.8, including the distribution of the parameters over the sequence of measurements taken randomly across the sample surface. While the thermal background does not have any stark dependence on annealing temperature, there is a significant disruption at 550 °C occurring for the oscillatory components: the amplitude of the Brillouin oscillations, shown in figure 4.8a, has increased, while the amplitude and lifetime of the fundamental vibration, shown in figure 4.8 (e, g), decreased by a factor 1.5 and 5.6, respectively.

4.3.4. Discussion

The drop in the lifetime of the confined phonon, combined with the increase in the Brillouin oscillations, points to enhanced elastic coupling of the membrane to the supporting substrate: the emission of phonons into the substrate increases the amplitude of the traveling waves while lowering both the amplitude and the lifetime of the membrane modes. This enhanced elastic coupling cannot be due to the evaporation of water molecules from the interface, which would manifest already at 150 °C. We can treat the membrane confinement as a consequence of a soft interface between the membrane and the substrate, parametrized by a finite stiffness k. In the $k \longrightarrow \infty$ limit, which corresponds to an epitaxial interface with perfect atomic connectivity, the reflectivity of the interface is a function of the acoustic impedances $z_i = \rho_i v_{s,i}$ is the mass density and $v_{s,i}$ is the speed

---

[3] Only centrosymmetric strain profiles are detectable, according to equation (4.13)

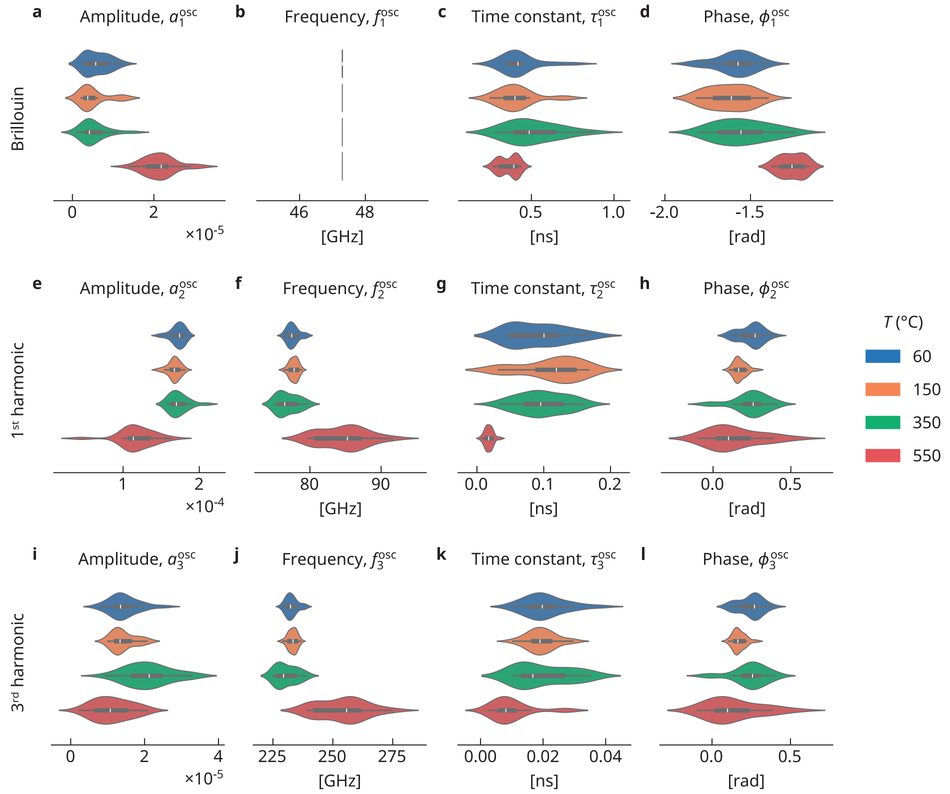

Figure 4.8: **Statistical distributions of oscillator parameters** Distribution, based on twenty measurements across the sample surface, of the point estimates for the oscillator parameters from a least-squares fit of equation (4.24) to the reflectivity data in figure 4.7. Color denotes annealing temperature T. **a-d**. Brillouin oscillations. **e-h**. Fundamental dilatational mode of the membrane. **i-l**. Third harmonic of the membrane mode.

of sound (i = **m**embrane, **s**ubstrate), where ρ_i:

$$r_0 = \frac{z_s - z_m}{z_s + z_m} \tag{4.25}$$

For finite k, the reflectivity is modified by the loss of energy into the substrate [36],

$$r = \frac{z_s - z_m - i z_s z_m \omega/k}{z_s + z_m + i z_s z_m \omega/k} = \frac{r_0 - i z_s z_m \omega/k}{1 + i z_s z_m \omega/k} \tag{4.26}$$

The lifetime of the membrane mode, if we assume the only loss channel is emission into the substrate, can be shown to be [37]

$$\tau = -\frac{1}{f_m \ln |r|} \tag{4.27}$$

The limiting value ($r = r_0$) of the decay time is $\tau = 2.5$ ps, using the values for density and sound velocity from table 4.2. Experimentally, we find that for temperatures $T < 550\,^\circ$C, the acoustic lifetime is $\tau = 100$ ps on average (see figure 4.8). After annealing at $550\,^\circ$C, this lifetime drops to $\tau = 18$ ps. Calculating k from equation (4.27), this means the spring constant starts at the low value of $k = 5.3\,\mathrm{nN/nm^3}$ and rises to a value $k = 30\,\mathrm{nN/nm^3}$ after the high temperature anneal.

Table 4.2: Acoustic impedance for the membrane and substrate.

Material	Acoustic impedance (ρv_s)
$SrTiO_3$ (s)	$5.11\,\mathrm{g/cm^3} \times 7.9\,\mathrm{nm/ps} = 40.36\,\mathrm{sPa/\mu m}$
$SrRuO_3$ (m)	$6.46\,\mathrm{g/cm^3} \times 6.31\,\mathrm{nm/ps} = 40.76\,\mathrm{sPa/\mu m}$

Assuming a Lennard-Jones potential as a model for the interfacial displacements, the spring constant (in the harmonic approximation) can be expressed in terms of the equilibrium distance $2^{1/6}\delta$ as $k = 72\varepsilon/\delta^2$, where ε is the bonding energy. That allows us to estimate the change in the average distance between the $SrRuO_3$ membrane and the substrate before (δ_0) and after (δ) annealing:

$$\delta = \delta_0 \sqrt{\frac{k_0}{k}} = \frac{\delta_0}{2.4} \tag{4.28}$$

In other words, the average membrane-substrate distance was reduced by a factor of 2.4. The moderately high temperature of $550\,^\circ$C is close to the growth temperature of $SrRuO_3$

in pulsed laser deposition. During deposition, diffusion of adatoms around the surface is part of the two-dimensional growth process. The diffusivity D of the adatoms in $SrRuO_3$ is known to be relatively low compared to most complex oxides [38]. Therefore, it is plausible that atomic diffusion occurs at the substrate-membrane interface during annealing. Since diffusion flux J is driven by gradients of the density ρ, that is, $\mathbf{J} = -D\nabla\rho$, this will tend to fill microscopic voids at the interface, reducing the average membrane-substrate distance. This process is sometimes used to fuse two materials without reaching their melting point and is known as cold welding or diffusion bonding. The process is illustrated in figure 4.9. Beyond this microstructural effect, we also expect chemical bonding to occur. In a recent work by Lee et al. [39], $SrRuO_3$ membranes were placed on micropores, and they could measure diffusion rates of N_2 gas in and out of the pore. They found that moderate thermal annealing (300 °C) resulted in a reduction of the diffusion rate by five orders of magnitude. That is consistent with our observations and the interpretation of a reduction in the average substrate-membrane distance. The authors did not observe a significant change in diffusion rates for an $SrRuO_3$ membrane placed on a micropore in a Si_3N_4 substrate, suggesting that the effect is chemically selective. Chemical reactions at surfaces are prevalent due to dangling bonds, metastable termination, and defects.

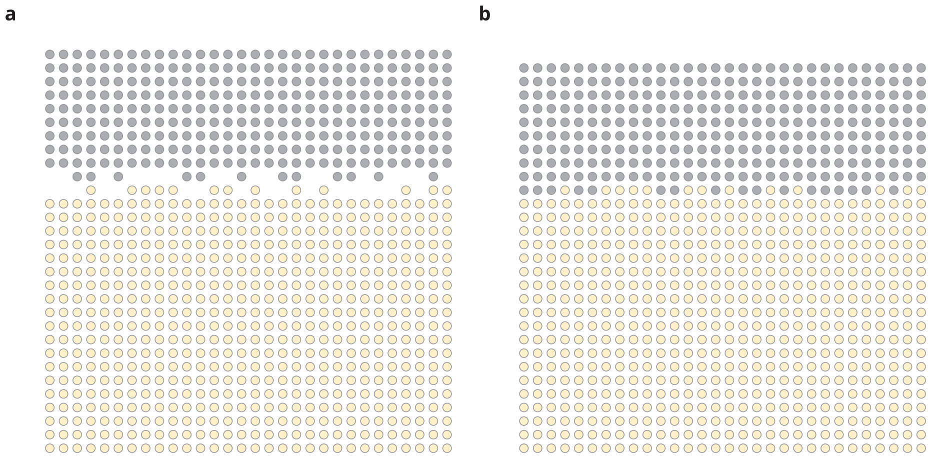

Figure 4.9: Illustration of diffusion bonding, driven by the tendency for random ionic movement to fill micro- and nanoscopic voids at the interface. **a**. Before annealing. **b**. After annealing.

It is known that Ru and RuO_2 are redox active and thermally unstable, and that $SrRuO_3$ can be formed by the hot reaction of SrO and RuO_2 interfaces in an oxygen atmosphere [40], according to

$$\mathrm{SrO} + \mathrm{RuO_2} \longrightarrow \mathrm{SrRuO_3} \tag{4.29}$$

The $SrTiO_3$ substrate used in this study did not have a unique termination but had a mixed SrO and TiO_2 termination. We therefore expect that the considerable improvement in the elastic coupling also involves the formation of chemical bonds at the interface.

We encourage further study on the annealing of freestanding oxide membranes, with careful control of the substrate termination, membrane alignment, and chemical substitution. Advancements may enable the fabrication of a new class of complex oxide heterostructures formed by the fusion of freestanding membranes.

4.4. Outlook

In a study by Wang et al. [41] on an epitaxial film of $SrRuO_3$ grown atop $SrTiO_3$, ultrafast reflectivity dynamics were studied using time-resolved x-ray diffraction. They found that the *c*-axis dilatation was linear in the pump (2.38 eV) fluence at least up to 2.5 $\mathrm{mJ/cm^2}$. Moreover, the dilatation at the maximum fluence, at the pump-probe overlap time, was $\epsilon = 0.08\,\%$. That strains on the order of 1 % are possible in the thin film geometry, with no sign of saturation, is greatly encouraging. Considering the enhanced amplitude and lifetime of this dynamical strain afforded by the membrane geometry explored in this work, this opens up the possibility of studying the effects of dynamical strains at sub-terahertz rates and amplitudes comparable to those of lattice mismatch engineering—traversing significant distances in the phase space of many complex oxides, dynamically. That is an opportunity not present in the thin film geometry, where the dynamical strain is limited by the lifetime ($\sim$ 1 ps) afforded by the small acoustic impedance mismatch.

4.5. Contributions

M. Matthiesen performed the optical experiments, the data analysis, and the sample annealing process. The growth and transport measurements for Figure 4.2 were done by E. Lesne and M. Lee, while the samples for the annealing study were grown by G. Kimbell and L. Tovaglieri, and studied with temperature dependent x-ray diffractometry by the former. Diffractometry on the samples studied with ASOPS was done by P. Blah and U. Filippozzi. The ASOPS setup was built by R. Guis, while the pump-probe reflectometry setup was built by M. Matthiesen.

4.6. Data availability

The data recorded in the experiments of this chapter, and the code used for the analysis and calculations are accessible at the DOI 10.5281/zenodo.13220717.

S1. Supplemental material

S1.1. Temperature-dependent x-ray study

To verify the crystallinity of the membranes even at high temperatures, we measured the [0 0 2] Bragg peak of the substrate and the membrane as a function of temperature. These membranes were grown with pulsed laser deposition, rather than sputtering as in the data of Figure 4.7 and Figure 4.6. We find a that the out-of-plane pseudocubic lattice constant is $c = 0.396\,\mathrm{nm}$, larger than the single crystal bulk value of $c = 0.393\,\mathrm{nm}$. That is likely due to growth conditions away from the optimum, and the presence of ruthenium vacancies which tend to enlarge the unit cell volume [42]. Figure S1a shows a scan around the [0 0 2] peak of the substrate, with the membrane peak on its shoulder. In Figure S1b the center position of the two peaks is shown as a function of temperature. Initially, a thermal expansion occurs at nearly the same rate for both substrate and membrane, until the membrane c-axis starts to shrink toward its native bulk value, likely due to a change in the film stoichiometry related to the defect-rich crystal.

S1.2. Temperature-reflectivity correspondence

The reflectivity is a temperature-dependent quantity since temperature is related to the electronic distributions. We are predominantly probing a Ru-t_{2g} band and expect to be sensitive to its occupation, specifically. Therefore, we expect $R = R(T_e)$. We can then use thermoreflectance measurements (in which $T_e, T_p = T$) to model $R(T_e)$. Reference [31] provides this data, where at the probing wavelength $\lambda = 800\,\mathrm{nm}$, they measure

$$\frac{\partial n}{\partial T} = -2.9 \times 10^{-4}\,\mathrm{K}^{-1}, \qquad \frac{\partial \kappa}{\partial T} = -8.1 \times 10^{-4}\,\mathrm{K}^{-1} \tag{4.30}$$

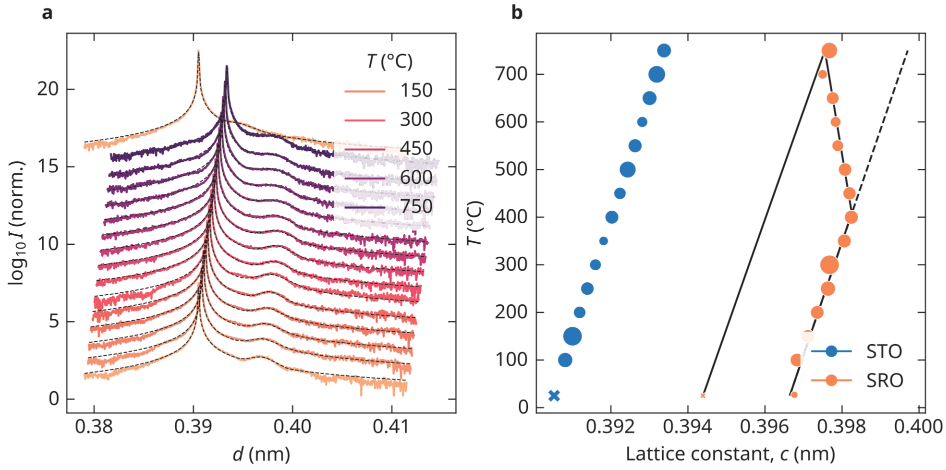

Figure S1: **a**. X-ray diffractogram around the [0 0 2]-peak of the substrate, $SrTiO_3$. The x-axis has been converted to distance, at the Bragg condition, which corresponds to the c-axis lattice parameter. Dotted lines are best-fit lines to two pseudo-Voigt peaks. **b**. Lattice constant from fits, as a function of temperature. The point size denotes the peak intensity (max-normalized for each peak, separately).

To relate this to the reflectivity, consider the Fresnel expression for the reflectivity of a thin film with an index of refraction $\hat{n} = n + i\kappa$ atop a transparent substrate of index n_s:

$$R = \left| \frac{r_{12} + r_{23} e^{2i\hat{k}d}}{1 + r_{12} r_{23} e^{2i\hat{k}d}} \right|^2 \approx \frac{(1 - n_s - 2dk_0\kappa n)^2}{(1 + n_s + 2dk_0\kappa n)^2} \tag{4.31}$$

where r_{ij} is the reflection coefficient at the interface between media i and j and the complex wavenumber in the film is $\hat{k} = k_0\hat{n}$. The last equality is the thin film approximation, $k_0 nd \ll 1$ [43]. Suppose the temperature jumps by ΔT. Then the reflectivity changes by

$$\frac{\Delta R}{R} = \frac{1}{R} \left(\frac{\partial R}{\partial n} \frac{\partial n}{\partial T} + \frac{\partial R}{\partial \kappa} \frac{\partial \kappa}{\partial T} \right) \Delta T = \frac{8k_0 d}{(2\kappa k_0 nd + n_s)^2 - 1} \left(\kappa \frac{\partial n}{\partial T} + n \frac{\partial \kappa}{\partial T} \right) \Delta T \tag{4.32}$$

The relative reflectivity therefore has the following proportionality to the temperature jump:

$$\frac{\Delta R}{R} = -1.8 \times 10^{-4}\,\mathrm{K}^{-1} \Delta T \tag{4.33}$$

At the greatest pump fluence in Figure 4.5, we observe a relative jump of $\Delta R/R = -10^{-2}$ (see Fig. 4.5), which would correspond to a thermal jump of about $\Delta T = 55\,\mathrm{K}$. This is similar to the 70 K jump observed in the calculations (see Fig. 4.4). It therefore seems reasonable to infer the evolution of $T_e(t)$ from the evolution of $\Delta R(t)/R$, keeping in mind that there will necessarily be non-thermal (photoelastic) contributions to the reflectivity as well—otherwise, no oscillations would be present.

References

1. Disa, A. S. *et al.* Polarizing an Antiferromagnet by Optical Engineering of the Crystal Field. *Nature Physics* **16** (2020).
2. Afanasiev, D. *et al.* Ultrafast Control of Magnetic Interactions via Light-Driven Phonons. *Nature Materials* **20** (2021).
3. Rini, M. *et al.* Control of the Electronic Phase of a Manganite by Mode-Selective Vibrational Excitation. *Nature* **449** (Sept. 2007).
4. Caviglia, A. D. *et al.* Ultrafast Strain Engineering in Complex Oxide Heterostructures. *Physical Review Letters* **108** (Mar. 26, 2012).
5. Rowe, E. *et al.* Resonant Enhancement of Photo-Induced Superconductivity in K_3C_{60}. *Nature Physics* **19** (Dec. 2023).
6. Xiang, H. J. *et al.* Rules and Mechanisms Governing Octahedral Tilts in Perovskites under Pressure. *Physical Review B* **96** (Aug. 2, 2017).
7. Lu, D. *et al.* Synthesis of Freestanding Single-Crystal Perovskite Films and Heterostructures by Etching of Sacrificial Water-Soluble Layers. *Nature Materials* **15** (Dec. 2016).
8. Pesquera, D. *et al.* Freestanding Complex-Oxide Membranes. *Journal of Physics: Condensed Matter* **34** (July 2022).
9. Hong, S. S. *et al.* Extreme Tensile Strain States in $La_{0.7}Ca_{0.3}MnO_3$ Membranes. *Science* **368** (Apr. 3, 2020).
10. Hortensius, J. R. *et al.* Ultrafast Strain Engineering and Coherent Structural Dynamics from Resonantly Driven Optical Phonons in $LaAlO_3$. *npj Quantum Materials* **5** (Dec. 16, 2020).
11. Disa, A. S. *et al.* Engineering Crystal Structures with Light. *Nature Physics* **17** (Oct. 2021).
12. Martin, T. P. *et al.* Ionic Raman Scattering and Ionic Frequency Mixing. *physica status solidi (b)* **61** (1974).
13. Ruello, P. *et al.* Physical Mechanisms of Coherent Acoustic Phonons Generation by Ultrafast Laser Action. *Ultrasonics* **56** (Feb. 1, 2015).
14. Ashcroft, N. W. *et al.* *Solid State Physics* (Saunders College Publishing, 1976).
15. Voisin, C. *et al.* Time-Resolved Investigation of the Vibrational Dynamics of Metal Nanoparticles. *Applied Surface Science. Surface Science in Micro & Nanotechnology* **164** (Sept. 1, 2000).
16. Griffiths, D. J. *et al.* *Introduction to Quantum Mechanics* Third edition (Cambridge University Press, 2018).
17. Perner, M. *et al.* Observation of Hot-Electron Pressure in the Vibration Dynamics of Metal Nanoparticles. *Physical Review Letters* **85** (July 24, 2000).

18. Shai, D. E. *et al.* Quasiparticle Mass Enhancement and Temperature Dependence of the Electronic Structure of Ferromagnetic $SrRuO_3$ Thin Films. *Physical Review Letters* **110** (Feb. 22, 2013).
19. Alexander, C. S. *et al.* Angle-Resolved de Haas–van Alphen Study of $SrRuO_3$. *Physical Review B* **72** (July 7, 2005).
20. Lee, S. *et al.* Strong Visible-Light Absorption and Hot-Carrier Injection in $TiO_2/SrRuO_3$ Heterostructures. *Advanced Energy Materials* **3** (2013).
21. De La Cruz, F. P. *et al.* Infrared Reflectivity of $SrRuO_3$. *Ferroelectrics* **185** (Sept. 1, 1996).
22. Lee, J. S. *et al.* Optical Investigation of the Electronic Structures of $Y_2Ru_2O_7$, $CaRuO_3$, $SrRuO_3$, and $Bi_2Ru_2O_7$. *Physical Review B* **64** (Dec. 4, 2001).
23. Matsuda, O. *et al.* Fundamentals of Picosecond Laser Ultrasonics. *Ultrasonics* **56** (Feb. 1, 2015).
24. Beattie, A. G. *et al.* Pressure Dependence of the Elastic Constants of $SrTiO_3$. *Journal of Applied Physics* **42** (Dec. 17, 2003).
25. Auld, B. A. *Acoustic Fields and Waves in Solids* 2nd ed (R.E. Krieger, Malabar, Fla, 1990).
26. Yamanaka, S. *et al.* Thermophysical Properties of $SrHfO_3$ and $SrRuO_3$. *Journal of Solid State Chemistry* **177** (Oct. 1, 2004).
27. Caruso, F. *et al.* Ultrafast Dynamics of Electrons and Phonons: From the Two-Temperature Model to the Time-Dependent Boltzmann Equation. *Advances in Physics: X* **7** (Dec. 31, 2022).
28. Allen, P. B. *et al.* Transport Properties, Thermodynamic Properties, and Electronic Structure of $SrRuO_3$. *Physical Review B* **53** (Feb. 15, 1996).
29. Qiu, T. Q. *et al.* Short-Pulse Laser Heating on Metals. *International Journal of Heat and Mass Transfer* **35** (Mar. 1, 1992).
30. Allen, P. B. Theory of Thermal Relaxation of Electrons in Metals. *Physical Review Letters* **59** (Sept. 28, 1987).
31. Wilson, R. B. *et al.* Thermoreflectance of Metal Transducers for Optical Pump-Probe Studies of Thermal Properties. *Optics Express* **20** (Dec. 17, 2012).
32. Choi, I. H. *et al.* Giant Enhancement of Electron–Phonon Coupling in Dimensionality-Controlled $SrRuO_3$ Heterostructures. *Advanced Science* **10** (2023).
33. Wei, T.-C. *et al.* Photostriction of Strontium Ruthenate. *Nature Communications* **8** (1 Apr. 24, 2017).
34. Damascelli, A. *et al.* Angle-Resolved Photoemission Studies of the Cuprate Superconductors. *Reviews of Modern Physics* **75** (Apr. 17, 2003).
35. Yang, H. F. *et al.* Origin of the Kink in the Band Dispersion of the Ferromagnetic Perovskite $SrRuO_3$: Electron-Phonon Coupling. *Physical Review B* **93** (Mar. 4, 2016).

36. Greener, J. D. G. *et al.* High-Frequency Elastic Coupling at the Interface of van Der Waals Nanolayers Imaged by Picosecond Ultrasonics. *ACS Nano* **13** (Oct. 22, 2019).

37. Greener, J. D. G. *et al.* Coherent Acoustic Phonons in van Der Waals Nanolayers and Heterostructures. *Physical Review B* **98** (Aug. 9, 2018).

38. Rijnders, G. *et al.* Enhanced Surface Diffusion through Termination Conversion during Epitaxial $SrRuO_3$ Growth. *Applied Physics Letters* **84** (Jan. 26, 2004).

39. Lee, M. *et al.* Self-Sealing Complex Oxide Resonators. *Nano Letters* **22** (Feb. 23, 2022).

40. Ahn, J.-H. *et al.* Effect of Annealing Conditions on Formation $SrRuO_3$ Films by Interfacial Reaction of SrO/RuO_2 Bi-Layer Films. *Microelectronic Engineering* **149** (Jan. 5, 2016).

41. Wang, K. *et al.* Coupling Among Carriers and Phonons in Femtosecond Laser Pulses Excited $SrRuO_3$: A Promising Candidate for Optomechanical and Optoelectronic Applications. *ACS Applied Nano Materials* **2** (June 28, 2019).

42. Dabrowski, B. *et al.* Reduced Ferromagnetic Transition Temperatures in $SrRu_{1-v}O_3$ Perovskites from Ru-Site Vacancies. *Physical Review B* **70** (July 21, 2004).

43. Holovský, J. *et al.* Thin-Film Limit Formalism Applied to Surface Defect Absorption. *Optics Express* **22** (Dec. 15, 2014).

5

Terahertz resonant metasurfaces

Spectroscopy using terahertz waves, which has wavelengths as long as 3 mm (0.1 THz), can be a great challenge when the samples have nanoscale dimensions, such as thin films. In this chapter, we discuss the use of resonant metasurfaces as a tool for terahertz spectroscopy, and in particular as nonlinear devices that can be used to explore strong-field physics in the terahertz range. We explain our approach to computing the scattered fields from such surfaces, and a circuit model picture that aids the understanding of their sensing capabilities and nonlinear response. As a demonstration, we use the metasurface to probe photoconductivity in a thin film, comparing it to spectroscopy without the resonators.

Optical metamaterials are composite materials containing subwavelength electromagnetic inclusions, the *metamolecules*, whose shapes and compositions are tailored to give a desired response to light. Metasurfaces are metamaterials in which these inclusion are placed in regular patterns on a surface, such as planar arrays of gapped metallic rings with a resonant electromagnetic response. Due to their deeply subwavelength size, the metasurface responds to light as an effective medium. This distinguishes them from photonic crystals, whose metamolecules have a size comparable to the wavelength of light and involve strong diffraction by design. This optical homogeneity of metasurfaces allows one to combine conventional far-field experiments with tailored electromagnetic near-field distributions at the surface, a remarkable traversal of scales.

In chapter 6 we will use metasurfaces simultaneously as a surface probe and as an electric field amplifier in pump-probe experiments. This prompts the use of a particular metamolecule design known as the *electric split-ring resonator*. These resonators are simple to fabricate, very sensitive to their local electrodynamic environment, and provide strong field enhancement at the surface.

In section 5.1 we discuss their design and the interpretation of their electrodynamic properties in terms of a simple circuit model. Details about numerical solutions of their response to light are given in section 5.2, and their function as field amplifiers in section 5.3. The last section 5.4 concerns an experiment in which the metasurface is used to probe photoconductivity of a thin film.

5.1. The electric split-ring resonator

We can calculate the scattered fields and the scattering matrix for the resonators directly using a finite-elements solver for Maxwell's equations, as discussed in section 5.2. However, exact solutions of the fields are not always helpful when forming expectations for how the metasurface will respond to perturbations—in particular, to a change in the film conductivity. Fortunately the metasurface regime, in which the dimensions of the metamolecules are much smaller than the wavelength of light with which they interact, the application of circuit theory is often valid, and the dynamics can be understood in terms of an effective circuit model.

A split-ring resonator (SRR) consists of a conducting loop, which can be understood as an inductor, and a gap or interruption at which charges can accumulate and form a coplanar capacitor. Together, this amounts to essentially an LC circuit, with a natural frequency $\omega_0/2\pi \sim 1/\sqrt{LC}$, as illustrated in figure 5.1. The induction produces an alternating magnetic field at the center of the loop, while the capacitance produces an alternating electric field strongly localized at the coplanar capacitor. The *electric* split-ring resonator (eSRR) is two opposing SRRs joined together at a common gap. The magnetic field of the two SRRs will be out of phase, producing a net zero magnetic field—in particular zero magnetic field in the gap, where the electric field is large. This design allows us to probe electric field effects, without the confounding effects of magnetic fields.

A conceptual connection between the circuit model and the effective medium picture can be made by consider the circuit impedance Z as a load on a transmission line. Specifically, assuming the metasurface is constructed as a regular lattice of resonators with lattice constant a and circuit impedance Z, the effective permittivity can be expressed as $\epsilon^* = 1 - iZ_0/(Zk_0a)$ [1].

5.1.1. Capacitance

When using a highly conducting metal such as gold to construct the resonators, R and L can be considered constant, such that all variation in an experiment comes from the capacitance C. Therefore it is instructive to consider an explicit expression for the capacitance. We estimate it as a coplanar capacitor atop a thin film on a substrate. An expression was derived by Vendik et al. [2] for such a geometry, and includes three parallel contributions: C_{vac} from the fringing fields in the vacuum halfspace, C_{film} from the thin film (with relative permittivity ϵ and C_{sub}) from the substrate (with relative permittivity ϵ_s). Making some further approximations based on our particular geometry, we obtain

$$\epsilon_0{}^{-1}C = \underbrace{\frac{2l}{\pi}\ln\left(\frac{4l}{g}\right)}_{\text{vacuum}} + \underbrace{\frac{l}{\pi}\ln\left(\frac{16D}{\pi g}\right)}_{\text{substrate}} + \underbrace{\frac{ld}{g}(\epsilon - \epsilon_s)}_{\text{film}} \tag{5.1}$$

The change in C due to a change in the relative permittivity ϵ of the film is then

$$\mathrm{d}C = \epsilon_0\,(ld/g)\,\mathrm{d}\epsilon \tag{5.2}$$

To maximize the sensitivity of the resonator to the film permittivity, one should use a narrow resonator gap g, a wide width of the coplanar plates l, and thick gold structures d. In our experiments we use $g = 600$ nm, $l = 6$ µm, and $d = 200$ nm.

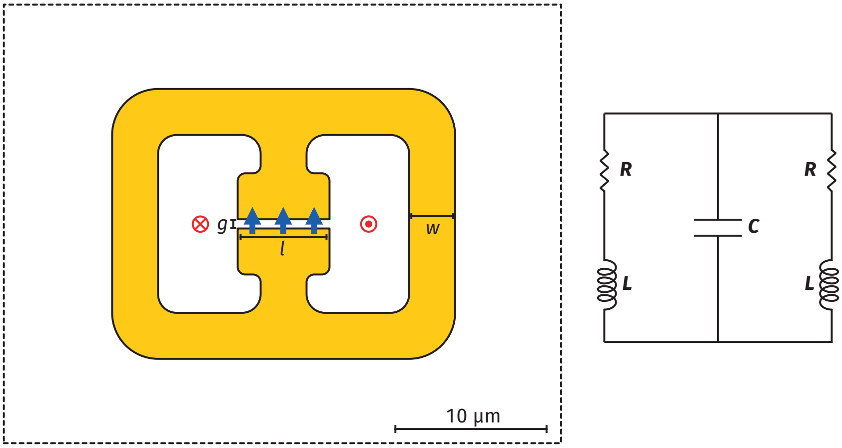

Figure 5.1: **Circuit picture of the electric split-ring resonator** *Left*: The electric split-ring resonator. Red marks denote magnetic field strength, while blue marks denote electric field strength. The frame marks the unit cell boundary. The resonator gap size g is 600 nm, the width of the coplanar capacitor is $l = 6$ µm, while the thickness of the gold structure is 200 nm. *Right*: An equivalent circuit model for the resonator.

5.2. Electrodynamical calculations

The experimental observable of a metasurface is typically the transmission or reflection amplitude; in our experiments we measure the transmission amplitude $\hat{t}(\omega)$. To extract from this the local response functions, such as the conductivity σ of a thin film under the resonators, one can calculate the expected transmission amplitude given a value for σ, then numerically minimize over σ the distance between the calculated and observed amplitudes.

To calculate $\hat{t}(\omega|\sigma)$, we solve a wave equation for the electric (and magnetic) fields resulting from scattering off of the metasurface. When the electric field is calculated, the transmission amplitude is calculated as the ratio of the electric field sufficiently far behind the surface to the incident or initial electric field. The relevant equation is a simple electric wave equation derived from Maxwell's equations,

$$\left(\mu^{-1}\nabla^2 + k^2\right)\mathbf{E} = 0, \quad k^2 = k_0^2\hat{\epsilon}(\mathbf{r},\omega) \tag{5.3}$$

Here μ is the relative permeability, k_0 is the wavenumber of the electric field in vacuum, $\hat{\epsilon}$ the relative permittivity and $\mathbf{E}$ the electric field. The problem is solved in the frequency domain because it allows for easy parallelization, with each frequency independent of the others in linear response. Geometries and material properties are encoded in the permittivity $\hat{\epsilon}$, and the initial (or source) electric field is encoded in $\mathbf{E}$ and k_0. While seemingly simple, analytic solutions are only tractable for simple geometries. In general, equation (5.3) is solved numerically.

5.2.1. Modelling a finite simulation domain

All computation happens in a finite domain, so we need to model the edges of the simulation domain. Since we are modeling a regular array of resonators, we can use periodic boundary conditions in the x- and y-directions. While the structure does not allow for reduction to a two-dimensional problem, some symmetries enable the reduction of the three-dimensional simulation volume. This is illustrated in figure 5.2. The initial electric field is polarized along the y-axis, and the problem has two mirror planes. We can therefore reduce the domain by a quarter, and model the continuity of the electric and magnetic fields by appropriate boundary conditions on the xz and yz planes. Specifically, the xz planes are modeled as perfect electric conductors (PEC), and the yz planes are modeled as perfect magnetic conductors (PMC). Imposing these boundary conditions neglects non-evanescent scattered waves, which we do not consider in this work.

The simulation domain is also finite in the propagation direction (z). We must therefore use a boundary condition prevents reflection of waves back into the simulation domain. Assuming normal incidence, a scattering boundary condition is sufficient—an approximate implementation of the Sommerfeld radiation condition.

5.2.2. Modelling the metasurface

The finite-element solver calculates the scattered electric and magnetic fields given some spatial and material composition of space. The gold microstructures which defines the terahertz resonator, as well as any thin films on the substrate, are of nanometric thickness. This poses a challenge of disparate spatial scales since we are dealing with wavelengths of 300 µm, and the planar dimensions of the resonator are of order 10 µm. Meshing the thin films will significantly increase the model size and computation time. Rather than considering the field distributions inside the thin films, we use the *transition boundary condition* (TBC) which calculates the induced surface currents on opposite sides (↑, ↓)

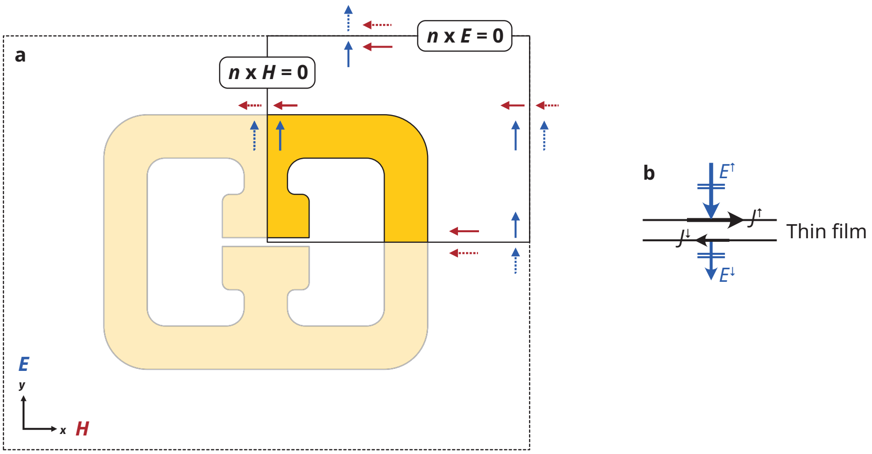

Figure 5.2: **Simulation domain and boundary conditions a**. The domain is reduced by a quarter compared to the resonator unit cell, exploiting the two mirror planes of the problem. The electric field is polarized along the y-axis. A perfect electric conductor (PEC) boundary condition is applied on the xz planes, while a perfect magnetic conductor (PMC) boundary condition is applied on the yz planes. **b**. The quantities involved in the transition boundary condition, as described in equation (5.4)

of the film, created by an electric discontinuity,

$$J_{s,z}^{\uparrow(\downarrow)} = \frac{Z_S E_y^{\uparrow(\downarrow)} - Z_T E_y^{\downarrow(\uparrow)}}{Z_S^2 - Z_T^2} \tag{5.4}$$

Here the surface impedance is $Z_S = i\omega\mu/k\tan(kd)$ and the transfer impedance is $Z_T = i\omega\mu/k\sin(kd)$, with $k = \omega\sqrt{\mu\epsilon}$ being the complex wave number. The properties of the TBC are favorable for both the gold structure and the thin film across a wide range of conductivities, as it does not assume infinite conductivity (unlike the *perfect electric conductor* boundary condition), and it is valid even when the skin depth is greater than the geometric thickness.

5.3. Resonant field enhancement

The field enhancement at the film surface is defined as $|E/E_0|$ evaluated at the center of the coplanar capacitor (the resonator gap), at the surface. The reference field E_0 is the field in the absence of the resonator, sourced as an incoming plane wave polarized across the capacitor. The field enhancement is visualized in figure 5.3, from which it is apparent

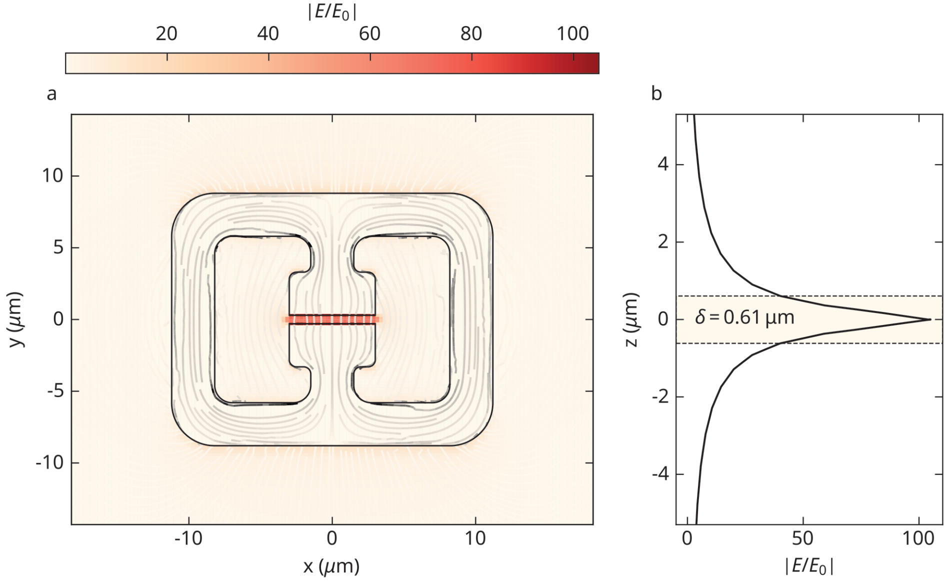

Figure 5.3: **Resonant field enhancement** **a**. The surface distribution of the field enhancement $|E/E_0|$ at 1 THz in color; lines represent surface current density on the upside, manifesting the counter-propagating currents producing alternating charge accumulation at the coplanar capacitor. The line density and color are not to scale; the current is strongly concentrated in the gold. **b**. The out-of-plane distribution, with a $1/e$ decay length of $\delta = 0.61\ \mu\text{m}$.

that the part of the film that is exposed to ample fields is the region within the coplanar capacitor. We can also define, based on the field profile, a mode volume for the 1 THz cavity: Using the width l (6 µm) and depth g (0.6 µm) of the coplanar capacitor, and the evanescent decay length δ (0.61 µm), we get

$$V = lg\delta \approx 2.2\ \mu\text{m}^3 \tag{5.5}$$

Compared to the diffraction limit (with, say, NA = 1) for a 1 THz wave in vacuum, $V_0 = (\lambda/2)^3 = (150\ \mu\text{m})^3$, the cavity mode volume is smaller by a factor of 10^6.

5.4. Film conductivity sensing

In chapter 6, the resonators will be covering a film of NdNiO_3, a material that undergoes a metal-to-insulator transition upon cooling below a critical temperature. We are therefore interested to see how the field within the capacitive gap evolves as a function of the

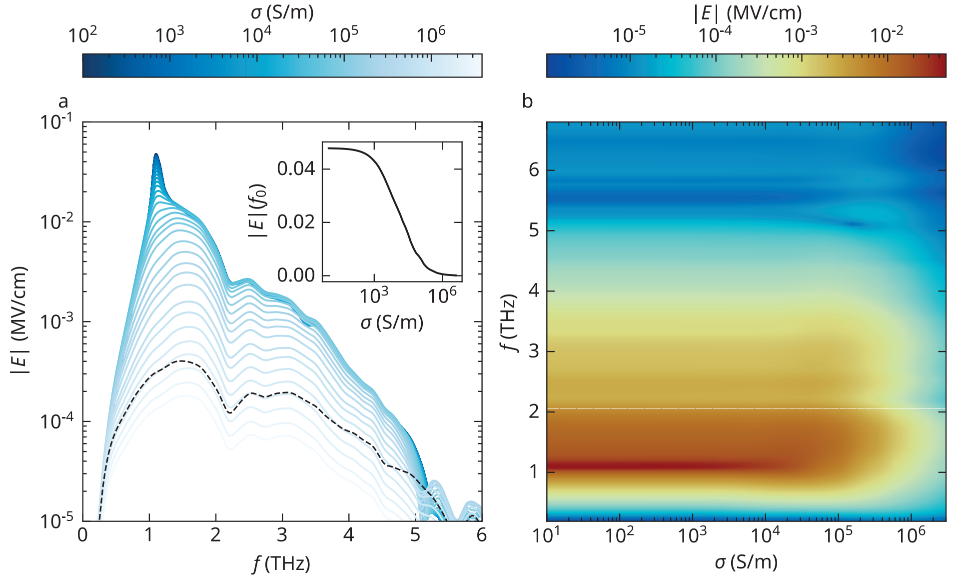

Figure 5.4: **Conductivity dependence of the local electric field spectrum a**. Frequency-resolved electric field strength, $|E| = |E(\mathbf{r} = \mathbf{0})|$, as a function of the conductivity σ of the film inside the coplanar capacitor. The incident field is shown in a dotted linestyle. A large field just above 1 THz is observed at low conductivity, and vanishes at large conductivity. **b**. Two-dimensional map of the field strength spectrum as a function of σ. The field strength is large and relatively constant until $\sigma \approx 3 \times 10^4$ S/m, above which it drops abruptly.

local film conductivity σ within the capacitive gap. The frequency-domain view of this dependence is shown in figure 5.4. The inset to figure 5.4a shows the field strength at the resonance frequency as a function of the local film conductivity, from which it is clear that the resonator amplitude is a sensitive probe of the film conductivity, with a sharp drop above 3×10^6 S/m.

In terms of a circuit model as discussed in section 5.1.1, we can consider the response of the metasurface to the conductivity σ as a change in the dielectric medium of the coplanar capacitor. The relative permittivity can be expressed in terms of the conductivity as $\epsilon(\omega) = \epsilon_\infty - i\sigma(\omega)/\epsilon_0\omega$. Inserting this into the expression for C in equation (5.1), we get

$$C_{\text{film}} \approx \epsilon_0 \, (ld/g) \, \frac{\sigma(\omega)}{i\epsilon_0\omega} \tag{5.6}$$

Far below the plasma frequency of the film, the conductivity is predominantly real-valued, and the capacitance is imaginary. Consequently, a change of conductivity is expected to manifest as a change of the resonator lifetime and amplitude. This complex capacitance can be identified as a *lossy capacitor*, being a parallel element composed of a capacitor C and a conductor G, having admittance $Y = i\omega C + G = i\omega C^*$, where

$$C^* = C_0 + (i\omega)^{-1} \underbrace{(ld/g)\sigma}_{G} \tag{5.7}$$

and C_0 is the capacitance absent the film (i.e. substrate and vacuum contributions).

5.4.1. Temporal dynamics

By calculating the inverse Fourier transform of the frequency-domain calculations of figure 5.4, we can have a temporal view of the electric field dynamics within the coplanar capacitor. This is shown in figure 5.5, together with fitting parameters from the following model for the temporal field dynamics:

$$E = E_0 \cos(\omega_0 t + \phi) e^{-t/\tau_\mathrm{d}} \tag{5.8}$$

We let E_0 have a finite rise time of 200 fs, not included in the fit for the purposes of conditioning. In line with our reasoning about the lossy capacitor of equation (5.7), we see that the lifetime, rather than the resonance frequency, exhibits the greatest sensitivity to the local conductivity.

5.5. Thin film sensing of a photodoped insulator

In the previous section, we discussed the sensitivity of the resonator to the conductivity of a thin film. We now demonstrate this by photoexciting a thin film of $NdNiO_3$, a material that is insulating at low temperatures, but can be driven into a metallic state by photoexcitation across the optical gap of about 0.5 meV [3].

5.5.1. Sample preparation

Three samples are prepared: A blanket $NdNiO_3$ film with a thickness of 30 unit cells, deposited by pulsed laser deposition on a (001)-oriented LSAT substrate, a nominally identical sample with the gold resonators deposited on top, and a blank LSAT substrate with resonators. The thin film samples were fabricated by pulsed laser deposition, and the

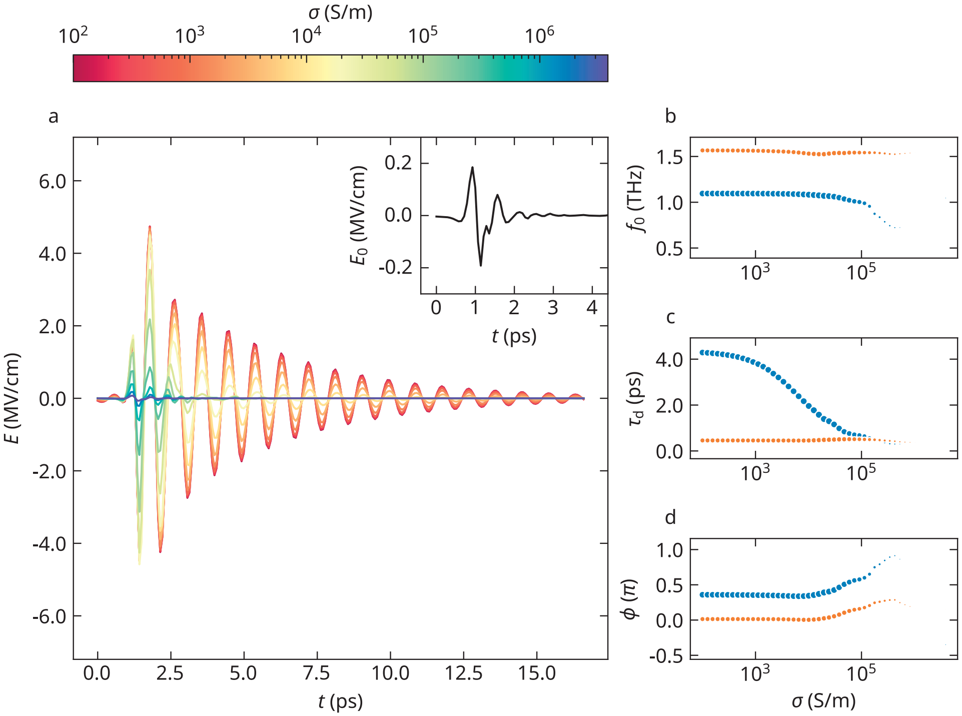

Figure 5.5: **Temporal capacitor field dynamics** **a**. Time-resolved electric field as a function of the conductivity σ of the film inside the coplanar capacitor. A large field oscillating at 1 THz is observed at low conductivity, and vanishes at large conductivity. The inset shows the incident electric field in the calculation, taken from experiment. **b-d**. Summary of film-conductivity (σ) dependence of the constants parametrizing the dynamics of the field at the center of the coplanar capacitor, according to Eq (5.8): The oscillation central frequency (**a**), decay time constant (**b**) and oscillation phase (**c**). The point size is proportional to oscillation amplitude, and color encodes the two damped oscillator components. The rise time, shared by both oscillators, was fixed to 250 fs, producing the most consistent results for the whole dataset. Notably, the 1 THz oscillation (the fundamental mode of the resonator) is strongly σ-dependent, showing considerable sensitivity to the local film conductivity. On the other hand, the faster oscillation associated with polarization of the whole gold structure is relatively robust across the full conductivity range and is less perturbed by the local environment in the coplanar capacitor.

fabrication of gold resonators was done by the author using electron-beam lithography and thermal evaporation. The fabrication recipe is given in the box below.

Metasurface fabrication recipe

1. Spin coat (4000 RPM) a layer of low-weight (MW = 495,000) polymethyl methacrylate (PMMA) diluted with 8% anisole. Bake the PMMA at 180 °C for 3 min and let cool for 1 min.
2. Spin coat (4000 RPM) a layer of high-weight (MW = 950,000) PMMA diluted with 4% anisole. Bake the PMMA at 180 °C for 3 min and let cool for 1 min.
3. Evaporate 4 nm of gold (to minimize charging due to the e-beam).
4. Expose the metasurface pattern using an electron beam. A 100 kV beam was used, with a dose of 800 μC/cm^2 and spot size of about 30 nm.
5. Dissolve the gold layer with gold etchant (KI) for 5 s. Rinse with deionized water.
6. Develop the exposed PMMA in a 1:3 mixture of methyl isobutyl ketone and isopropyl alcohol for 1 min. Rinse in pure isopropyl alcohol.
7. Evaporate 5 nm Cr (for better adhesion) and 200 nm Au.
8. Leave sample in 45 °C acetone for 1 h. Complete lift-off with weak ultrasound.
9. Rinse in acetone followed by isopropyl alcohol.

5.5.2. Measurement

We compare the metasurface transmission amplitude spectra with and without the presence of a thin film in figure 5.6a and b. The thin film of $NdNiO_3$ undergoes a metal-insulator transition which manifests as a disappearance of the metasurface resonance at high tem-

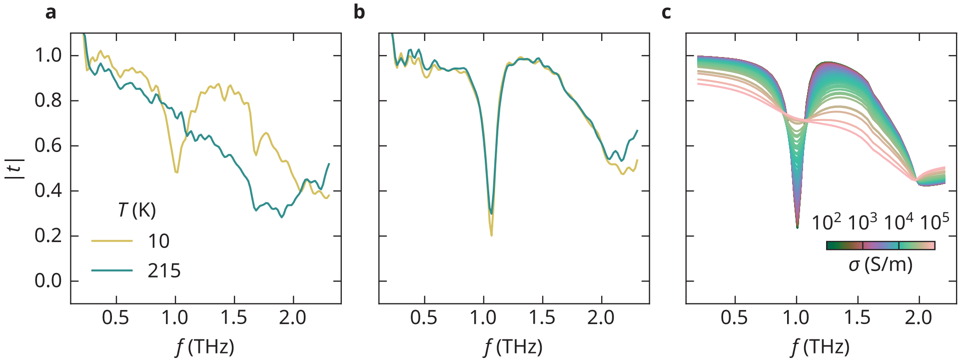

Figure 5.6: **Transmission spectra** Comparison of transmission magnitude $|t|$ for **a**. the metasurface sample with a $NdNiO_3$ film grown, and **b**. a metasurface patterned directly on the LSAT substrate (no film). **c**. The transmission magnitude for a range of film conductivities, calculated.

perature (a), in stark contrast to the metasurface supported by a substrate without a thin film (b). We also show in figure 5.6c the calculated transmission amplitude for a range of film conductivities, from which the conductivity of the film can be inferred.

Having established that the metasurface responds strongly to the thin film conductivity, we measure the response to photoexcitation from the insulating phase. Figure 5.7 summarizes the findings, showing the differential (pump-induced change) transmitted electric fields ΔE measured 20 ps after photoexcitation above the optical gap. The blank film response scales with the fluence quadratically, while the metasurface response is nearly linear, showing much greater sensitivity at low fluences. This shows that metasurfaces may be used for ultrafast conductivity sensing for ultrathin films or weak excitation conditions.

5.6. Data availability

The code used for the analysis and calculations of this chapter and chapter 6 are accessible at the DOI 10.5281/zenodo.12752052.

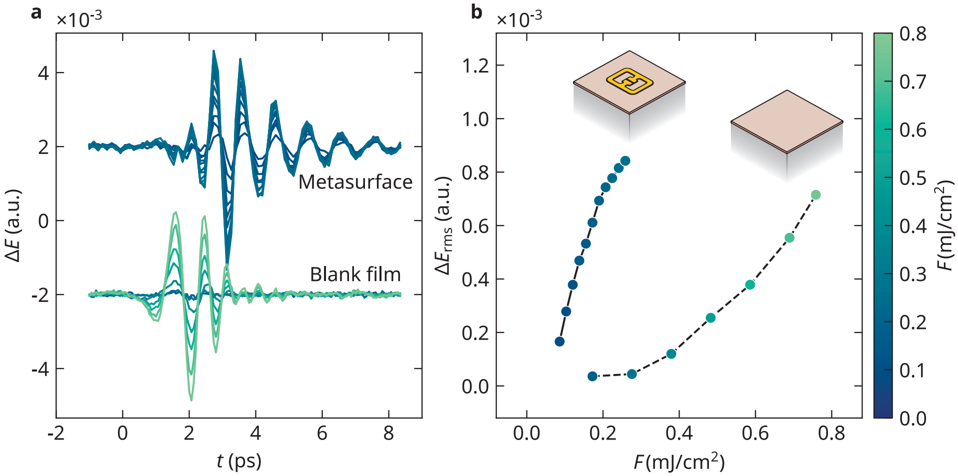

Figure 5.7: **Conductivity sensing** **a**. Differential probe waveforms as measured shortly after photoexcitation well above the optical gap at $\hbar\omega = 0.95$ eV, creating photoconductivity. The color represents the fluence F of the pump pulses. The metasurface response is a damped 1 THz oscillator, while the response of the blank film has the spectral content of the probe pulses. **b**. The root-mean-square of the differential signal, ΔE_{rms}, shows a marked difference in the fluence susceptibility. The fluence dependence for the blanket film has a quadratic dependence, requiring fluences in excess of 0.4 mJ/cm^2 to reach detectibility in our apparatus. The metasurface on the other hand has a detectable response even below 0.1 mJ/cm^2, closer to a linear dependence.

References

1. Tretyakov, S. *Analytical Modeling in Applied Electromagnetics* (Artech House, 2003).
2. Vendik, O. G. *et al.* Modeling and Calculation of the Capacitance of a Planar Capacitor Containing a Ferroelectric Thin Film. *Technical Physics* **44** (Apr. 1, 1999).
3. Ruppen, J. *et al.* Optical Spectroscopy and the Nature of the Insulating State of Rare-Earth Nickelates. *Physical Review B* **92** (Oct. 27, 2015).

6

Metallization of a correlated insulator with terahertz fields

In rare-earth nickelates, spontaneous charge localization occurs at low temperatures due to a complex interplay of strong bond covalency, electron-electron repulsions, and structural distortions. Here, we couple $NdNiO_3$ to a resonant metasurface which sustains strong local electric fields exceeding 10 mV/Å oscillating at terahertz (THz) rates. In this regime, the electric potential energy is comparable to the charge gap of the localized carriers, producing strong tunneling into conducting states. Using THz pump-probe measurements, we find that charges can transiently delocalize within one picosecond, relaxing back to the insulating state in a non-trivial way.

In the rare-earth nickelates ($RNiO_3$), a competition of energies gives rise to electron localization and insulating behavior at low temperatures, a subject of intense theoretical and experimental study [1]. The interplay of bond covalency, electron-electron interactions, and structural distortions that result in localization also makes the electrons susceptible to delocalization by external perturbations: conductivity within their insulating phase has been induced using ionic liquid gating [2] and high-density currents [3], and out of equilibrium at short timescales by photodoping [4] and resonant phonon excitation [5].

The delocalization of charges in otherwise insulating systems may be achieved by photodoping: Exposing a material with light whose photon energy ($\hbar\omega$) exceeds the charge gap (Δ_g) of the insulator will produce a population of itinerant quasiparticles and an associated photoconductivity. With photon energies below the charge gap, only higher-order effects can produce photoconductivity, such as multiphoton absorption where an integer number N of photons are absorbed such that $N\hbar\omega \geq \Delta_g$. However, as $\hbar\omega/\Delta_g \rightarrow 0$, such an event becomes exponentially unlikely and requires fields of large amplitude. At large amplitude, however, another process dominates, and this is the situation we study in this work.

With sufficiently strong fields, the electric potential energy $V \approx eaE_0$ (a being the lattice constant) between localized charges can be comparable to Δ_g. Landau, Zener, and Stückelberg (LZS) [6–8] applied the theory of tunneling to the then-recent theory of band insulators: An electric field of strength E_0 tilts the valence and conduction bands making them degenerate and separated by a tunneling barrier of length $L = \Delta_g/eE_0$. They calculated that the tunneling probability of an electron into the conduction band had the form

$$P(E_0) \propto \exp\left(-\pi\frac{E_{\mathrm{th}}}{E_0}\right) \tag{6.1}$$

which has a threshold behavior at $E_0 = E_{\mathrm{th}}$. This non-perturbative result (singular at $E_0 = 0$) appears to apply with equal validity to arbitrary many-body wavefunctions [9] such that it may be used for insulators other than band insulators, only with renormalized values for the model parameters. One example is the Mott insulator [10], where the threshold field E_{th} was shown to be related to the Mott gap Δ_{Mott} and the doublon-holon correlation length ξ as $E_{\mathrm{th}} = \Delta_{\mathrm{Mott}}/(2e\xi)$.

We study the response of the conductivity of the correlated insulator $NdNiO_3$ to electric fields in the tunneling regime. Since a constant electric field of that magnitude is known to cause a phase change that is not related to tunneling, involving the formation of conducting paths caused by nanoscopic current heating [3], we conduct our experiment at high frequency: Using a resonant metasurface as discussed in chapter 5, we generate strong alternating electric fields in terahertz, which avoids the thermal breakdown that occurs on the nanosecond (gigahertz) scale [3]. We take advantage of the strong sensitivity of the metasurface response to the local conductivity of a supporting thin film, using it simultaneously as a field amplifier and as a conductivity sensor on the ps timescale in a terahertz pump-probe scheme.

6.1. Electronic structure and excitations

The materials in the $RNiO_3$ family are insulators that, according to band theory, should be conductors. The reasons for this have been a matter of great discussion [1], which we detail in the supplementary section S1.4; a simplified picture of the electronic structure is shown in figure 6.1. The metallic ground state is understood in terms of the single, unpaired Ni-e_g electron that has hybridized with O-2p to form a covalent frontier orbital and may be interpreted as a $3d^7$ state doped with an electron from the oxygen ligands. This notion is referred to as self-doping [11] and is a manifestation of a negative charge-transfer energy in these compounds [12]. It was understood that as the system goes insulating below T_{MI}, a disproportionation transition occurs in which the oxygen holes cluster onto half the sites, forming small NiO_6 octahedra with an $S = 0$ orbital and short Ni-O bonds; the remaining half of the sites are correspondingly larger octahedra with long bonds and $S = 1$ [1]. Such a transition is referred to in the literature as bond disproportionation [11]. Park et al. [13] found in a dynamical mean-field study that the large sites have the spin susceptibility and the self-energy characteristic of a Mott system. They argued that these sites undergo a Mott transition, baptizing it a *site-selective* Mott transition, since the small sites—having constant self-energy—play no essential role in this transition.

The nature of the charge gap $\Delta_g \approx 0.6$ eV [14] depends on the size of the Mott gap of the large-site bands: If the corresponding upper Hubbard band is the lowest unoccupied band, then the charge gap is just the Mott gap. If the Mott mechanism has pushed the upper Hubbard band even above the energy difference between large and small sites, the charge gap is an intersite charge transfer. Experiments seem to indicate that the latter is the case [14]. Given the many interactions that conspire to produce the charge

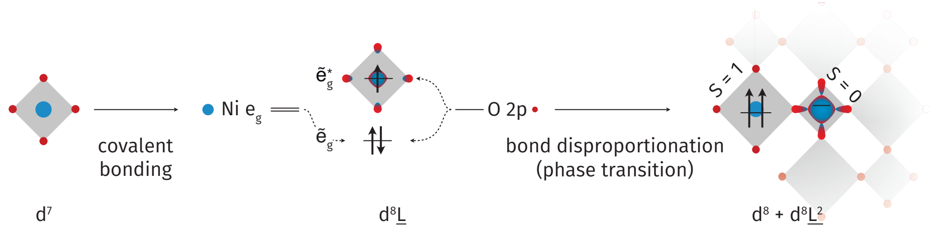

Figure 6.1: **Electronic structure of $RNiO_3$** In the metallic ground state, the electron in the Ni-e_g ionic orbital has bonded with the O-2p ligands, forming bonding ($\tilde{e}_g$) and antibonding ($\tilde{e}_g^*$) orbitals, understood as Ni-d^8 and a distributed hole $\underline{L}$ on the oxygen ligand (conventionally denoted $d^8\underline{L}$). The phase transition involves a disproportionation of the $\tilde{e}_g^*$ orbitals, with alternating double/empty occupation of the ligand hole on the Ni sites. As a function of the disproportionation amplitude, electronic correlations open up a charge gap Δ_g in the ($\tilde{e}_g^*$)bands.

gap, one can expect its dependence on external perturbations, such as electric fields or photodoping, to be quite different from that of a band insulator, where the band gap can be considered constant over a wide range of perturbations.

6.2. Linear spectroscopy of the metal-insulator transition

The metal-insulator transition in $NdNiO_3$ is detectable in spectroscopy as a change in optical conductivity. We study the transmission amplitude of a blanket film of $NdNiO_3$ grown epitaxially on (001)-oriented LSAT to a thickness of 30 unit cells using pulsed laser deposition. We characterized the sample using terahertz spectroscopy, summarized in figure 6.2a. A hysteretic metal-insulator transition occurs in the range 160 K to 185 K, with the film transparency becoming indistinguishable from unity below the transition in our experimental resolution. Using electron beam lithography and the lift-off method as detailed in section 5.5.1, we deposit gold resonators on a nominally identical film and measure its transmission amplitude as a function of temperature. The conductivity is extracted from comparison to full-wave calculations (see section S1.2), using a Drude model for the conductivity,

$$\sigma(\omega) = \sigma_0/(1 - i\omega\tau)$$

We take the scattering time that gives the smallest global difference between experiment and calculation ($\tau = 65$ fs). Unless otherwise specified, we approximate the scattering time to be constant across all measurements in this work, noting that it does not significantly change the estimations of σ_0. The conductivity, shown in figure 6.2b, exhibits the

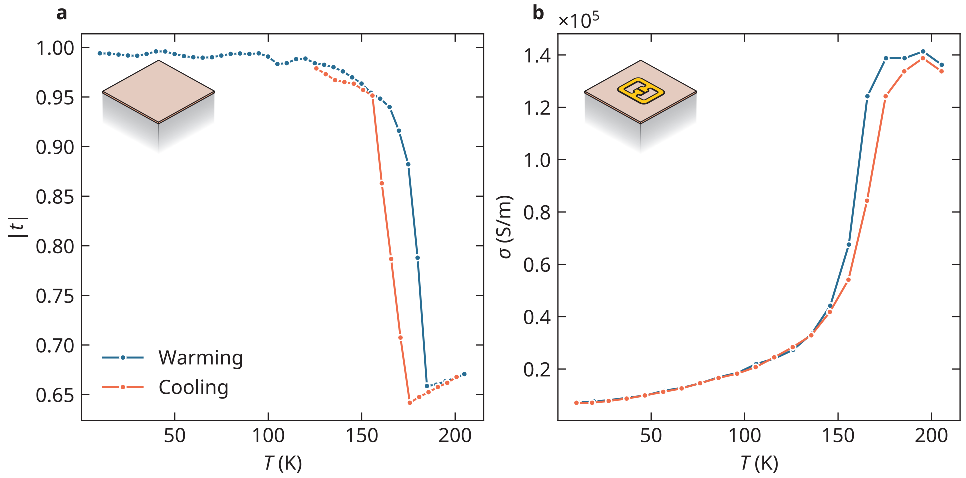

Figure 6.2: **Spectroscopy of the thermal metal-insulator transition** **a**. Frequency-averaged transmission amplitude of a blank film, for two directions of the temperature incrementation. **b**. Temperature dependence of real conductivity (static limit) of the film under the resonators, estimated using full-wave simulations.

metal-insulator transition in the same range of temperatures. The hysteresis region is smaller, which is not unsurprising given that the transition is of first order, and involves a phase coexistence and a nucleation process known to correlate with substrate morphology [15]. The addition of surface structures, the resonators, may introduce pinning sites or minor local strains that affect the nucleation process.

6.3. Nonlinear spectroscopy

The electrodynamics of the metasurface involves strongly concentrated electric fields penetrating the correlated insulating film within the capacitive gaps of the resonators. We study the nonlinear response of the metasurface by transmitting waveforms through the device at increasing field strengths E_0. For the analysis, we consider the *normalized* waveforms,

$$E(t|E_0) \longrightarrow \frac{E(t|E_0)}{\sqrt{U(E_0)}} \tag{6.2}$$

where $U(E_0)$ is the corresponding energy of the incident probe field (not transmitted through the sample). If the response is linear, we will have field strength independence, $\bar{E}(t|E_0) = \bar{E}(t)$. We consider the transmission amplitude at temperature conditions (T, E_0) *relative to* that of the device at the reference conditions $(T_{\text{min}}, E_{0,\text{min}})$ where the response is in the linear regime ($T_{\text{min}} \approx 5\,\text{K}$ and $E_{0,\text{min}} \approx 6\,\text{kV/cm}$). This amplitude we define in the frequency domain as

$$t(\omega|E_0, T) = \frac{\hat{E}(\omega|E_0, T)}{\hat{E}(\omega|E_{0,\text{min}}, T_{\text{min}})} \tag{6.3}$$

Figure 6.3 show its magnitude as a function of field strength E_0 for three temperatures. The transmission magnitude does not vary with the field strength at the temperature above T_{MI}. That is in stark contrast to the response at low temperatures: The transmission at 1 THz varies by nearly 100 %, corresponding to a complete suppression of the resonant response.

We attribute the nonlinearity of the resonators to a nonlinear conductivity $\sigma(E_0)$. The nonlinearity needs only be considered within the coplanar capacitor since the electric fields are smaller outside this region by at least two decades. In the circuit language of chapter 5, we can understand this as a nonlinear capacitance changing as $\Delta C(E_0) \sim \Delta\sigma(E_0)/i\omega$ (see section 5.4).

Inspecting the field strength dependence of the transmission magnitude at the resonance frequency, displayed in figure 6.3c, we also find a remarkable similarity of the field strength dependence between the two temperatures, 3 K and 50 K; that is, aside from an offset due to a different equilibrium conductivity. That rules out a Poole-Frenkel effect in which the electric field lowers the activation barrier for thermal excitation and leads to a conductivity $\sigma = \sigma_0 \exp(\alpha\sqrt{E}/k_B T)$ [16]. It is also an indication that $\Delta\sigma$ is not produced by a subpicosecond change in temperature, considering that the specific heat—which determines the temperature change given an amount of absorbed energy—differs by a factor of about 20 between these two temperatures [17].

6.4. Pump-probe spectroscopy

The nonlinear response of the insulator (section 6.3) to electric fields implies that whatever local change occurs in the conductivity σ occurs on a timescale at least as fast as the resonator period (1 ps). Measuring the dynamics of this requires temporal separation of pump and probe, which we achieve by generating a pair of THz pulses, one weak for probing and one variable-strength pulse for pumping; the two are delayed relative to each other by a movable mirror. We further detail the experimental setup in the supplementary section S1.1. Unless otherwise specified, the sample temperature is kept at 5 K.

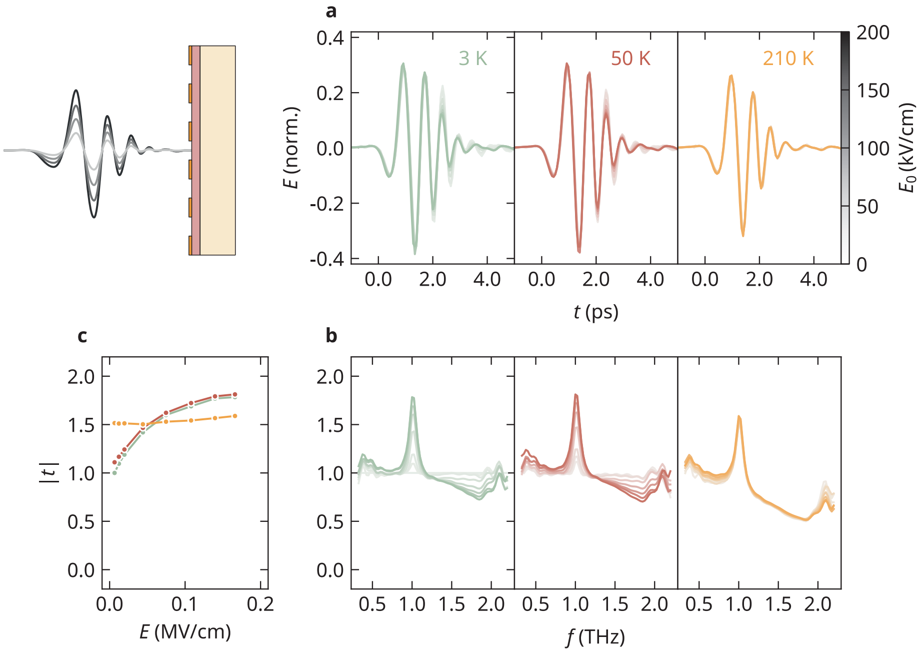

Figure 6.3: **Nonlinear spectroscopy of the metasurface** **a**. Electro-optically sampled waveforms after transmission through the metasurface device, normalized by the energy of the incoming field. **b**. Transmission magnitude as defined in equation (6.3), defined relative to base temperature. **c**. Comparing the field strength dependence of the transmission magnitude at 1 THz for the three temperatures.

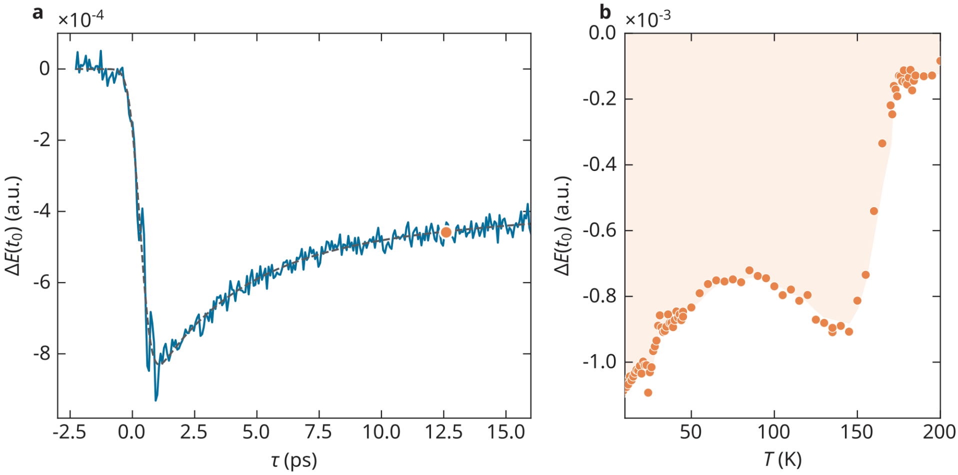

Figure 6.4: **Fixed-sampler pump-probe trace a**. Decay dynamics with a double-exponential fit in black, with one few-picosecond relaxation process ($\tau_1 = 3.8(3)$ ps) and one slower relaxation process on subnanosecond timescale ($\tau_2 = 217(182)$ ps). **b**. Temperature dependence of $\Delta E\left(t_0\right)$ at a fixed pump-probe delay of 13 ps.

The most straightforward measurement is to continuously record the electric field of the probing waveform at some time slice t_0 and vary the delay of the pump pulse τ relative to the probe. This method, which we will call the *fixed-sampler scan*, is illustrated in figure 6.5b. We use the value of t_0 where the largest change occurs. A fixed-sampler scan is shown in figure 6.4a, where a sudden jump in ΔE is observed at a very fast timescale, followed by a relaxation. Under the assumption of exponential decay, the relaxation process requires *two* exponential functions in linear combination. One of these is a few-picosecond relaxation process, with time constant $\tau_1 = 3.8(2)$ ps; the other is a slower relaxation proceeding on a subnanosecond timescale, with time constant $\tau_2 = 217(182)$ ps. The considerable uncertainty on τ_2 is due to a limitation of the measurement window to about 20 ps because of the reflection of the pump pulse at the back of the sample, causing it to return to the surface and re-excite the cavities at a little less than half the amplitude.

Measuring the change ΔE at a time delay of 13 ps as a function of temperature, shown in figure 6.4b, shows that the pump-induced signal appears from the insulating phase but is hardly present when starting from the metallic phase. Moreover, the largest changes are not close to T_{MI} but at the lowest temperatures where the sample conductivity is smallest at equilibrium.

6.4.1. Carrier generation

Rise time

Using a fixed-sampler scan, we measure the rise time dynamics in figure 6.5a. We find a rise time of less than 1 ps, consistent with the existence of a nonlinear response as discussed in section 6.3. This rise time is only an upper bound on the true rise time due to the finite temporal resolution of the experiment.

We verify that the dynamics of figure 6.5a can be understood as dynamics purely of the local conductivity within the capacitive gap by performing a *two-dimensional scan* of $E(t, \tau)$ across the sampler time t and the pump-probe delay τ. We take the Fourier spectra along t to find the instantaneous transmission amplitude and calculate the local conductivity σ based on the calculated transmission amplitudes as described in section S1.2. At these short timescales, the conductivity changes within the probe pulse duration, which violates the assumptions of the calculations. Therefore, we only consider the extracted conductivity dynamics to be an indication of the true dynamics. The results, shown in figure 6.5c, reveal that the conductivity dynamics proceed on the same timescales inferred from the fixed-sampler scans. In the supplementary, we also show in figure 6.5 that the rise time is independent of both the pump field strength and the temperature.

The electrodynamic calculations of chapter 5 yield the electric field within the resonator, $E_{\text{gap}}(t)$. In figure 6.5a we show the cumulative energy,

$$U(t) = \int_{-\infty}^{t} \mathrm{d}t' \, E_{\text{gap}}^2(t') \tag{6.4}$$

which turns out to have a rise time comparable to that of the conductivity. We can, therefore, conclude that the real rise time is at least as fast as the accumulation of energy in the resonator.

A rise time faster than 1 ps rules out several scenarios. One known effect is the formation of conducting regions in $NdNiO_3$ due to resistive heating from continuous currents [3]. Heat buildup in local hot spots can lead to a cascading effect where the film becomes conducting through a percolation transition of the hot regions, ultimately shorting the electrodes used for current sourcing. However, the rise time of this effect is on the order of 1 ns, three orders of magnitude slower than we observe. A related possibility that we can exclude based on the fast rise time is local heating close to the gold in

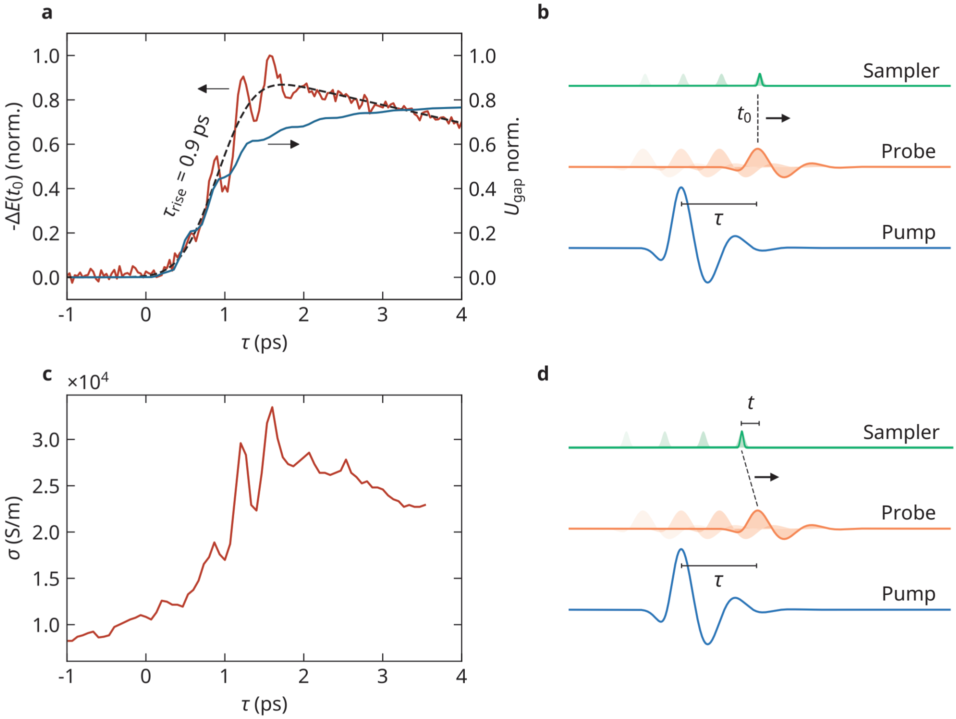

Figure 6.5: **Rise time dynamics** **a**. A fixed-sampler scan of the probe waveform over the pump-probe delay τ, in pink. The cumulative integral of the calculated local electric field within the resonator is shown in dark blue on the twin axis. The rise time τ_{rise} is the time it takes for the signal to reach 90% of its maximum value. Note that the oscillations are an artifact of the detection system caused by higher-order optical responses occurring when both THz pulses are propagating in the electro-optic crystal. **b**. Explanation of the 1D scan. The relative delay of the probe and sampler is fixed, while their common delay relative to the pump is varied. The amplitudes are not to scale. **c**. The estimated local conductivity of the film in the resonator gap. Moderate pump field strength was used in this experiment, so the changes were small to avoid saturation of the conductivity influencing the estimate of the rise time. These estimates require full measurements of the probe waveform, requiring a 2D scan. **d**. The delay τ moves the sampler and probe together relative to the pump; the delay τ moves the sampler relative to the probe.

the coplanar capacitors, which would only diffuse across the distance between the strips ($g = 600\,\mathrm{nm}$) in $300\,\mathrm{nm}/4\,\mathrm{nm\,ps^{-1}} = 75\,\mathrm{ps}$, much too slow.

Considering whether the conductivity dynamics can be explained as the result of the local temperature within the coplanar resonator requires modeling not undertaken in this work due to the lack of several crucial material properties necessary for a reliable estimate. For a two-temperature model, this includes the electron-phonon coupling, the latent heat, and the specific heat at low temperatures due to electrons and phonons. Such modeling was, however, done for VO_2, for which these properties are known, by Liu et al. [18] at very similar experimental conditions. They found that the accumulated temperature was about 20 K, such that a nonlinear terahertz response of VO_2 was only observable at temperatures within 30 K from the transition temperature (340 K). Since our experiments on $NdNiO_3$ take place at 5 K, and the phase transition occurs at 175 K, the temperature elevation would be required to bring about a thermal phase transition would be 170 K. Such a temperature change at this timescale exceeds what we consider a plausible heating effect. As discussed in section 6.4.2, thermal dynamics may nevertheless play a role in the decay dynamics at long timescales.

Electric susceptibility

The relationship between the photoconductivity and the field strength of the pump can be used to infer the excitation mechanism. In figure 6.6, we study how the conductivity of $NdNiO_3$ within the capacitive gap varies with the pump field strength E_0, at a fixed delay (a) or a fixed temperature (b).

Considering the effect of temperature on the field strength dependence in figure 6.6b, temperature contributes only constant background but does not scale the curves, i.e., the derivative $\partial\sigma/\partial E$ does not appear to depend on temperature. This indicates that the conductivity change is not caused by approaching the metal-insulator transition thermally since a strong temperature dependence of the slope would be expected in that case.

The relationship between conductivity and field strength does not follow either a linear, quadratic, or exponential form. The experiment occurs in a regime in which the strength (E_0) is comparable to the charge gap (Δ). Specifically, the electric potential energy for a field strength of $E = 4\,\mathrm{MeV/cm}$ across one lattice site ($a = 0.4\,\mathrm{nm}$) is $aeE = 160\,\mathrm{meV}$. Comparatively, the optical gap of bulk $NdNiO_3$ is $\Delta = 300\,\mathrm{meV}$ [19], putting the system in a regime where tunneling through the charge gap should be significant.

If the conductivity change is caused by tunneling, it should be proportional to the number of tunneled carriers, $N \approx P(E_p)\Delta t$, with E_p the peak electric field and Δt a measure of the pulse duration. Based on equation (6.1), we expect the conductivity to go as

$$\sigma = \sigma_0 + a \exp(-\pi E_{\text{th}}/E_p) \tag{6.5}$$

In figure 6.6b we fit this expression to the data at $\tau = 20$ ps. A finite time delay was used for this analysis because the conductivity changes rapidly at $\tau = 0$, and nonlinear effects in the dielectric substrate may contribute to the signal during the presence of the pump field [20]. The threshold fields obtained from these fits are $E_{\text{th}} \approx 69(6)$ kV/cm, with no clear temperature trend. Note that this field strength corresponds to the incident free-space electric field—the resonator amplification brings this to a value of 1.4 MV/cm within the capacitive gap. Over a pseudocubic lattice constant of 0.4 nm, roughly the distance between two Ni sites, the estimated E_{th} corresponds to a potential energy of about 60 meV. Comparatively, the charge gap of NdNiO_3 thin films as taken from optical spectroscopy is near $\Delta_g = 0.5$ eV [14]. In the theory of nonlinear doublon production in the one-dimensional Hubbard model, the threshold field is $E_{\text{th}} = \Delta_{\text{Mott}}/2e\xi$, where ξ is the correlation length of doublon-holon pairs. The fluctuations in NdNiO_3 are, as discussed in section 6.1, either intersite charge-transfer between small and large octahedra, or doublon-holon pairs on the large octahedra. The characteristic length of these fluctuations ξ is in this picture equal to 1.8 nm, roughly four times the lattice constant, which seems a reasonable value [21].

6.4.2. Relaxation

The fixed-sampler scan of $\Delta E(t_0, \tau)$ along τ is proportional to the transmission magnitude at resonance $t(\omega_0)$ provided that is the only frequency component of the metasurface spectrum that changes. For an estimate of the actual local conductivity change $\Delta\sigma$, we sample the whole transmitted probe waveform $E(t)$ across a wide range of pump-probe delays τ and infer σ based on full-wave calculations. The result is shown in figure 6.7. We fit a linear combination of exponential functions to the data and include the effect of the reentrant pump pulse around 20 ps as a free parameter. We find that the minimal number of exponential functions required to fit the data is three, with one short time constant $\tau_1 \approx 2$ ps, and two longer constants $\tau_2 \approx 100$ ps and $\tau_3 \approx 1$ ns. The simplest relaxation

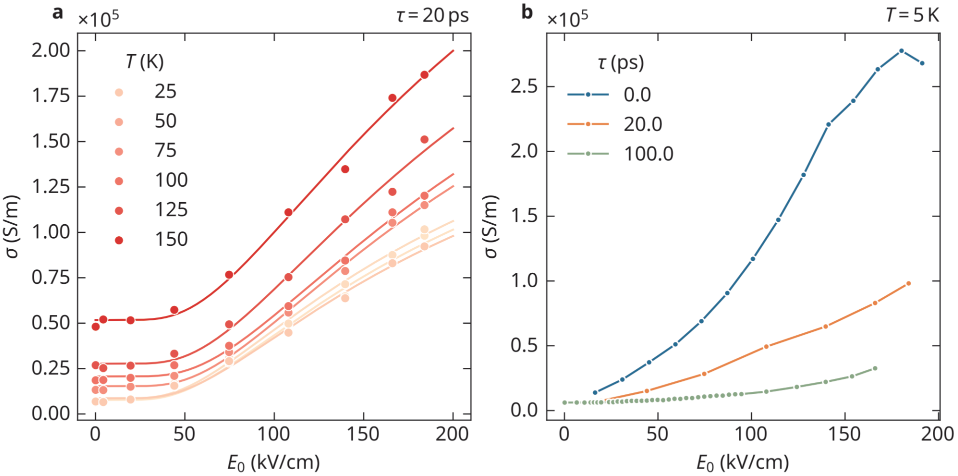

Figure 6.6: **Field strength dependence** **a**. Conductivity σ within the capacitive gap of the resonators, measured as a function of field strength at a set of temperatures T, while the pump-probe delay τ is kept fixed at 20 ps. **b**. The conductivity shown as a function of the incident peak field strength E_0 of the pump pulse. The sample temperature is kept at 5 K during this measurement, and the conductivity is measured at three values of the pump-probe delay τ, with the pump arriving at $\tau = 0$.

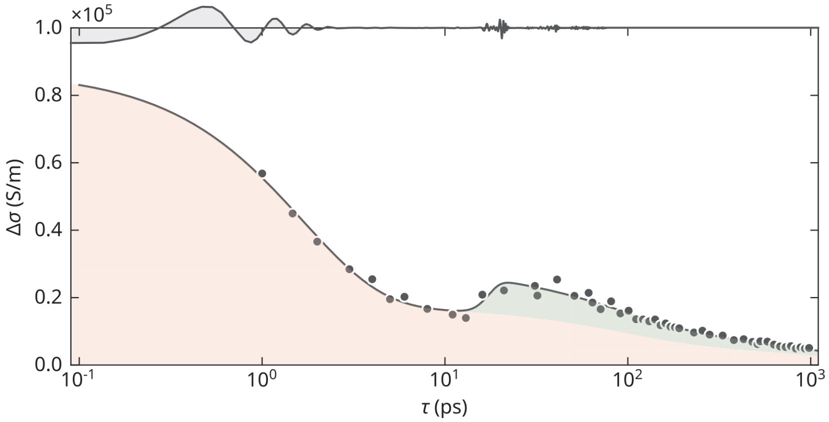

Figure 6.7: **Decay dynamics of conductivity** The change in conductivity $\Delta\sigma$ as estimated by sampling a full probe waveform for pump-probe delays τ up to 1 ns, and match the experimental transmission amplitude with full-wave calculations. The reentrant dynamics at 20 ps is caused by the pump returning to the sample surface after partial reflection at the substrate backside. A measurement of the pump field is plotted on the top spine. We fit a multi-exponential model to the data, giving the following point estimates for the time constants: $\tau_1 \approx$ 2 ps and $\tau_2 \approx$ 100 ps, as well as a relaxation process with $\tau_3 =$ 1600 ps that appears after the second pump. The effect of the pump echo is included additively, and the contributions from the initial excitation (red) and the addition of the second pump (green) are shaded in separate colors.

model is the single exponential decay, resulting from a single relaxation process with a constant relaxation time, $\sigma = \sigma_0 e^{-t/\tau}$. To get multiple timescales, as we observe, the relaxation process must either involve consecutive events or the conductivity must decay due to the relaxation of distinct subsystems (simultaneous, parallel processes will just change the effective τ). A multistep relaxation pathway that involves such vastly different timescales would be highly unusual. More plausibly, the longer timescale is due to the evolution of a different subsystem—the lattice. Immediately following the creation of the initial photoconductivity, the system can sustain larger currents, such that the local temperature increases while the highly damped resonators ring down. While the quasiparticles decay on the fast τ_1 timescale, the thermodynamic process of thermalizing with the resonators and with the substrate takes a longer time (τ_2). The third timescale (τ_3) may arise due to the reentrant pump, which, acting on the remaining population of carriers, introduces some additional thermal energy into the system.

While a multi-exponential empirical model appears to fit the data, the relaxation dynamics may not adhere to a model involving constant decay times. In the Hubbard model, doublon-holon recombination time is exponential in the charge gap [22, 23], i.e., $\tau \propto \exp(\Delta_g/\beta)$ for some characteristic energy β. The circumstances are likely similar for $NdNiO_3$. While the charge gap remains largely unchanged after photoexcitation or carrier injection in a band insulator, the charge gap of a correlated insulator is a dynamic quantity that can be renormalized by the presence of carriers [24, 25]. After the initial change in conductivity due to the driving of the resonator, the charge gap will grow back to its equilibrium value as excitations decay. Consequently, the decay time will increase over time rather than remain constant. We note that, on the log-log scale of figure 6.7, the data points preceding and those succeeding the reentrant pump appear linear. This would correspond to a power-law decay, which can result from specific time-dependent decay rates [26]. We cannot distinguish between multi-exponential and power-law decay with the current data alone.

6.5. Photodoping

Pulses of photon energy far above the optical gap of $NdNiO_3$ produce a nonequilibrium population of excited states, putting the system in a state akin to the one caused by quantum tunneling. If the field-induced effect is due to tunneling, we expect similar decay dynamics for the photodoped state as for the field-driven state. In figure 6.8 we show

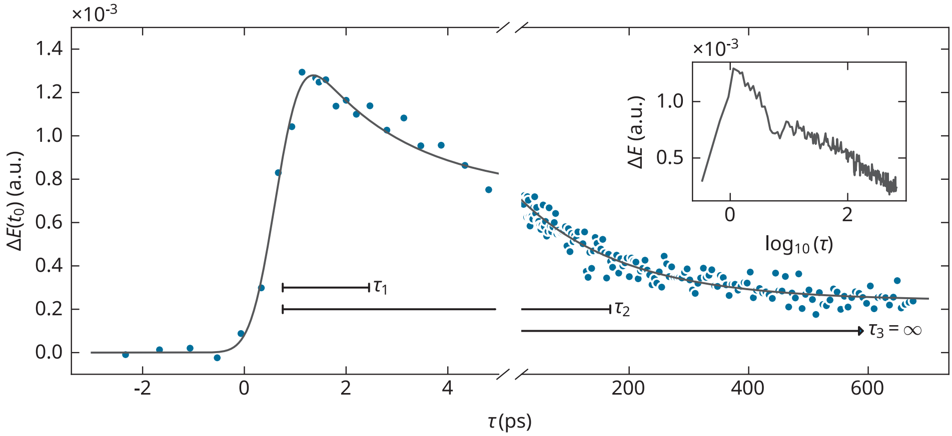

Figure 6.8: **Photodoping timescales** The change ΔE in the transmitted electric field in a fixed-sampler scan over pump-probe delay τ. The inset shows the data in logarithmic time. A three-exponential empirical model produces the point estimates $\tau_1 = 1.8(2)$ ps, $\tau_2 = 174(11)$ ps for the decay times, with τ_3 set to infinity. The rise time is below the experimental resolution due to the limited bandwidth of the terahertz pulses.

the rise and decay dynamics of the photodoped state, using pump pulses with 0.95 eV photon energy and a pulse duration of about 100 fs. We use a fluence such that the response has just saturated, corresponding to a complete suppression of the metasurface resonance. The dynamics are strikingly similar between the two experiments: The rise time is resolution-limited as in the field-driven experiments. Similarly, the relaxation dynamics require three time constants comparable to those of the terahertz field excitation.

6.6. Conclusion

We have studied the response of the correlated insulator $NdNiO_3$ to strong electric fields. Through the use of a split-ring resonator metasurface that exhibits a ×20 local field amplification, with a resonance frequency in the adiabatic tunneling regime, we observe a subpicosecond growth of conductivity. We study the field strength dependence of this conductivity change, including at different temperatures, and conclude that its origin is consistent with a Zener-like tunneling process. Our work demonstrates the use of resonant metasurfaces that support strong local fields as a tool for studying strong-field physics in thin films or surfaces, serving both as a field amplifier and a local conductivity sensor.

6.7. Data availability

The data recorded in the experiments of this chapter, the code used for the analysis and calculations (including those of chapter 5) are accessible at the DOI 10.5281/zenodo.12752052.

6.8. Acknowledgements

M. Matthiesen measured and analyzed the terahertz experiments, designed and prepared the microfabrication of gold split-ring resonators on the thin film, and wrote the manuscript; M. Hadjimichael deposited the $NdNiO_3$ films by pulsed laser deposition; P. Blah verified the quality and thickness of the films with electric transport measurements and x-ray diffractometry.

S1. Supplemental material

S1.1. Pump-probe setup

A simplified schematic of the experimental setup is shown in figure S1.

S1.2. Retrieving conductivity from experiment

The purpose of computing the theoretical transmission amplitude of our device, as detailed in chapter 5, is to extract the conductivity σ of the thin film under the metasurface given the experimental transmission amplitude $t(\omega|R)$. The variable R represents the experimental conditions, such as temperature, field strength, or pump-probe delay. This is achieved with the following approach: We compute the theoretical transmission amplitude for a given σ, which we will denote $h(\omega|\sigma)$, on a grid of candidate values for σ that is sufficiently dense to justify interpolation for intermediate values. We define the distance between the theoretical and experimental transmission amplitudes as

$$\mathcal{E}(R,\sigma) = \int \mathrm{d}\omega \, \left(t(\omega|R) - h(\omega|\sigma)\right)^2 \tag{6.6}$$

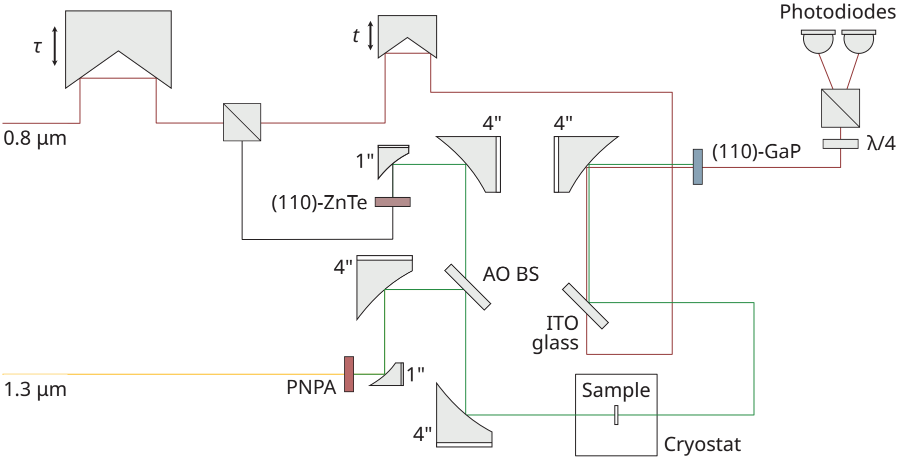

Figure S1: A simplified schematic of the experimental setup. Terahertz (green lines) probe pulses are generated in ZnTe using 100 fs pulses (red line) with a central wavelength of $\lambda = 800$ nm. These pulses are also used for electro-optic sampling of the terahertz pulses in a 200 μm thin (110)-GaP crystal optically contacted to a (100)-GaP substrate. The sampler path and the terahertz path are combined with an indium tin oxide (ITO)-coated glass substrate. Large-amplitude THz pulses used for excitation are generated in an organic crystal, PNPA [27]. Both THz paths include a 4X beam expander consisting of a one-inch and a four-inch off-axis parabolic mirror, to minimize the focal spot size at the sample.

We select σ for a given R based on minimizing this, i.e.

$$\sigma|R = \arg\min_{\sigma} \mathcal{E}(R, \sigma) \tag{6.7}$$

In some experiments, the local conductivity σ within the capacitive gap changes, while the conductivity σ_0 of the rest of the film can be assumed constant. In this case, we use bilevel minimization strategy,

$$\sigma_0 = \arg\min_{\sigma_0} \sum_i \min_{\sigma} \mathcal{E}(R_i, \sigma, \sigma_0) \tag{6.8}$$

which gives the solutions $\sigma|R$ and the σ_0 that minimizes the global error.

S1.3. Keldysh parameter

While our experiments occur not at zero frequency but at 1 THz, Keldysh [28] derived the condition for which the tunneling effect is adiabatic[1], namely when the *Keldysh parameter* γ_K is small. It is defined for an alternating field $E = E_0 \cos(\omega t)$ as

$$\gamma_K = \omega_0 \frac{\sqrt{m_e \Delta}}{e E_0} \tag{6.9}$$

where m_e is the effective mass of the electron, and Δ is the ionization energy, or in the case of band insulators, the band gap. Intuitively, this can be understood as the ratio of the tunneling time to the driving period, measuring how static the effectively oscillating ionization potential is from the point of view of the bound electron [29]. Taking $\Delta = 0.6$ eV from optical spectroscopy of bulk $NdNiO_3$ [14], an effective mass $m = 6m_e$ estimated from the Seebeck coefficient [30], and $E_0 = 4$ MeV/cm we find $\gamma_K = 0.1 \ll 1$. Hence, our experiments are in the adiabatic tunneling regime.

S1.4. Electronic structure

The Ni^{3+} ions are formally $3d^7$ and in a high-spin state with unpaired e_g^2 electrons. In such a system, Hund's coupling J is an attractive force between the e_g^1 spins, while the Coulomb interaction U repels these charges. Mazin et al. [31] argued that J and U are comparable in the rare-earth nickelates, and that this compeition resolves itself as a charge-ordered state where the Ni sites are alternately singly and doubly occupied (Ni^{2+}, Ni^{4+}). It turns out that the charge repulsion U between the e_g is too great to allow such a phase to form, but that a very similar phase is possible if one includes the effects of covalent bonding between Ni and O. The charge-transfer energy (Ni $\longrightarrow$ O) is small or negative in the rare-earth nickelates, such that it is energetically favorable to transfer an electron from oxygen to the nickel sites [32]. Consequently, the proper ground state of Ni is not $3d^7$ as one might initially expect, but rather what is denoted $d^8\underline{L}$ (or $3d^8\,2p^5$), with $\underline{L}$ representing an oxygen hole. This can be thought of as a *self-doped* [11] system, where the oxygen serves as the electron donor rather than e.g. ion substitution. Low-energy minimal models of the electronic structure use as a basis these $d^8\underline{L}$ orbitals resulting from 3 d-2p hybridization. Because they have the same symmetry as the native e_g orbitals, we denote them $\tilde{e}_g$, and the ground state contains a single particle in these orbitals. The renormal-

---

[1] In the sense that the tunneling current depends only on the instantaneous electric field—not, of course, the continuity of eigenstates.

ized repulsion U between the $\tilde{e}_g$ is smaller than that between the e_g, while not significantly affecting the Hund's coupling J [33]. This restores the initial proposal of Mazin et al., but in a slightly different form. The transition can be denoted

$$2\tilde{e}_g^1 \longrightarrow \tilde{e}_g^0 + \tilde{e}_g^2 \quad \text{or} \quad 2\mathrm{d}^8\underline{\mathrm{L}} \longrightarrow \mathrm{d}^8\underline{L}^2 + \mathrm{d}^8 \tag{6.10}$$

Rather than a charge order, here the oxygen hole occupancy (or, the strength of covalency) undergoes an ordering referred to as *bond disproportionation* [11]. This is quite analogous to the phenomenon of charge disproportionation, where the ionic charge is modulated. Structurally, the bond disproportionation corresponds to sites with short Ni-O bonds (SB) and sites with long bonds (LB), known as a breathing distortion. This structural distortion splits the energy of LB and SB by Δ_s, but it does not open any charge gap at the Fermi level and so is not alone responsible for the insulating state. Instead, the insulating state is stabilized roughly when the following condition is satisfied

$$U - 3J < \Delta_s \tag{6.11}$$

Here U is the repulsion between the $\tilde{e}_g$ electrons, and J the Hund's coupling (attractive). Unlike for the ionic e_g states, the covalent $\tilde{e}_g$ states have very weak repulsion $U - 3J$, such that essentially any finite value of Δ_s is sufficient to drive the system insulating [33]. Hence, it can be said that correlations (*viz*. charge repulsions and Hund's coupling of highly covalent wavefunctions) brings the material to the brink of localization, and a lattice instability pushes it over the edge. In an alternative point of view, correlations soften the free energy surface, and the lattice instability forms new local minima [34].

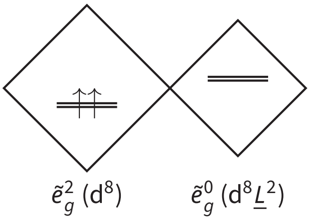

Figure S2: Illustration of site occupations in the insulating state. The diamonds represent the oxygen octahedral cages complexing the Ni sites.

Excited states

The excited states of $NdNiO_3$ in its insulating phase are not fully understood, but two possibilities have been proposed based on the current understanding of the ground state. Ruppen et al. [14] used a combination of optical spectroscopy and dynamical mean-field theory to study the nature of the lowest-energy excitations above the optical gap $\Delta_g \approx 0.6$ eV. They identified two possible scenarios: either the optical gap is essentially a Hubbard gap for the LB sites, or it is an intersite charge-transfer gap between the LB and SB sites.

The Hubbard gap can be explained as follows, based on the DFT + DMFT study by Park et al. [13]: The two sites (SB, LB) in the insulating state are differentiated by occupation (0, 2) as well as spin (0, 1), as illustrated in figure S2. At the SB sites, the e_g electron (considered conceptually prior to covalent bonding) couples strongly to O-2 p orbitals of opposite spin and forms a hybridization gap with a singlet ($S = 0$) ground state, similar to a Kondo insulator, with weak correlations. The LB sites, however, are spin triplets $S = 1$ with strong correlations. Without the breathing distortion, their self-energy resembles that of a Fermi liquid (quadratic in energy). In contrast, with the breathing distortion the self-energy of LB sites looks like that of a Mott-Hubbard insulator (singular at low energy). Park et al. proposed that the metal-insulator transition can be understood as a Mott transition of these LB sites—a “site-selective Mott transition”—opening up a Mott-Hubbard gap Δ_{Mott} in the LB bands. If the corresponding upper Hubbard band is the lowest energy unoccupied state, then $\Delta_g = \Delta_{\text{Mott}}$, and the excited states are essentailly those of a Mott insulator. However, if the upper Hubbard band lies above the unoccupied SB bands, then Δ_g would correspond to an intersite transition (LB $\longrightarrow$ SB), similar to those of a charge-transfer insulator. Experiments indicate that the situation is close to a crossover between these two regimes, if not closer to the charge-transfer regime.

S1.5. X-ray diffraction

X-ray diffraction was used to determine the crystal quality and structure of a blanket thin film of $NdNiO_3$, nominally identical to the film used for the metasurface. A θ–2θ scan around the $(0\,0\,2)$ Bragg peak is shown in figure S3. The presence of a large number of finite-size oscillations signify a high degree of crystallinity. We fit the data to a dynamical diffraction model, obtaining a film thickness of 10.8 nm and a misfit strain $\Delta c / c_{\text{bulk}} = -1.3\,\%$.

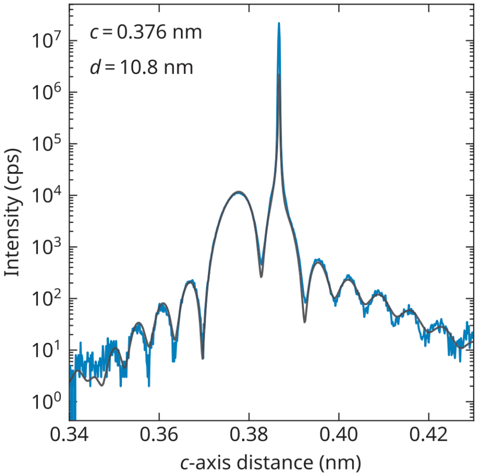

Figure S3: X-ray diffractogram around the $SrTiO_3$ (0 0 2) Bragg peak of the blanket film sample. In black, fit to a model involving a tetragonal $NdNiO_3$ + $SrTiO_3$ stack, with the best-fit parameters noted in the top left for the $NdNiO_3$ film. The x-axis is the Bragg grating constant at the 2θ angle.

S1.6. Pump polarization

The dipole moment of the terahertz resonators is oriented across the capacitive gap, and will not couple to light that is polarized perpendicular to this gap. In figure S4 we verify this by comparing the terahertz dynamics for the two pump polarizations, observing only the fundamental LC-like mode when the pump is aligned with the gap.

S1.7. Temperature and field strength dependence of relaxation

While the pump and the probe interact with the metasurface simultaneously, the probe field undergoes a moduluation $\Delta E(\tau)$ as a function of their delay τ. For any given point t_0 on the probe waveform, this involves a rise and decay time which can depend on the experimental situation, such as temperature T or the strength of the pump field E_0. We study this dependence in figure S5, and find that the rise time τ_0 is independent of both T and E_0, consistent with the understanding that this time is limited by the experimental resolution. The decay time τ_1 however correlates positively with both, amounting to a longer lived state at higher temperatures and field strengths, when considering this early timescale.

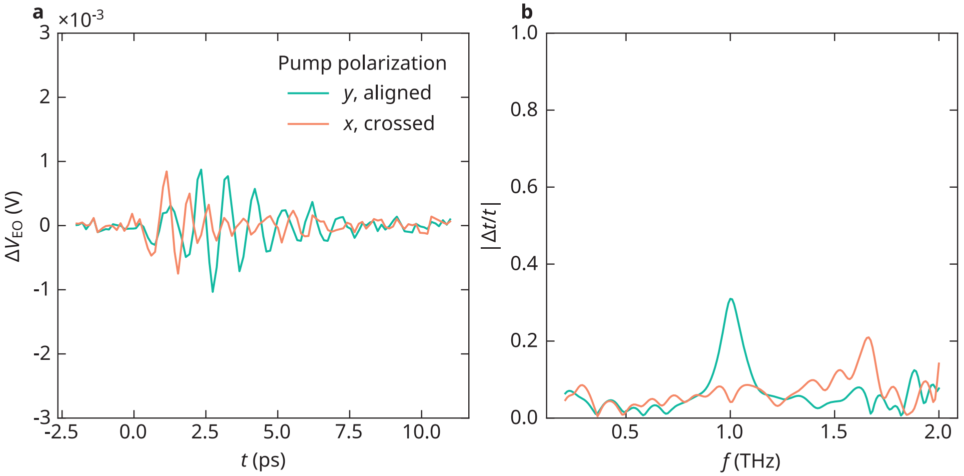

Figure S4: **a**. Comparison of the terahertz dynamics for a pump polarization parallel (aligned) and perpendicular (crossed) to the coplanar capacitor of the terahertz resonators. The signal ΔV_{EO} represents the difference in the electro-optical signal between a measurements with a pump present 7 ps prior to the probe arrival, to one with no pump present. **b**. The magnitude of the relative transmission amplitude, defined as the ratio of the Fourier transform of the differential signal V_{EO}, to the electro-optical signal for a waveform with no pump present. A 1 THz component is only present when the pump is aligned with the capacitive gap of the resonator, activating the field-enhancement with the fundamental LC-like mode.

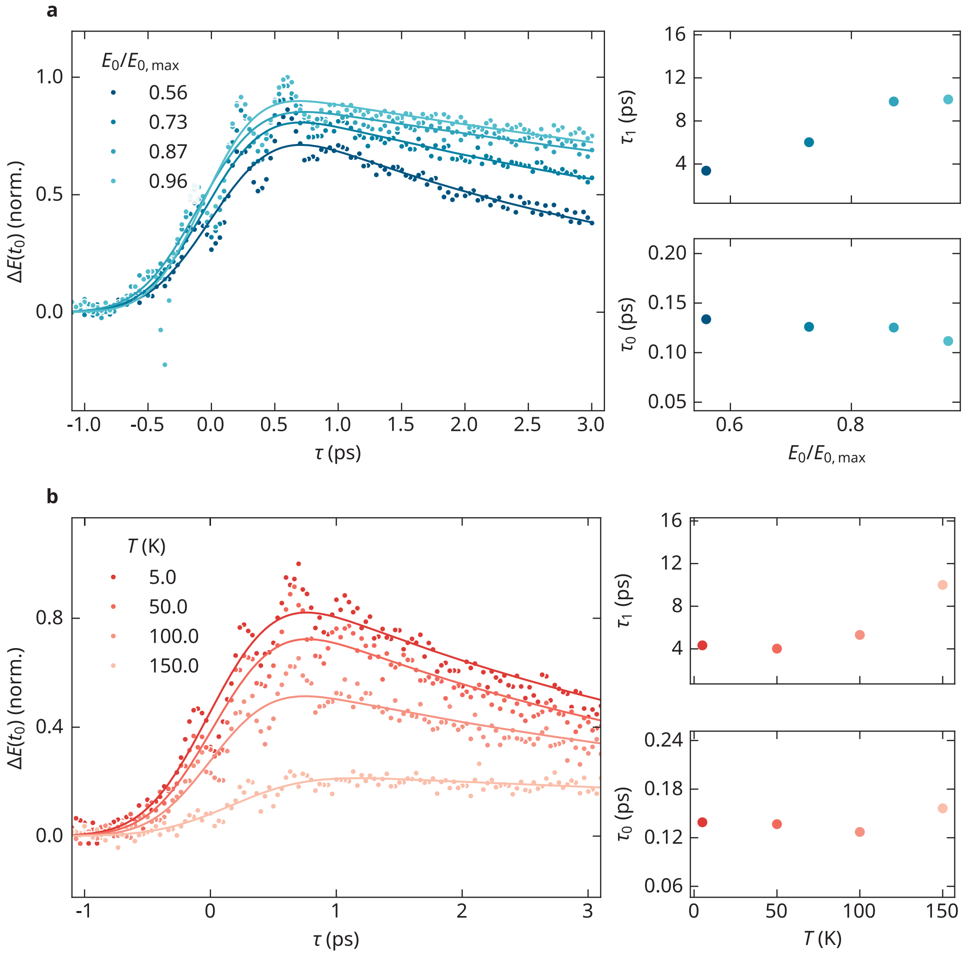

Figure S5: **Pump-probe overlap dynamics** Change in probe electric field ΔE measured at a specific sampling time t_0, as described in section 6.4.1. An exponential rise and decay model, with rise time τ_0 and decay time τ_1 is fit to the data, with point estimates shown to the right. **a**. Dependence on incident pump peak field strength E_0 (relative to the maximum attainable field strength $E_{0,\mathrm{max}} \approx 200\,\mathrm{kV/cm}$). **b**. Dependence on temperature T. The rise time τ_0 is independent of E_0 and T in these measurement ranges, while the decay time τ_1 correlates positively.

References

1. Catalano, S. *et al.* Rare-Earth Nickelates $RNiO_3$: Thin Films and Heterostructures. *Reports on Progress in Physics* **81** (Feb. 2018).
2. Scherwitzl, R. *et al.* Electric-Field Control of the Metal-Insulator Transition in Ultrathin $NdNiO_3$ Films. *Advanced Materials* **22** (2010).
3. Del Valle, J. *et al.* Dynamics of the Electrically Induced Insulator-to-Metal Transition in Rare-Earth Nickelates. *Physical Review B* **104** (2021).
4. Caviglia, A. D. *et al.* Photoinduced Melting of Magnetic Order in the Correlated Electron Insulator $NdNiO_3$. *Physical Review B* **88** (Dec. 2, 2013).
5. Caviglia, A. D. *et al.* Ultrafast Strain Engineering in Complex Oxide Heterostructures. *Physical Review Letters* **108** (Mar. 26, 2012).
6. Landau, L. Zur Theorie Der Energieubertragung. II. *Physikalische Zeitschrift der Sowjetunion* **2** (1932).
7. Zener, C. A Theory of the Electrical Breakdown of Solid Dielectrics. *Proceedings of the Royal Society of London. Series A, Containing Papers of a Mathematical and Physical Character* **145.** JSTOR: 2935519 (1934).
8. Stückelberg, E. C. G. Theorie Der Unelastischen Stösse Zwischen Atomen. *Helvetica Physica Acta* **5** (1932).
9. Oka, T. *et al.* Breakdown of a Mott Insulator: A Nonadiabatic Tunneling Mechanism. *Physical Review Letters* **91** (Aug. 5, 2003).
10. Oka, T. Nonlinear Doublon Production in a Mott Insulator: Landau-Dykhne Method Applied to an Integrable Model. *Physical Review B* **86** (Aug. 27, 2012).
11. Green, R. J. *et al.* Bond Disproportionation and Dynamical Charge Fluctuations in the Perovskite Rare-Earth Nickelates. *Physical Review B* **94** (Nov. 15, 2016).
12. Bisogni, V. *et al.* Ground-State Oxygen Holes and the Metal–Insulator Transition in the Negative Charge-Transfer Rare-Earth Nickelates. *Nature Communications* **7** (Oct. 11, 2016).
13. Park, H. *et al.* Site-Selective Mott Transition in Rare-Earth-Element Nickelates. *Physical Review Letters* **109** (Oct. 9, 2012).
14. Ruppen, J. *et al.* Optical Spectroscopy and the Nature of the Insulating State of Rare-Earth Nickelates. *Physical Review B* **92** (Oct. 27, 2015).
15. Mattoni, G. *et al.* Striped Nanoscale Phase Separation at the Metal–Insulator Transition of Heteroepitaxial Nickelates. *Nature Communications* **7** (Nov. 2, 2016).
16. Simmons, J. G. Poole-Frenkel Effect and Schottky Effect in Metal-Insulator-Metal Systems. *Physical Review* **155** (Mar. 15, 1967).

17. Barbeta, V. B. *et al.* Metal-Insulator Transition in $Nd_{1-x}Eu_xNiO_3$ Probed by Specific Heat and Anelastic Measurements. *Journal of Applied Physics* **109** (Mar. 24, 2011).

18. Liu, M. *et al.* Terahertz-Field-Induced Insulator-to-Metal Transition in Vanadium Dioxide Metamaterial. *Nature* **487** (July 2012).

19. Katsufuji, T. *et al.* Optical Spectroscopy of the Metal-Insulator Transition in $NdNiO_3$. *Physical Review B* **51** (Feb. 15, 1995).

20. Takamura, N. *et al.* Efficient Mott Insulator-Metal Transition by an Intense Terahertz Electric Field Pulse via Quantum Tunneling. *Physical Review B* **107** (Feb. 27, 2023).

21. AlShafey, A. *et al.* Extracting Correlation Length in Mott Insulators by Strong-Field Driving. *JOSA B* **41** (June 1, 2024).

22. Sensarma, R. *et al.* Lifetime of Double Occupancies in the Fermi-Hubbard Model. *Physical Review B* **82** (Dec. 3, 2010).

23. Strohmaier, N. *et al.* Observation of Elastic Doublon Decay in the Fermi-Hubbard Model. *Physical Review Letters* **104** (Feb. 22, 2010).

24. Eckstein, M. *et al.* Photoinduced States in a Mott Insulator. *Physical Review Letters* **110** (Mar. 18, 2013).

25. Golež, D. *et al.* Dynamics of Photodoped Charge Transfer Insulators. *Physical Review B* **100** (July 17, 2019).

26. Plonka, A. Chapter 3. Dispersive Kinetics in Condensed Phases. *Annual Reports Section 'C' (Physical Chemistry)* **85** (Jan. 1, 1988).

27. Rader, C. *et al.* A New Standard in High-Field Terahertz Generation: The Organic Nonlinear Optical Crystal PNPA. *ACS Photonics* **9** (Nov. 16, 2022).

28. Keldysh, L. V. Ionization in the Field of a Strong Electromagnetic Wave. *Soviet Physics, JETP* **20** (1964).

29. Topcu, T. *et al.* Dichotomy between Tunneling and Multiphoton Ionization in Atomic Photoionization: Keldysh Parameter γ versus Scaled Frequency Ω. *Physical Review A* **86** (Nov. 9, 2012).

30. Granados, X. *et al.* Metallic State and the Metal-Insulator Transition of $NdNiO_3$. *Physical Review B* **48** (Oct. 15, 1993).

31. Mazin, I. I. *et al.* Charge Ordering as Alternative to Jahn-Teller Distortion. *Physical Review Letters* **98** (Apr. 26, 2007).

32. Zaanen, J. *et al.* Band Gaps and Electronic Structure of Transition-Metal Compounds. *Physical Review Letters* **55** (July 22, 1985).

33. Seth, P. *et al.* Renormalization of Effective Interactions in a Negative Charge Transfer Insulator. *Physical Review B* **96** (Nov. 21, 2017).

34. Georgescu, A. B. *et al.* Quantifying the Role of the Lattice in Metal–Insulator Phase Transitions. *Communications Physics* **5** (1 May 31, 2022).

7

Terahertz emission from spin currents in platinum

In bilayers of ferromagnets and heavy metals, which form so-called spintronic emitters, the phenomena of ultrafast demagnetization and the inverse spin Hall effect (ISHE) conspire to yield remarkably efficient emission of electric pulses in the THz band. Light-induced demagnetization of the ferromagnet launches a pulse of spin current into the heavy metal, which bifurcates into a radiative charge transient due to the ISHE. The influence of temperature on this combined effect should depend on the magnetic phase diagram and the microscopic origin of spin Hall conductivity, but its impact remains to be clarified. Here, we experimentally study the temperature dependence of an archetypal spintronic emitter, the Co/Pt bilayer, using electro-optic sampling of the emitted THz pulses in the time domain. The emission amplitude diminishes with decreasing temperature, consistent with an inverse spin Hall effect in platinum of predominantly intrinsic origin.

This chapter is based on Matthiesen et al. [1], “Temperature dependent inverse spin Hall effect in Co/Pt spintronic emitters”.

Femtosecond laser excitation of ferromagnet/non-magnetic heavy metal bilayers produces surprisingly intense emission of THz radiation, despite their nanometric thickness [2–4]. This effect consists of (i) the production of a transient spin current, (ii) the conversion of the spin current into a charge current, and (iii) the emission of broadband light from the charge dynamics. (i) The production of a spin current $\mathbf{j}_\mathrm{s}(t)$ occurs in metallic ferromagnets such as Co because hot electron populations produced by the high-energy excitation have spin-dependent transport properties, such as mobility and lifetime [5–8]. (ii) The transient spin current is consequently converted to a charge current $\mathbf{j}_c$ through the inverse spin Hall effect (ISHE): In the heavy metal, hot electrons of opposite spin undergo spatial deflection in opposite directions at a mean tangent $\theta_\mathrm{sH} \equiv \rho_\mathrm{sH}/\rho$, called the spin Hall angle, with ρ_sH the spin Hall resistivity of the heavy metal and ρ its longitudinal resistivity[1]. The heavy metal thereby acts as a spin-charge transducer, converting the injected pulsed spin current $\mathbf{j}_\mathrm{s}$ into a charge current $\mathbf{j}_\mathrm{c} = \theta_\mathrm{sH}(\mathbf{j}_\mathrm{s} \times \hat{\mathbf{m}})$, with $\hat{\mathbf{m}} = \mathbf{M}/M$ the magnetization direction. (iii) Finally, the transient charge current $\mathbf{j}_\mathrm{c}$ emits an electric pulse $E(t)$ polarized perpendicularly to the initial in-plane magnetization of the sample, acting as a source in the wave equation,

$$\left(\nabla^2 - \frac{1}{c^2}\partial_t^2\right)\mathbf{E}(\mathbf{r},t) = \mu_0 \frac{\partial \mathbf{j}_c(\mathbf{r},t)}{\partial t} \tag{7.1}$$

In terms of the spin current density, the emission amplitude reads in the spectral domain (see section 7.2.1)

$$E_\mathrm{THz}(\omega) = \left(\frac{\rho_\mathrm{FM|HM}}{\rho_\mathrm{HM} d}\right) \rho_\mathrm{sH} j_\mathrm{s}(\omega) \tag{7.2}$$

The spectral content is, therefore, dictated by that of the spin current. Due to the short timescale of demagnetization (about 100 fs), this extends into the terahertz range, with demonstrations of spectral content spanning tens of THz when using very short excitation pulses [3].

7.1. Temperature dependence

Whereas the bracketed factor in equation (7.2), which includes the resistivity of the complete bilayer of thickness d, is nearly temperature independent in a bilayer of two similar metals, the THz emission amplitude may inherit a substantial temperature dependence

---

[1] Common convention uses a negative sign, omitted in this work.

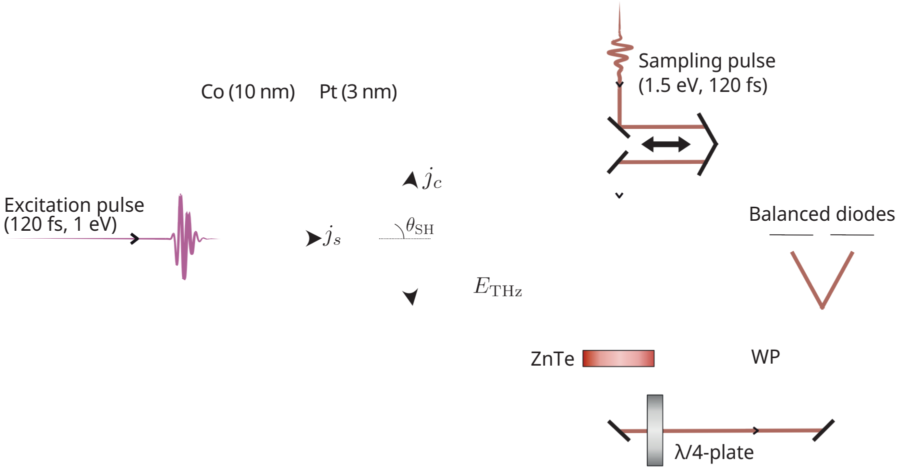

Figure 7.1: Experimental scheme, consisting of two beams, one for excitation ($\lambda_0 = 1.2\,\mu$m) of the sample and one for sampling ($\lambda_0 = 0.8\,\mu$m) of the emitted THz pulse. The sampling is based on the Pockels effect in a (110)-oriented ZnTe, wherein the THz pulse modulates the polarization state of the Co-propagating sampling pulse. The change in the polarization state is detected by measuring the relative intensity of the two transverse sampler field components: the components are spatially separated with a Wollaston prism (WP) and sent onto a pair of balanced photodiodes (BPD). A quarter-wave plate (QWP) equalizes their intensity without a THz pulse. The spectrometer is sensitive up to about 2.7 THz (370 fs).

from the remaining two quantities: the laser-induced pulsed spin current density j_s supplied by the ferromagnet, and the spin Hall resistivity [9] $\rho_{\mathrm{sH}} = \theta_{\mathrm{sH}}\rho$ of the heavy metal.

The temperature dependence of ρ_{sH} (or θ_{sH}) differs depending on the microscopic origin of the ISHE. The particular dependence can be ascribed either to spin-dependent scattering events (extrinsic origin) or to a geometric correction to the electron velocity arising from spin Berry curvature (intrinsic origin) [10, 11]. The temperature dependence of the spin current density j_s on the other hand, is set by the degree of demagnetization $\Delta M / M_0$ of the ferromagnet.

Previous studies report that the amplitude and timescale of demagnetization may depend on temperature when the ferromagnet is in proximity to a magnetic phase transition [12–16]. In this work, we use cobalt as a spin source because of its large Curie temperature ($T_\mathrm{C} = 1388$ K in bulk [17]), meaning that below room temperature the system is far from any magnetic transition. We show that the thermal variation in this case is not set by the spin source (Co), which exhibits temperature-independent magnetization and demagnetization dynamics, but instead by the spin Hall resistivity of our chosen transduction layer (Pt).

7.2. Terahertz emission spectroscopy

A Co/Pt (10 nm/3 nm) bilayer was deposited by dc magnetron sputtering at room temperature onto a glass substrate that is transparent to THz radiation. A small Ar deposition pressure (3 mTorr) gives to a low degree of interface roughness [18], and a Pt residual resistivity ($T \longrightarrow 0$) of $\rho_0 = 29.4\,\mu\Omega$ cm.

Figure 7.1 depicts the experimental THz time-domain emission spectroscopy setup. Subpicosecond laser pulses (central wavelength 1.2 μm, repetition rate $f_{\text{rep}} = 1$ kHz) are used to demagnetize the Co layer. The emitted pulse is collected by a parabolic mirror, focused, and detected with electro-optic sampling in a 0.5 mm thick ZnTe crystal cut along the (110) crystallographic direction. The peak amplitude (E_{p}) of the emitted pulse was measured in a temperature range of 10 − 280 K, as shown in figure 7.2a. We note that the pulse shape is constant with temperature, making E_{p} an unambiguous measure of the emission amplitude, and its square is proportional to the pulse energy. A complete reversal of the pulse polarization by switching the Co magnetization using an external magnet, shown in figure 7.2b, demonstrates the magnetic origin of this emission signal. We observe a reduction of emission amplitude as the sample is cooled, eventually reaching a plateau at roughly 70 K. This decrease in E_{p} is at striking variance with the temperature behavior of THz emitters based on optical rectification, such as ZnTe and LiNbO$_3$, wherein lower temperatures reduce phonon reabsorption and enhance the emission amplitude [19, 20]. The same is true of photoswitches made of InSb or GaAs, for which higher mobility at lower temperatures also contributes to enhanced THz emission [21].

7.2.1. Emission amplitude

Following the derivation of Seifert et al. [3], the THz emission amplitude following an excited spin current density j_{s} within the Co/Pt stack can be shown to be

$$E_{\text{THz}}(\omega) = \frac{j_{\text{s}}\rho_{\text{sH}}/\rho_{\text{Pt}}}{(1+n_{\text{sub}})/Z_0 + \int_0^d \mathrm{d}x\,\sigma(x,\omega)} \tag{7.3}$$

with n_{sub} the substrate index of refraction and Z_0 the vacuum impedance. Since the bilayer conductance $\int_0^d \mathrm{d}x\,\sigma = d\sigma_{\text{Co|Pt}}$ is much larger than the shunt conductance (1 +

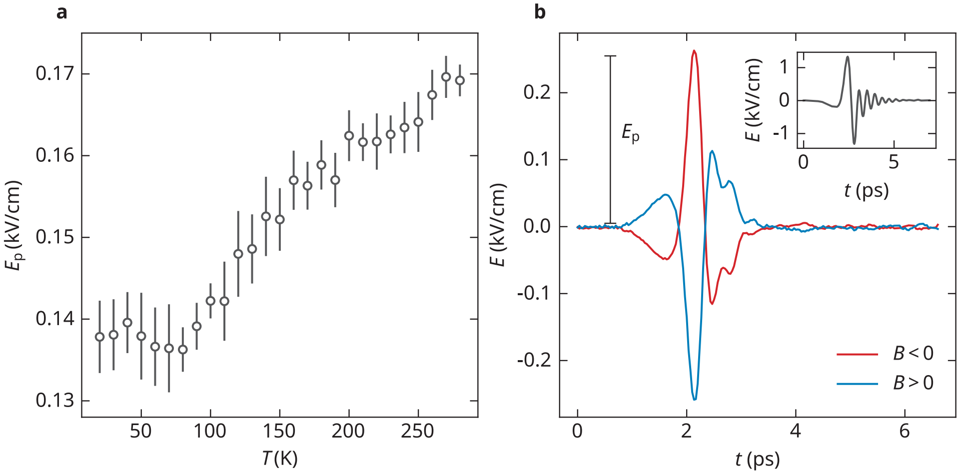

Figure 7.2: **a**. Temperature (T) dependence of the peak THz emission amplitude (E_p). **b**. Time-domain emitted waveforms after magnetizing the sample with opposite magnetic field polarity. For comparison with a well-known THz emitter, the inset shows the waveform emitted from a ZnTe crystal.

$n_{sub})/Z_0$, the latter can be neglected and one obtains

$$E_{THz} \approx \left(\frac{\rho_{Co|Pt}}{d\rho_{Pt}}\right) j_s \rho_{sH} \tag{7.4}$$

While both ρ_{Pt} and ρ_{Co} play a role in the coupling of currents in the bilayer to radiation, it is important to note that only ρ_{Pt} plays a role in the spin-charge conversion process, which takes place in platinum. Moreover, our measurements reveal that the ratio $\rho_{Co|Pt}/\rho_{Pt}$ is nearly temperature independent (see figure 7.5).

7.3. Magneto-optics

To probe whether the observed temperature dependence of E_p is due to variations in the excited spin current density j_s, we measure the temperature dependence of the magneto-optical Faraday effect, in which the presence of magnetization causes a rotation (θ_F) of the probe polarization (figure 7.3a) proportional to the total magnetization. We observe the magnetization is independent of temperature in the $10 - 280\,$K range. The laser-induced change in rotation ($\Delta\theta_F/\theta_F$) arising from demagnetization is presented in figure 7.3b. For the various initial sample temperatures, we extract the degree of demagnetization. We see no significant temperature dependence of the demagnetization amplitude. These observations point to ρ_{sH}, instead of j_s, as the origin of the temperature-dependent THz emission amplitude.

The spin Hall resistivity $\rho_{\mathrm{sH}} = \theta_{\mathrm{sH}}\rho_{\mathrm{Pt}}$ is a measure of the magnitude of the ISHE for a system with longitudinal resistivity ρ_{Pt}. It is, therefore, necessary to consider the temperature dependence of the Pt resistivity. For this, we deposit a 3 nm Pt film on a glass substrate separately and measure the longitudinal resistivity as a function of temperature. These measurements are performed in a four-point van der Pauw geometry, sourcing a low frequency (17 Hz) 100 μA current and measuring the resulting voltage drop with a lock-in amplifier. We note that ρ_{sH} and ρ_{Pt} both concern the static limit ($\omega \to 0$) (see section S2), whereas the currents excited in the sample are transient. However, since interaction and scattering times are much shorter than the current dynamics $\omega/2\pi \approx 1$ THz, a quasi-static regime can be assumed (see section S2). The measured resistivity $\rho_{\mathrm{Pt}}(T)$ of the bare Pt film decreases linearly from room temperature down to 30 K, below which a slight recovery occurs (figure 7.4b). Additionally, we measure the temperature dependence of the resistivity of the Co/Pt bilayer and note that the ratio $\rho_{\mathrm{Co|Pt}}/\rho_{\mathrm{Pt}}$ is approximately constant to within 4% across the temperature range.

7

7.4. Causes of spin Hall resistivity

It is clear that ρ_{Pt} plays a central role in the temperature dependence of E_{p}, a connection that requires consideration of the microscopic origin of spin Hall resistivity, $\rho_{\mathrm{sH}} = \sigma_{\mathrm{sH}}\rho_{\mathrm{Pt}}^2$. The residual resistivity of the bare Pt film is $\rho_{\mathrm{Pt},0} = 29.4\,\mu\Omega\,\mathrm{cm}$, placing it at the boundary of two spin Hall regimes: the dominant contribution to the spin Hall resistivity arises, in one case, intrinsically from the band structure; in the other, from extrinsic skew (Mott) impurity scattering [22]. The intrinsic effect occurs due to the mixing of spin states near lifted degeneracies of the spin-orbit coupled band structure. This results in a finite spin Berry curvature $\boldsymbol{\Omega}_{\sigma,\mathbf{k}}$ that modifies the semiclassical electron velocity by an amount $-\mathbf{k} \times \boldsymbol{\Omega}_{\sigma,\mathbf{k}}$ [23]. Thus, the accumulation of transverse velocity takes place during propagation rather than during scattering events. Consequently, the intrinsic spin Hall conductivity $\sigma_{\mathrm{sH}}^{\mathrm{int}}$ does not depend on the scattering rate, so that $\rho_{\mathrm{SH}}^{\mathrm{int}} = \sigma_{\mathrm{sH}}^{\mathrm{int}}\rho_{\mathrm{Pt}}^2$. On the other hand, skew scattering is a relativistic effect in which electrons spin-orbit coupled to an impurity experience an effective magnetic field gradient in the scattering plane. This results in a net force toward, or away, from the scattering center depending on its spin angular momentum (figure 7.4a) [10]. The skew scattering contribution to the spin Hall

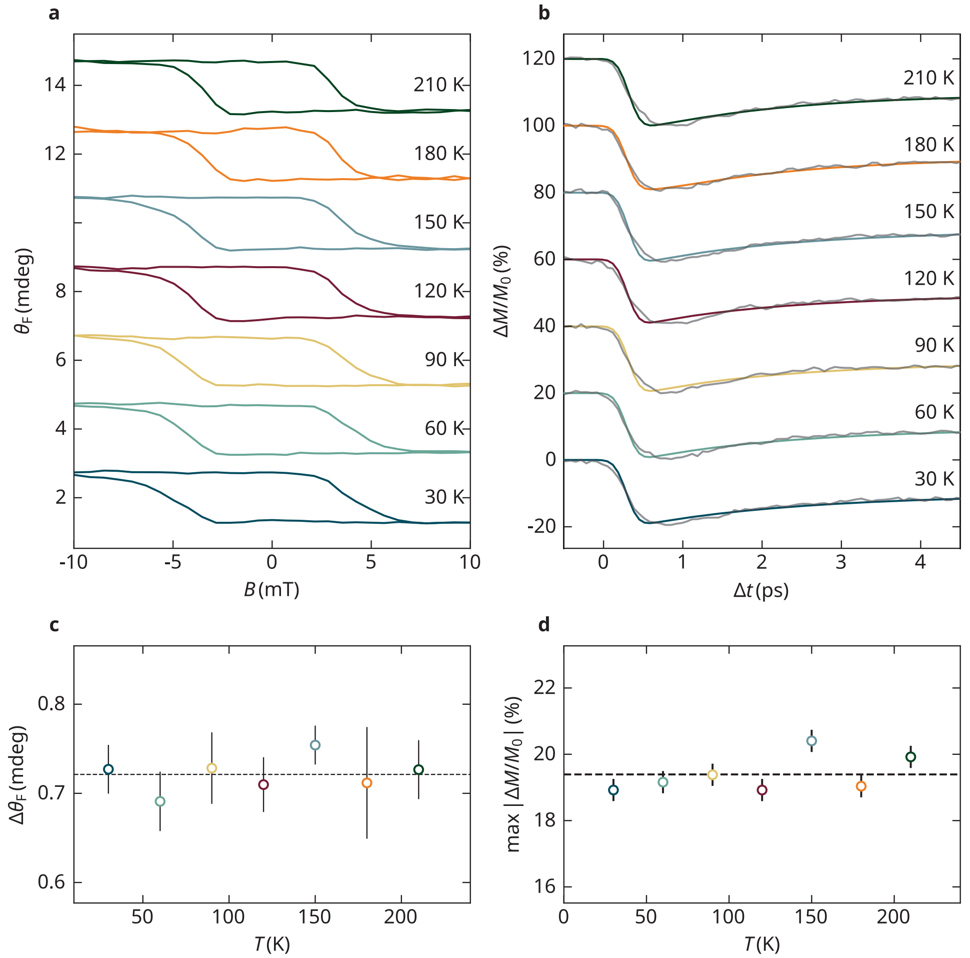

Figure 7.3: **a**. Hysteresis curves of the Faraday rotation θ_F are presented for various temperatures of the sample (top panel). The total rotation $\Delta\theta_F = \frac{1}{2}(\theta_F^+ - \theta_F^-)$ shown for each measured temperature (bottom panel). **b**. Laser-induced dynamical changes to the magnetization, probed via the Faraday rotation, is shown for various temperatures (top panel). The peak demagnetization is extracted and plotted against T (bottom panel).

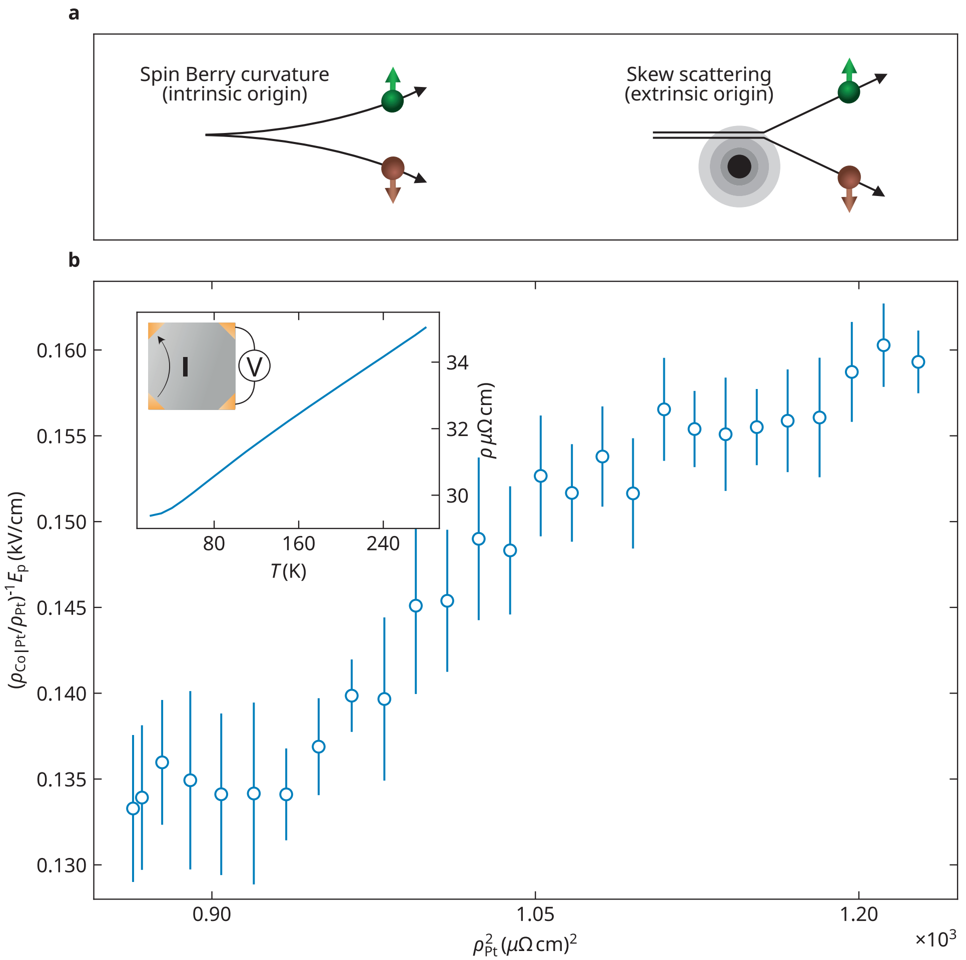

Figure 7.4: **a**. An illustration of the leading intrinsic and extrinsic contributions to the ISHE in Pt. **b**. A measure of the spin Hall resistivity, $\rho_{\mathrm{sH}} \propto (\rho_{\mathrm{Co|Pt}}/\rho_{\mathrm{Pt}})^{-1}E_{\mathrm{p}}$, as a function of the squared resistivity ρ_{Pt}^2. The inset displays the temperature dependence of the resistivity ρ_{Pt}, measured in a 3 nm thick Pt film with a four-point van der Pauw scheme.

conductivity $\sigma_{\mathrm{sH}}^{\mathrm{ss}} = \alpha_{\mathrm{ss}}/\rho_{\mathrm{Pt},0}$ relates inversely to the residual resistivity, with α_{ss} the skew scattering angle. Furthermore, since skew scattering is impurity dependent, it is $\rho_{\mathrm{Pt},0}$, not ρ_{Pt}, that is the relevant resistivity. The spin Hall resistivity contribution therefore takes the form $\rho_{\mathrm{sH}}^{\mathrm{ss}} = \sigma_{\mathrm{sH}}^{\mathrm{ss}}\rho_{\mathrm{Pt},0}^2 = \alpha_{\mathrm{ss}}\rho_{\mathrm{Pt},0}$. From the above considerations, a temperature scaling of the total spin Hall resistivity has been motivated experimentally [24] and theoretically [25] to take the form

$$\rho_{\mathrm{sH}}(T) = \alpha_{\mathrm{ss}}\rho_{\mathrm{Pt},0} + \sigma_{\mathrm{sH}}^{\mathrm{int}}\rho_{\mathrm{Pt}}^2(T) \tag{7.5}$$

In figure 7.4 we display the quantity $(\rho_{\mathrm{Co|Pt}}/\rho_{\mathrm{Pt}})^{-1}E_{\mathrm{p}} \propto \rho_{\mathrm{sH}}$ as a function of ρ_{Pt}^2. Comparing with equation (7.5) it is clear that the observed temperature dependence follows from a substantial intrinsic contribution to the spin Hall effect. A spin Hall effect of predominantly intrinsic origin is consistently observed for Pt in experiment [9, 26] and is expected from relativistic band structure calculations [27].

7.5. Low-temperature anomaly

While an approximately ρ_{Pt}^2-linear correlation is maintained across most of the temperature range, an unexpected amplitude recovery occurs below $T \approx 70$ K. This is at variance with equation (7.5) and warrants discussion. One possible explanation is a rise in the spin current relaxation length at low temperatures. The decay of j_{s} along the thickness of Pt yields a smaller effective spin current density $j_{\mathrm{s}}^* \leqslant j_{\mathrm{s}}$ undergoing spin-charge conversion, resulting in reduced emission. However, assuming this relaxation length is close to the spin diffusion length ($\lambda_{\mathrm{sd}} \approx 8$ nm) [28], it is significantly longer than the thickness of our Pt film ($d_{\mathrm{Pt}} = 3$ nm). As such, variations in λ_{sd} would have a negligible impact on E_{p} (see section S1). A more likely scenario is that the intrinsic spin Hall conductivity $\sigma_{\mathrm{sH}}^{\mathrm{int}}$ has a temperature dependence, as predicted by Guo et al. [27] using first-principles relativistic band calculations for Pt. In this scenario, the Berry curvature results from the competition of two bands with contributions of opposite sign, one of which is unoccupied at $T = 0$. When the temperature increases, the population of this band begins to reduce the net Berry curvature, thus decreasing the spin Hall conductivity. A similar temperature-dependent competition between opposing sources of emergent magnetic field has been proposed recently for ultrathin SrRuO$_3$ [29].

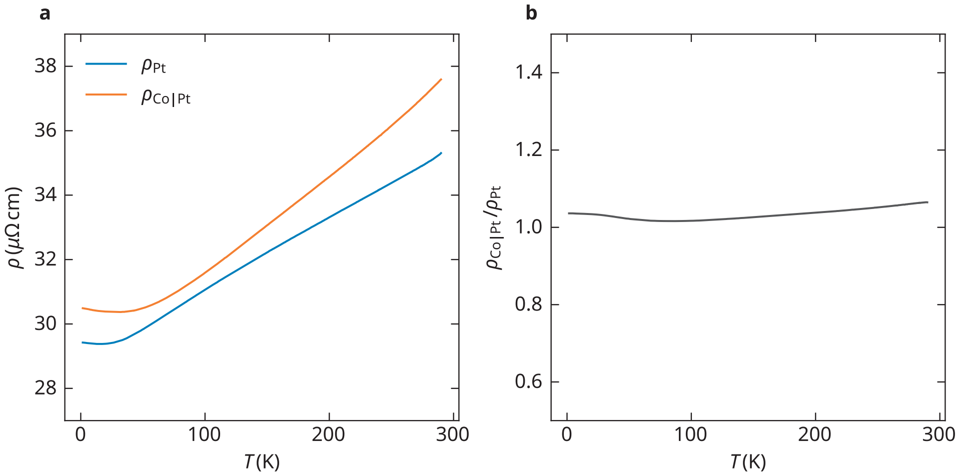

Figure 7.5: **a**. The measured resistivities of the sample (Co/Pt, 10/3 nm) and a platinum-only film of thickness 3 nm. **b**. The ratio of the two resistivities shows constancy within 5% across the measured temperature range.

7.6. Conclusion

Using a combination of time-domain THz emission spectroscopy, transport measurements, and magneto-optics in a cryogenic setup, we demonstrate that the temperature response of the Co/Pt spintronic emitter is dictated by the spin Hall physics of Pt, the intrinsic origin of which leads to a proportionality between the emission amplitude and the squared resistivity of Pt. Our results highlight the relevance of cryogenic THz emission spectroscopy to the study of spin-charge conversion processes in spintronic emitters.

7.7. Contributions

M. Matthiesen built the experimental setup, performed the measurements, the analysis; D. Afanasiev and J. R. Hortensius contributed to the understanding and the writing of the manuscript associated with this chapter; R. Medapalli deposited the metallic bilayers; T. C. van Thiel did the transport measurements.

7.8. Data availability

The data recorded in the experiments of this chapter and the code used for the analysis are accessible at the DOI 10.5281/zenodo.13205361.

S1. Neglecting spin relaxation

The ultrafast spin current has a relaxation length λ_{rel}, which gives an effective spin current j_{s}^{*} smaller than the optically injected spin current j_{s}. In the main text we assume that even if λ_{rel} does have some temperature dependence, the effect on E_{p} will be negligible. The spin current relaxation length has been shown to be close to the spin diffusion length λ_{sd} of d.c. transport [30]. Following *Niimi et al.* [31], this results in an effective spin Hall resistivity ρ_{sH}^{*} which is a nonlinear function of the relative film thickness, $d_{\mathrm{Pt}}/\lambda_{\mathrm{sd}}$.

As is well known, the determination of λ_{sd} is notoriously difficult and the reported values are highly scattered. However, much progress have been made in the past few years. Using a self-consistent method, *Tao et al.* determine a spin diffusion length of $\lambda_{\mathrm{sd}} = 8.0\,\mathrm{nm}$ for a platinum system close to ours in terms of purity [28]. Since our platinum film is relatively thin ($d_{\mathrm{Pt}} = 3\,\mathrm{nm}$), the ratio $\rho_{\mathrm{sH}}^{*}/\rho_{\mathrm{sH}}$ is approximately constant,

$$\frac{\partial_{\lambda_{\mathrm{sd}}}(\rho_{\mathrm{sH}}^{*}/\rho_{\mathrm{sH}})}{\rho_{\mathrm{sH}}^{*}/\rho_{\mathrm{sH}}} = 0.3\% \qquad (\lambda_{\mathrm{sd}} = 8\,\mathrm{nm}) \tag{7.6}$$

Even if we assume a significantly shorter diffusion length, say $\lambda_{\mathrm{sd}} = 4\,\mathrm{nm}$, the same expression gives 2.3%. Thus we can neglect the effect of changes in λ_{sd} on E_{p} for our sample.

S2. Validity of the static limit

Whereas quantities such as ρ_{sH} and θ_{sH} are defined in the $\omega \to 0$ in the Kubo formalism, and measurements of them are performed in dc (or low frequency) transport schemes, the excited spin and charge currents in Co/Pt have lifetimes on the order of picoseconds. We use no generalizations of these parameters, but assume a quasi-static regime where the equilibrium quantities are still appropriate.

Generalizations of the spin Hall quantities to finite frequencies are model dependent, but generally involve corrections on the order $\omega\tau$ with τ some interaction or scattering time. In the Rashba model, the relevant interaction time is

$$\tau_{\mathrm{SO}} \propto \hbar/\sqrt{E_{\mathrm{SO}} E_{\mathrm{F}}} \tag{7.7}$$

with E_{SO} the spin-orbit induced band splitting and E_{F} the Fermi energy [32]. We estimate the Fermi energy (assuming a free electron gas) to be

$$E_{\mathrm{F}} = (\hbar^2/2m_{\mathrm{e}})/(3\pi^2(-1/eR_{\mathrm{H}}))^{2/3} = 14.5\,\mathrm{eV} \tag{7.8}$$

with $R_{\mathrm{H}} = -25.5\,\mathrm{p\Omega\,m/T}$ the ordinary Hall coefficient obtained from transport measurements. We take the spin-orbit splitting energy $E_{\mathrm{SO}} = 0.93\,\mathrm{eV}$ from the relativistic band structure calculations of Guo et al [27]. As a characteristic frequency of our current transients we take $\omega/2\pi = 1\,\mathrm{THz}$. Then we obtain $\omega\tau_{\mathrm{SO}} \approx 10^{-3} \ll 1$. Other relevant scattering times are the momentum relaxation time τ_p and the spin diffusion time τ_{sd}. The former is approximately $\tau_p = -R_{\mathrm{H}} m_{\mathrm{e}}/\rho e = 0.5\,\mathrm{fs}$ so that corrections are of order $\omega\tau_p \approx 10^{-3} \ll 1$. The spin diffusion time, assuming Dyakonov-Perel spin relaxation, is given by $\tau_{\mathrm{s}} = 1/(\Omega_{\mathrm{SO}}^2 \tau_p)$ [33]. Taking $\Omega_{\mathrm{SO}} = E_{\mathrm{SO}}/\hbar$, we obtain

$$\omega\tau_{\mathrm{sd}} \approx 10^{-2} \ll 1 \tag{7.9}$$

This confirms the validity of the quasistatic limit.

References

1. Matthiesen, M. *et al.* Temperature Dependent Inverse Spin Hall Effect in Co/Pt Spintronic Emitters. *Applied Physics Letters* **116** (May 29, 2020).
2. Kampfrath, T. *et al.* Terahertz Spin Current Pulses Controlled by Magnetic Heterostructures. *Nature Nanotechnology* **8** (Apr. 2013).
3. Seifert, T. *et al.* Efficient Metallic Spintronic Emitters of Ultrabroadband Terahertz Radiation. *Nature Photonics* **10** (7 July 2016).
4. Huisman, T. J. *et al.* Femtosecond Control of Electric Currents in Metallic Ferromagnetic Heterostructures. *Nature Nanotechnology* **11** (5 May 2016).
5. Battiato, M. *et al.* Superdiffusive Spin Transport as a Mechanism of Ultrafast Demagnetization. *Physical Review Letters* **105** (July 9, 2010).
6. Eschenlohr, A. *et al.* Ultrafast Spin Transport as Key to Femtosecond Demagnetization. *Nature Materials* **12** (4 Apr. 2013).
7. Turgut, E. *et al.* Controlling the Competition between Optically Induced Ultrafast Spin-Flip Scattering and Spin Transport in Magnetic Multilayers. *Physical Review Letters* **110** (May 7, 2013).
8. Melnikov, A. *et al.* Ultrafast Transport of Laser-Excited Spin-Polarized Carriers in Au/Fe/MgO(001). *Physical Review Letters* **107** (Aug. 12, 2011).
9. Isasa, M. *et al.* Temperature Dependence of Spin Diffusion Length and Spin Hall Angle in Au and Pt. *Physical Review B* **91** (Jan. 5, 2015).
10. Hoffmann, A. Spin Hall Effects in Metals. *IEEE Transactions on Magnetics* **49** (Oct. 2013).
11. Nagaosa, N. *et al.* Anomalous Hall Effect. *Reviews of Modern Physics* **82** (May 13, 2010).
12. Seifert, T. *et al.* Terahertz Spin Currents and Inverse Spin Hall Effect in Thin-Film Heterostructures Containing Complex Magnetic Compounds. *SPIN* **07** (July 3, 2017).
13. Roth, T. *et al.* Temperature Dependence of Laser-Induced Demagnetization in Ni: A Key for Identifying the Underlying Mechanism. *Physical Review X* **2** (May 16, 2012).
14. Fix, M. *et al.* Thermomagnetic Control of Spintronic THz Emission Enabled by Ferrimagnets. *Applied Physics Letters* **116** (Jan. 2, 2020).
15. Huisman, T. J. *et al.* Spin-Photo-Currents Generated by Femtosecond Laser Pulses in a Ferrimagnetic GdFeCo/Pt Bilayer. *Applied Physics Letters* **110** (Feb. 13, 2017).
16. Mueller, B. Y. *et al.* Thermodynamic μT Model of Ultrafast Magnetization Dynamics. *Physical Review B* **90** (Oct. 16, 2014).

17. Mohn, P. *et al.* The Curie Temperature of the Ferromagnetic Transition Metals and Their Compounds. *Journal of Physics F: Metal Physics* **17** (Dec. 1987).
18. Li, G. *et al.* THz Emission from Co/Pt Bilayers with Varied Roughness, Crystal Structure, and Interface Intermixing. *Physical Review Materials* **3** (Aug. 19, 2019).
19. Schall, M. *et al.* Freeze-out of Difference-Phonon Modes in ZnTe and Its Application in Detection of THz Pulses. *Applied Physics Letters* **77** (Oct. 24, 2000).
20. Wu, X. *et al.* Temperature Dependent Refractive Index and Absorption Coefficient of Congruent Lithium Niobate Crystals in the Terahertz Range. *Optics Express* **23** (Nov. 16, 2015).
21. Hu, B. B. *et al.* Temperature Dependence of Femtosecond Electromagnetic Radiation from Semiconductor Surfaces. *Applied Physics Letters* **57** (Dec. 17, 1990).
22. Onoda, S. *et al.* Quantum Transport Theory of Anomalous Electric, Thermoelectric, and Thermal Hall Effects in Ferromagnets. *Physical Review B* **77** (Apr. 2, 2008).
23. Xiao, D. *et al.* Berry Phase Effects on Electronic Properties. *Reviews of Modern Physics* **82** (July 6, 2010).
24. Tian, Y. *et al.* Proper Scaling of the Anomalous Hall Effect. *Physical Review Letters* **103** (Aug. 21, 2009).
25. Shitade, A. *et al.* Anomalous Hall Effect in Ferromagnetic Metals: Role of Phonons at Finite Temperature. *Journal of the Physical Society of Japan* **81** (July 18, 2012).
26. Zhu, L. *et al.* Variation of the Giant Intrinsic Spin Hall Conductivity of Pt with Carrier Lifetime. *Science Advances* **5** (July 1, 2019).
27. Guo, G. Y. *et al.* Intrinsic Spin Hall Effect in Platinum: First-Principles Calculations. *Physical Review Letters* **100** (Mar. 3, 2008).
28. Tao, X. *et al.* Self-Consistent Determination of Spin Hall Angle and Spin Diffusion Length in Pt and Pd: The Role of the Interface Spin Loss. *Science Advances* **4** (June 1, 2018).
29. Groenendijk, D. J. *et al.* Berry Phase Engineering at Oxide Interfaces. *Physical Review Research* **2** (June 25, 2020).
30. Seifert, T. S. *et al.* Terahertz Spectroscopy for All-Optical Spintronic Characterization of the Spin-Hall-Effect Metals Pt, W and $Cu_{80}Ir_{20}$. *Journal of Physics D: Applied Physics* **51** (Aug. 2018).
31. Niimi, Y. *et al.* Extrinsic Spin Hall Effect Induced by Iridium Impurities in Copper. *Physical Review Letters* **106** (Mar. 22, 2011).
32. Erlingsson, S. I. *et al.* Spin Susceptibilities, Spin Densities, and Their Connection to Spin Currents. *Physical Review B* **71** (Jan. 14, 2005).
33. Freeman, R. *et al.* Intrinsic and Extrinsic Contributions to Spin Scattering in Pt. *Physical Review Letters* **120.** arXiv: 1707.05330 (Feb. 9, 2018).

Conclusion

We have used pulsed electromagnetic radiation to probe and excite bulk and thin film crystals with complex ground states. With femtosecond laser pulses interacting with nonlinear media, photon energies from the few-meV to the eV were generated to study charge, spin and structural dynamics after either direct excitation of optical transitions (chapters 2 to 4), or indirect excitation through nonlinear processes (chapter 6).

In chapter 2 we found that collective oscillations of antiparallel spins over macroscopic distances are triggered when driving the manganese ions in $MnPS_3$ into an orbital triplet state. In contrast, these spin waves could not be triggered impulsively through higher-order processes (non-resonant excitation), nor through the ultrafast injection of heat (through optical phonon excitation). For materials with similar characteristics—an orbital singlet ground state with an optically accessible triplet excited state—we expect these waves may be excited in the same fashion. Using coherent spin waves as carriers of information in antiferromagnets as a way to avoid the problem of resistive current losses, and to take advantage of the phase degree of freedom in analog computing schemes, is a scientific research avenue which may lead to useful technologies. Our findings add an unexpected class of antiferromagnets to the list of materials which may prove useful in such schemes.

In chapter 3 we found that photodoping the antiferromagnet $CaMnO_3$ using charge-transfer transitions causes spins to align over macroscopic distances. Measurements of the terahertz transmittivity of a $CaMnO_3$ film showed a fast rise of photocarriers, monotonic in the density of excited electrons. Using the Faraday effect, we detected a rise of magnetization occurring on a slower timescale than the electron transition and exhibiting a critical threshold in the excitation density. Drawing on established knowledge about the energy competitions in the ground state of chemically substituted manganites, we argued that the transient magnetization is the result of double-exchange interactions between photoexcited manganese ions which disposes their spins to align—an interaction which does not occur between the ground state ions. Our experiments take well-established magnetic ground state engineering into the picosecond time domain, and show that magnetic phase instabilities can be triggered by the excitation of charge-transfer transitions.

In chapter 4 we found that the chemical bonding structure at a crystalline interface significantly influences the reflection of coherent acoustic phonons, and that this can be utilized to excite extremely confined acoustic standing waves oscillating in the hundreds of GHz. We photoexcited $SrRuO_3$ crystals of nanometric thickness and found that these exhibit confined phonons that are not present in crystals bound epitaxially to a substrate. Thermal annealing at high temperatures was sufficient to cause restructuring of the interface between the freestanding crystals and a substrate and destroy the acoustic confinement. Today it is possible to produce freestanding crystals of many materials, including the complex oxides. Moreover, many quantum materials exhibit strongly volume-dependent properties. Our results show that a new class of experiments are very feasible: driving high-frequency volume changes on the nanoscale through the excitation of these confined, coherent acoustic phonons.

In chapters 5 and 6 we found that exposure to strong terahertz field oscillations, as generated by planar microfabricated resonators (chapter 5), leads to charge delocalization in the correlated insulator $NdNiO_3$ on a subpicosecond timescale. The phenomenology of our experiment points to the importance of quantum tunneling in this process, a nonlinear effect which takes place well away from any optical transitions and occurs even at zero temperature. This non-thermal mechanism for generating conductivity on a picosecond timescale is a physical process that may turn out to be technologically interesting, for example for electronic switching with extremely high slew rates, operable in cryogenic conditions.

The works presented in this dissertation uses highly specialized and expensive equipment, and the physical situations which are created in the experiments are artificial and contrived. This has long been a quality of empirical science, even since gravity was studied using highly polished balls placed on inclined planes, their descent carefully timed with a water clock. Our strange experiments, taking place near absolute zero or under illumination with bullets of light, serve to teach us about what is *physically possible* given the dispositions of matter or the laws of nature. While on occasion the growing catalog of physical possibilities will produce technological side effects—sometimes even of the world changing kind—this author is content if the dissertation stands as a record of scientific explorations in a dimly lit laboratory, and its results a small addition to the commentary of the Book.

Acknowledgements

Sensitive photodiodes and photomultiplier tubes require a dark laboratory. With no windows and dim lights, I spent many days in darkness, standing right next to one of the world's brightest light sources that shine at wavelengths *just outside* the visible spectrum. Fortunately, the proverbial light of great colleagues has provided me with the necessary vitamins to brighten long days.

I must start by thanking **Andrea Caviglia**, my PhD promotor and supervisor, for the great opportunity to join your team in Delft. You made me feel competent and trusted, allowing me to pursue my own ideas, gave me opportunities to collaborate with other researchers, and put me in rooms that I did not expect to be in. I wish all the best for you and your group in Geneva. To my other promotor, **Yaroslav Blanter**, I must thank you for supporting my career, for being an assuring and conscientious presence in the department, and for making a serious effort to keep me on track during our progress meetings.

For the last two years of the PhD program, Caviglia Lab location Delft was constituted by three *intrepid* souls. Some called us cowboys, others the Lost Boys. With **Ulderico Filippozzi** and **Patrick Blah**, we kept the scientific wheels spinning in Delft against the viscous forces of a department that seemed not to want us there. To both of you, thank you for being comrades, for the openness and frankness between us, for sharing our common despair, and for helping each other with our scientific tasks.

> Ulderico, thank you for your colleagueship, for our many scientific discussions and for our unofficial support group. Also, for your friendship in and outside of work, from beers and smoky dinners to supporting me in the professional melting of plastics, various public explosions, and preserving the secrets of hidden laboratories. Patrick, it has been great to get things off my chest with you over ciders in dark pubs, to hear about your extracurricular escapades, and to work together on our various projects with late hours in the cleanroom and weekend-long diffractograms. While we did not manage to contribute free labor for a luxury for-profit journal, nobody can blame us for not trying.

Before that last era was a more populous one, where I was blessed with the colleagueships of various scientific heroes. **Dmytro Afanasiev** and **Jorrit Hortensius**, your enthusiasm and obvious skill compelled me to join your dark laboratory for my main MSc project. I did not expect to like the work of an optics lab as much as I did, but I want to thank you for that because I have gotten to experience a lot of genuine excitement during my MSc and PhD.

> Dima, your drive and enthusiasm is contagious; as is your confidence that anything is doable, and your immense pragmatic productivity.
>
> Jorrit, I admire your calmness in the storm, your endurance and perserverance, and I look up to your sober scientific eye. I am grateful for the many hours we spent together in the lab, from what you taught me and all your practical advice.
>
> Outside the laboratory, I have learned a lot from the both of you, at a personal level and professionally. I am not least incredibly thankful for your help getting my papers from zero to hero; I am not sure how that would have gone without you.

Amongst my several laser-less colleagues and friends, my employment overlapped substantially with **Thierry van Thiel** and **Edouard Lesne** in Delft, and **Graham Kimbell** in Geneva.

> Thierry, you bring a lot of fun to the table, it is always a good time to discuss with you, be it about science or anything else. The cowboy reputation of the lab members I think must be attributable to you, a true explorer who cannot be stopped from pressing even the scariest of buttons.
>
> Edouard, your healthy scientific skepticism is an important antidote in the current state of things. Your incredible generosity with helping your peers set an ideal for me to follow (and for which I will surely fail).
>
> Graham, I appreciate your collaborative spirit, and for trying out new types of experiments for our projects. You are a kind soul who I would be wise to imitate.
>
> To the other members of the Caviglia Lab, Yildiz and Victoria, with whom I overlapped briefly: thank you for your kindness, genuine spirits, for contributing to a nice atmosphere in the group, and for sharing about your cool and courageous experiments in the group meetings.

A great many other people helped me along the way, and offered great company on my journey.

> To my lovely group of friends known simply as $\hbar$: In various permutations, we have gone to Spain together, partied in the Dutch countryside, lived together, researched together, and shared many meals of varied viscosity. I am very grateful for your friendship throughout the years.
>
> To the various good folk that populated the Department of Quantum Nanoscience together with me, from my E111 office companions, to my lunch partners from Otte Lab, the socially outgoing van der Sar lab, or the various optics labs with whom mirrors and lenses have been exchanged: Thank you for all your help and company, for making the department a nice place to work.

Rasa Rejali, first my colleague, then my friend, then my girlfriend, and finally my wife—all during the production of this dissertation. Respectfully to everyone else I have thanked above, none measure up to the absolute necessity of you. You helped keep me standing when the ground was moving under my feet, you pulled me away from the fire when I was too close. Without you, I would have gotten lost in there. You are the unacknowledged coauthor on everything I did, sometimes quite literally. This goes without saying, but if I ever doubt the value of this period of my life and career, having gained you leaves no room for regret. Asheghetam.

List of publications

- M. Matthiesen et al., *Controlling magnetism with light in a zero orbital angular momentum antiferromagnet*, Phys. Rev. Lett. 130, (2023).
- M. Matthiesen et al., *Temperature-dependent inverse spin Hall effect in Co/Pt spintronic emitters*, Appl. Phys. Lett. 116, 212405 (2020).
- M. Matthiesen et al., *Metallization of a correlated insulator in a strongly driven terahertz resonator*, in preparation.
- M. Matthiesen et al., *Sub-terahertz strain dynamics in $SrRuO_3$ under strong acoustic confinement*, in preparation.
- J. R. Hortensius et al., *Coherent spin-wave transport in an antiferromagnet*, Nat. Phys. 17, 1001 (2021).
- D. Afanasiev et al., *Controlling the anisotropy of a van der Waals antiferromagnet with light*, Sci. Adv. 7, (2021).
- J. R. Hortensius et al., *Ultrafast activation of the double-exchange interaction in antiferromagnetic manganites*, APL Mater 11, 071107 (2023).